DESIGN OF AN ADAPTIVE FUZZY LOGIC CONTROLLER FOR CYLINDRICAL PLUNGE GRINDING PROCESS

SAMUEL KARANJA KABINI

MASTER OF SCIENCE

(Mechatronic Engineering)

JOMO KENYATTA UNIVERSITY OF AGRICULTURE AND TECHNOLOGY

2011

Design of an Adaptive Fuzzy Logic Controller for Cylindrical Plunge Grinding Process

Samuel Karanja Kabini

A thesis submitted in partial fulfillment for the degree of Master of Science in Mechatronic Engineering in the Jomo Kenyatta University of Agriculture and Technology

2011

DECLARATION

This thesis is my original work and has not been presented for a degree in any other university.

Signature..... Date.....

Samuel Karanja Kabini

This thesis has been submitted for examination with our approval as the University supervisors:

Signature..... Date.....

Dr. Eng. Bernard W. Ikua

JKUAT, Kenya

Signature..... Date.....

Dr. George N. Nyakoe

JKUAT, Kenya

DEDICATION

I dedicate this work to my entire family. They have always been there to lift me up when I fall, and to celebrate with me when I succeed.

ACKNOWLEDGEMENTS

I would like to thank the Almighty God, without whom this work would not have even started. I thank Him for giving me the opportunity to undertake this course to completion. I would also like to express my humble gratitude to my supervisors, Dr. Eng. B.W. Ikua and Dr. G.N. Nyakoe, not only for their invaluable guidance and advice throughout my studies, but also for listening to me when I was excited about a new idea. The chief technologist in the department of Mechanical Engineering, Mr. Evans Kibiro, deserves more than a mention for the assistance he accorded me throughout my study. I am happy to acknowledge my debt to Mr. Boniface Kariuki and Mr. Mihari Mumu whose assistance and guidance made my research work fun. A special mention should be made of all Engineering workshops staff for their assistance in setting up and carrying out the experiments, and in particular, Mr. Kathurima and Mr. Sissa who helped me set up my experiment.

In addition, I would like to register my appreciation to my course mates, Lina Owino and Luke Rottok for their constructive criticism, and encouragement. My eternal gratitude goes to Mr. Jackson Githu for his guidance and encouragement throughout my research. I also express my sincere thanks to all members of staff and all post graduate students in the departments of Mechanical and Mechatronic Engineering for their positive input to my work during post graduate seminars through their comments and suggestions. Last but not least, I would like to acknowledge Jomo Kenyatta University of Agriculture and Technology for giving me an opportunity to study and for funding my research.

TABLE OF CONTENTS

LIST OF TABLES

LIST OF FIGURES

LIST OF APPENDICES

LIST OF ABBREVIATIONS

A/D	Analogue to Digital interface
AE	Acoustic Emission
AI	Artificial Intelligence
ANFIS	Adaptive Neural Fuzzy Inference System
CNC	Computer Numerical Control
CBN	Cubic Boron Nitride
CIR	Coarse-grained Information Rate
D/A	Digital to Analogue interface
DAQ	Data acquisition Box
EDF	Error Distribution Function
EP	Elastoplastic
FAM	Fuzzy Associative Memory
FE	Finite Element
FFT	Fast Fourier Transform
FIS	Fuzzy Inference Systems
FL	Fuzzy Logic
FLC	Fuzzy Logic Controller
GA	Genetic Algorithm
LSE	Least Squares Estimate
NN	Neural Network
PID	Proportional Integral Differential

PSD Power Spectral Density

RMS Root Mean Square

rpm revolution per minute

VFD Variable Frequency Drive

NOMENCLATURE

$\boldsymbol{a}$	Instantaneous depth of cut (m)
$\boldsymbol{\beta_g}$	Angular displacement of the grinding wheel $(^\circ)$
$\boldsymbol{\beta_w}$	Angular displacement of the workpiece $(^\circ)$
$\boldsymbol{C}$	Active grit density
$\boldsymbol{C_t}$	Normalized instantaneous chip thickness (m)
$\boldsymbol{d_g}$	Grinding wheel diameter (m)
$\boldsymbol{d_w}$	Workpiece diameter (m)
$\boldsymbol{\delta}$	Displacement (μm)
$\boldsymbol{\delta_n}$	Displacement in the normal direction (μm)
$\boldsymbol{\delta_t}$	Displacement in the tangential direction (μm)
$\boldsymbol{\Delta\beta}$	Wheel angular increment $(^\circ)$
$\boldsymbol{e_c}$	Specific grinding energy (J/mm^3)
$\boldsymbol{f}$	Actual infeed (mm/s)
$\boldsymbol{F}$	Resultant grinding force (N)
$\boldsymbol{F_n}$	Normal force (N)
$\boldsymbol{f_r}$	Control infeed (mm/s)
$\boldsymbol{F_t}$	Tangential force (N)
$\boldsymbol{f'_n}$	Specific force per unit width of segment in normal direction (N/m)
$\boldsymbol{f'_t}$	Specific force per unit width of segment in tangential direction (N/m)
$\boldsymbol{K_{eq}}$	Equivalent system stiffness (N/m)
$\boldsymbol{K_g}$	Grinding wheel stiffness (N/m)

$\boldsymbol{K_n}$	Normalized force coefficient in the normal direction (N/m)
$\boldsymbol{K_s}$	Grinding wheel and machine stiffness (N/m)
$\boldsymbol{K_t}$	Normalized force coefficient in the tangential direction (N/m)
$\boldsymbol{K_w}$	Workpiece stiffness (N/m)
$\boldsymbol{l_d}$	Instantaneous distance between workpiece and grinding wheel centers(m)
$\boldsymbol{l_s}$	Initial distance between workpiece and grinding wheel centers(m)
$\boldsymbol{M}$	Mass (kg)
$\boldsymbol{M_{rr}}$	Material removal rate (mm^3/s)
$\boldsymbol{\mu}$	Coefficient of grinding
$\boldsymbol{r}$	Grit cutting point shape factor
$\boldsymbol{R_g}$	Grinding wheel radius (m)
$\boldsymbol{R_w}$	Workpiece radius (m)
$\boldsymbol{u}$	Input parameters
$\boldsymbol{v_g}$	Grinding wheel surface velocity (m/s)
$\boldsymbol{v_n}$	Instantaneous normal velocity (m/s)
$\boldsymbol{v_t}$	Instantaneous tangential velocity (m/s)
$\boldsymbol{v_w}$	Workpiece surface velocity (m/s)
$\boldsymbol{\Omega_g}$	Grinding wheel rotational speed (rad/s)
$\boldsymbol{\Omega_w}$	Workpiece rotational speed (rad/s)
$\boldsymbol{X}$	X-axis of arbitrary coordinate system
$\boldsymbol{X_g}$	X-coordinate for grinding wheel center
$\boldsymbol{X_w}$	X-coordinate for workpiece center

$\boldsymbol{Y}$	Y-axis of arbitrary coordinate system
$\boldsymbol{Y_g}$	Y-coordinate for grinding wheel center
$\boldsymbol{Y_w}$	Y-coordinate for workpiece center
$\boldsymbol{\psi}$	Phase shift (°)
$\boldsymbol{Z}$	Slide position (m)

ABSTRACT

In modern competitive manufacturing industry, machining processes are expected to deliver products with high accuracy and good surface integrity. This should be achieved through shorter production cycle times with reduced operator intervention and increased flexibility. In order to accomplish this, the trend is towards increased use of machine intelligence in machining processes. Grinding process is usually employed to machine harder materials, or, as a finishing process. A fast, accurate and efficient grinding process contributes greatly to the productivity in a production setup.

In the current work, a theoretical model was developed and used to predict the vibrations resulting from the grinding process. A controller based on adaptive neural fuzzy inference system (ANFIS), was developed for the cylindrical grinding machine-tool. The main aim of this study was to optimize the grinding process by adaptively controlling the speed of the grinding wheel based on the infeed and the speed of the workpiece. This would help in prevention of excessive vibrations that would affect the machining process, resulting in poorly finished surfaces and degraded grinding wheel. Also, experimental work was carried out to validate the model.

From this study, it was demonstrated that, ANFIS based controller controlled vibrations during grinding through in-process adjustment of speed of the grinding wheel so that there would be minimal vibrations. The proposed controller was tested experimentally and was seen to be effective in reducing the machining vibrations by as much as 90 percent.

CHAPTER 1

1 INTRODUCTION

1.1 Background

Grinding is a machining process that employs an abrasive grinding wheel rotating at high speed to remove material from a softer material. It may be thought of as milling using a cutter with a large number of teeth of irregular shape, size, and spacing. Each grit can be seen as a cutting tooth with a specific orientation and sharpness. The grinding process parameters can vary for many reasons. Some of the factors that contribute to the process variation include; sharpness of the grits, wheel microstructure, workpiece material variation and loading of workpiece material on the wheel [1]. The grinding processes can broadly be classified as either surface grinding or cylindrical grinding. Surface grinding is a process that involves a flat workpiece mounted on the table and is ground in both the transverse and longitudinal directions by a cylindrical grinding wheel. Cylindrical grinding process involves a cylindrical workpiece and grinding wheel, each rotating about its own axis. Some examples of cylindrical grinding processes are;

- centerless grinding
- internal and external cylindrical plunge grinding
- internal and external cylindrical transverse grinding
- jig grinding

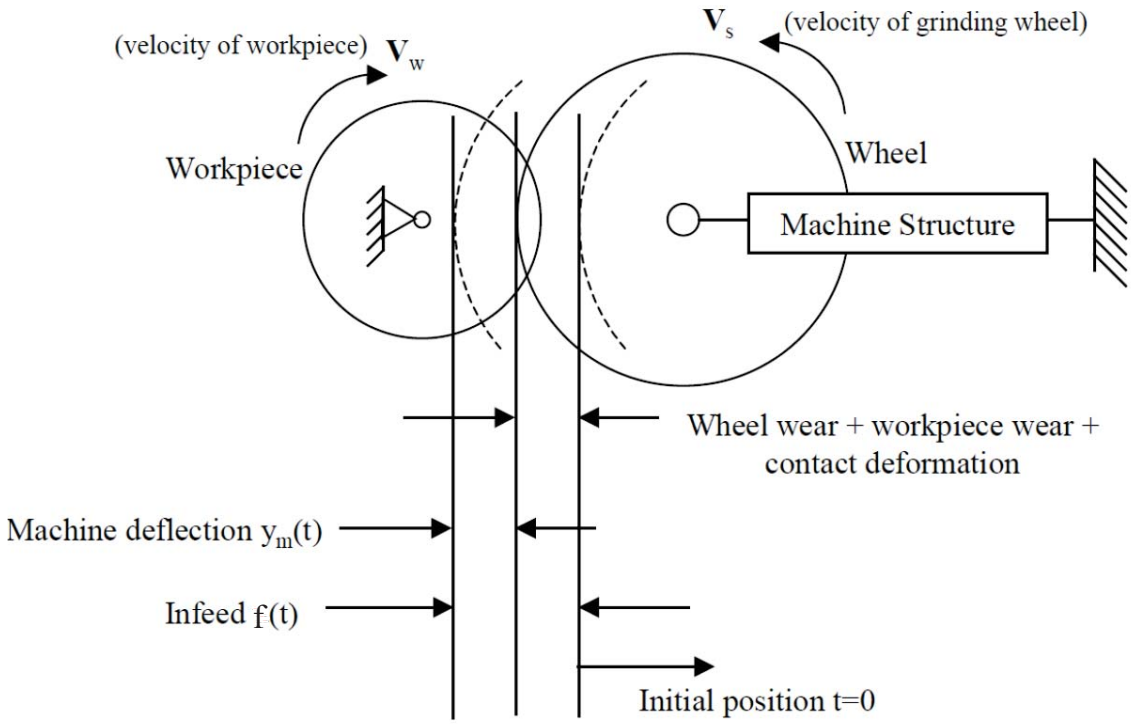

Figure 1.1: Illustration of the cylindrical plunge grinding process

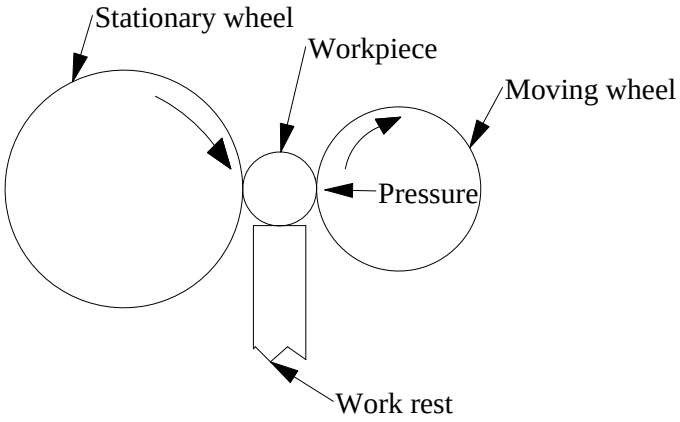

Figure 1.2: Illustration of the centerless cylindrical grinding process

The external cylindrical plunge grinding process can be schematically represented as shown in Fig. 1.1, [2], with the main input parameters being the workpiece and

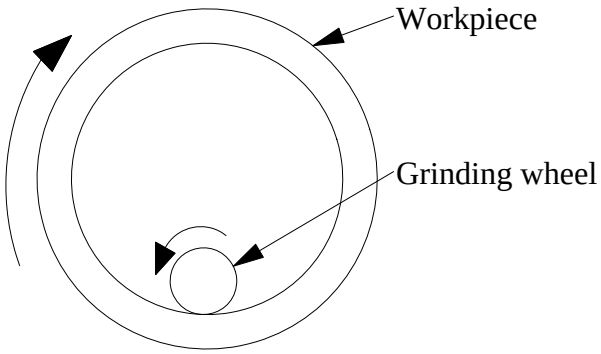

Figure 1.3: Illustration of the internal cylindrical grinding process

grinding wheel rotational speeds V_w and V_s, respectively, and infeed $f(t)$.

1.1.1 Setup and equipment

The setup of a cylindrical grinding machine has a grinding (abrasive) wheel, two centers that hold the workpiece, a chuck and a grinding dog, or other mechanism to drive the workpiece. Most cylindrical grinding machines include a swivel to allow for the forming of tapered pieces. The wheel and workpiece move relative to one another in both the normal and transverse directions. The abrasive wheel can have many shapes. Standard disk shaped wheels can be used to create a tapered or straight workpiece geometry while formed wheels are used to create a shaped workpiece. The process using a formed wheel creates less vibration than using a regular disk shaped wheel.

1.1.2 Abrasive materials

The most commonly used abrasive materials are Aluminium oxide, silicon carbide, diamond, and cubic boron nitride (CBN), with aluminium oxide being the most common of the four. Diamond and CBN wheels are often made of a cheaper core with outer layer of abrasive material to make the wheel less expensive. Diamond and CBN wheels are very hard and can grind down materials such as ceramic and carbides economically [3].

1.1.3 Dressing

This is a process of using a diamond tool to remove the outer layer of a wheel, so that it becomes round (true) and the ends square.

During the grinding process which includes cutting, rubbing and ploughing, vibration is generated. There are two classes of vibration; self excited vibration, commonly known as chatter vibration, and externally induced vibration known as forced vibration. Chatter vibration is generated by the interaction between the wheel and the workpiece and corresponds to the relative movement between the machined part and the cutting tool and can be seen as waves on the machined surface in grinding. The self excited vibration results from the generation of different chip thicknesses during machining [4].

The main objective of carrying out the grinding process is to achieve the required shape, size and surface topography of the finished product in the most economical way. The essential step used to achieve this target are

1. the process design, which design involves selection of suitable input parameters, i.e., grinding wheel and process variables (such as, grinding wheel speed, workpiece speed and feed)

2. dressing type and its variables

3. cutting fluid specifications and its flow conditions.

The selection of the optimum variables depends on a good understanding of their effects on the process output parameters such as, cutting force, feed force, consumed power, cutting temperature and workpiece quality.

However, improvement on the efficiency of the grinding processes is important as the processes develop to compete with increased efficiency in other primary material removal processes and alternative finishing processes. Notably, the grinding process differs from many of the other processes in the complexity of the relationship between the machining parameters and the process performance.

As a consequence, in both manual and Computer Numerical Control (CNC) operations, the process quality and productivity depend to a large extent on the experience of the operator, and as a result many operations are undertaken at conditions far from optimal. Also in modern competitive manufacturing industry, machining processes are expected to deliver products with high accuracy and good surface integrity, using shorter cycle times with reduced operator intervention and increased flexibility. To meet such demands, there is need for increased use of machine intelligence in machining systems and operations. ANFIS has the advantage over the other control

methods in that, it combines the learning ability of neural networks and the ability of fuzzy logic to represent data in a human like manner.

In this study, an adaptive neural fuzzy inference system (ANFIS) is developed for the control of the vibrations that occur during the grinding process. The vibrations in cylindrical grinding process result from the forces generated during the grinding process. The forces are brought about by factors such as, improper infeed, grinding wheel and workpiece speeds and machine wear. Vibrations generated during the grinding process with different parameters are monitored. A decision is made, based on the amplitudes of the vibration either to increase or decrease the necessary process parameters, in order to operate at the optimum conditions.

1.2 Problem statement

Grinding process accounts for about 20-25 percent of the total expenditures on machining operations [5]. During the grinding process and in the interaction between the wheel and the workpiece, chatter vibration is generated. Chatter vibration in grinding operations usually has undesirable effects, such as accelerated tool wear, excessive noise, damage of the machine tool, poor surface finish and low dimensional accuracy of the machined part [6]. All of these negative effects of chatter not only increase the machine downtime, hence lowering productivity, but, they also lower the quality of the finished surface. The chatter vibration is as a result of poor selection of machining parameters. There is, therefore, need for the development of an in-process control system that is able to detect the changes in the machining conditions and adjust the various process parameters to their optimum values.

1.3 Objectives

The main objective was to develop an adaptive neural fuzzy inference system (ANFIS) based controller, for the optimization of the process parameters in the cylindrical plunge grinding process, in real-time. To achieve this objective, the following specific objectives were accomplished;

1. Development of a theoretical model for predicting the chatter vibrations that result from the grinding process, based on the process parameters.

2. Validation of the model through a series of experiments.

3. Development of a controller based on adaptive neural fuzzy inference system (ANFIS), for the control of the vibrations.

4. Simulation, testing and implementation of the ANFIS based controller.

1.4 Justification of the study

Cylindrical plunge grinding process is usually employed as a final stage machining process for cylindrical workpieces, or for the machining of hard materials. The process is expected to improve on the quality of a product's surface finish. However, the process is usually affected negatively by the occurrence of chatter vibrations during the grinding process. These vibrations are difficult to control by conventional control methods, due to the complex nature of the grinding process. The proposed ANFIS based controller is aimed at controlling the cylindrical plunge grinding process by minimizing the chatter vibration. The controller significantly and effectively reduces

the vibration amplitudes, leading to improved quality of the machined part, reduced machine downtime and at the same time eliminating the need for a human operator during the grinding process.

1.5 Outline of thesis

This thesis contains five chapters. The first chapter provides an introduction to the research by highlighting the existing problem, the objective and the scope of the research work. Chapter 2 is a literature review on occurrence of vibration in cylindrical plunge grinding process and the various methods employed in its control. Chapter 3 outlines a theoretical approach in modeling and analysis of the chatter vibrations in the cylindrical plunge grinding process. In chapter 4, theoretical results obtained in chapter 3 are validated through experimental work. Finally chapter 5 outlines the design procedure for the adaptive neural fuzzy controller, its simulation and implementation. The conclusion and recommendations are made in chapter 6.

CHAPTER 2

2 LITERATURE REVIEW

2.1 Overview

In recent years, grinding research has had a renewed focus on the mechanics of the grinding process. A question such as how material is removed from the surface is of considerable importance from both research and industrial perspectives. However, significant challenges exist when attempting to answer this fundamental question. This could be addressed by empirical models, but such empirical approaches often require the fitting of non-physical parameters into experimental data, which creates a phenomenological model [7]. As a result, the fundamental physical processes at work during material removal cannot be directly investigated. Furthermore, advanced modeling of the material removal process requires constitutive material models incorporating elastoplasticity theory. Elastoplastic (EP) material models are commonly used in metal-cutting and metal-forming applications [7], but present an analytical impasse where equations can only be solved numerically.

2.2 Modeling of the grinding process

Many researchers have made attempts to come up with models of the grinding process. This has resulted in a number of models, each attempting to address, or emphasize on, a specific area of the grinding processes.

Modeling of the grinding process can be achieved through development of empirical and theoretical models, but, modeling generally involves a trade-off between the

accuracy of the model and the difficulty (or physical possibility) of obtaining the necessary information or parameters.

Theoretical grinding models for calculating material removal rates are based on the specific cutting energy of the material and energy distribution of the applied power [8]. Mathematical models make it possible to simulate machining vibration quite accurately, but in practice, it is difficult to avoid vibrations. The following is a review of the milestones achieved in modeling of the grinding process.

Rogelio *et al* [9] developed equations governing the surface roughness in plunge grinding. These equations included several physical mechanisms in grinding. The physical mechanisms considered were wheel-workpiece overall deflection, local grit deflection and individual grit-workpiece interaction. The equations also took into account the workpiece material properties, type of wheel, machine characteristics and machining parameters, such as, tool feed per revolution, dressing conditions and wheel/workpiece tangential velocities. The time dependent behavior of the grinding process was also considered. The equations were used in an optimization strategy composed of an accelerated spark-out process combined with a power controlled stock removal stage. The control system that was developed used surface roughness equations to control the part dimension, and also ensure that, surface roughness requirements were met. This ensured dimensional accuracy of the part.

Mohammed *et al* [10] investigated the effects of dynamic changes in the grinding force components due to changes in the grinding wheel's flat area wear, and the workpiece material on the vibration behavior of the grinding spindle. The steady-state dynam-

ics and vibration behavior of the grinding machine spindle was simulated by a five degree of freedom model. The results indicated different vibration behavior, when grinding different materials using a grinding wheel with fixed wear flat area. As the grinding wheel flat area increased, the level of vibration increased for all the degrees of freedom, which indicated that, there was an upper limit for the level of wear on the grinding wheel beyond which, dressing operation must be conducted on the grinding wheel.

Biera *et al* [11] presented a time-domain dynamic model of the external cylindrical plunge grinding process. The model consisted of a block-based simulation tool that simplified the inclusion of process or machine parameters. Since the model was a time-domain model, non-linear effects could be considered. The model included the interference phenomenon between two consecutive workpiece revolutions. The reason for the inclusion of this phenomenon was to explain which process parameters cause unstable conditions during stability analysis. The model permitted the visualization of the lobe destruction effect between consecutive workpiece revolutions.

Franciszek *et al* [12] conducted theoretical analysis of the dynamics for the machine tool-workpiece system, for cylindrical plunge grinding process. A mathematical model of grinder equipped with hydrostatic bearing on the grinding wheel spindle and hydrostatic slideways was developed. Simulations based on the developed model allowed qualitative investigation of grinding force characteristics, and its influence on forced vibrations in the grinder. It was demonstrated that, the grinding force significantly influenced the forced vibration damping of the headstock for a grinding wheel.

Orynski *et al* [13] developed a physical model of a cylindrical plunge grinder with hydrostatic slideways and hydrostatic bearings for the grinding wheel spindle. The model was used to check the influence of the grinding process on forced vibration damping by the grinding wheel headstock.

Huang *et al* [14] presented a closed form expression for the stochastic grinding force as a function of the grinding conditions and grit distribution that incorporated the random nature of grit distribution. The stochastic grit density function was introduced to describe the random grit distribution of the rotating wheel. The dynamic grinding force was formulated as the convolution of a single-grit force and the grit density function. The single-grit force was obtained from analysis of the grinding geometry and treated as a deterministic impulse response of the grinding process. The spectrum characteristics of the grinding force were investigated in the frequency domain, where the power spectral density (PSD) of the total grinding force could be expressed as a product of the energy spectral density of the single-grit force and the PSD of the grit density function. The analytical nature of the PSD expression of the grinding force allowed the identification of the PSD of the grit density function and the mechanistic grinding coefficients, and facilitated the analysis of the effects of the grit distribution and grinding conditions upon the grinding force.

Sakakura *et al* [15] carried out a visual simulation of the grinding process. The work involved several computer simulations using the Monte Carlo Method. Most of the simulations calculated static geometrical interference between a grain and a workpiece. They also developed a simulation program based on the elastic behaviour

model of a grain, that focused on the generation process of a workpiece surface, and simulation of the interaction of grains with a workpiece, which includes the elastic and plastic deformation as well as the removal of workpiece material.

Kuang *et al* [16] modeled and predicted the grinding force for the creep feed grinding process, using back propagation (BP) neural network. The BP neural network was improved by integrating an error distribution function (EDF), to overcome local minimum problems. This was done in order to find the global minimum solution, and to accelerate the convergence speed. Compared with the theoretical force model, the force model implemented by the improved BP neural network was found to be more accurate.

2.3 Occurrence of chatter in grinding process

Chatter vibration occurs when there is contact and relative motion between the grinding wheel and the workpiece. The waves generated on the workpiece surface are caused by the periphery of the grinding wheel and vice versa. There are conditions that can cause the amplitudes of the relative vibration and the waves generated on the workpiece surface to be identical. The conditions are; low vibration frequency, small relative amplitude and low workpiece velocity.

However, once the critical limit determined using the above-mentioned parameters is exceeded, the amplitude of waves generated on the workpiece surface becomes smaller than that of the relative vibration. In other words, the envelope curve starts to have a mode (a characteristic pattern or shape in which the system will vibrate).

Assuming that the amplitude of the relative vibration and the waves is y and a_w, respectively, geometrical interference, G_{e0}, which is a non-linear relationship, can be derived [17]. In equations 2.1 through 2.3 y_{cr} represents a critical amplitude, v_w, is the workpiece surface velocity, and ω is the angular chatter frequency.

$$G_{e0} = \frac{a_w}{y} \tag{2.1}$$

$$G_{e0} = \frac{1}{2}(1 - \cos\sqrt{\frac{y_{cr}}{y}}\pi) \text{for} \quad \frac{y_{cr}}{y} < 1 \tag{2.2}$$

$$y_{cr} = \frac{v_w}{\omega^2}\frac{2(d_w + d_s)}{d_w d_s} \tag{2.3}$$

When $y_{cr} < y$, the amplitude of waves becomes smaller than that of the relative vibration. Otherwise, both amplitudes remain identical. As for the waves generated on the grinding wheel, the critical amplitude is obtained by replacing workpiece surface velocity v_w with grinding wheel speed v_s. Therefore, the critical amplitude will be much larger for the waves generated on the grinding wheel because the wheel speed is always much higher than the workpiece speed. This implies that, workpiece regeneration (wear on workpiece due to chatter vibration) has a complete effect on process instability and the development of grinding wheel regeneration (wear on wheel due to chatter vibration) is much slower than workpiece regeneration.

The phenomenon of self excited vibration in grinding are summarized as below [18]:

1. Self-excited vibration due to regenerative effect on the workpiece periphery can progress so fast that, it becomes impossible to perform the process. Self-excited vibration of this type is likely to be generated when the peripheral speed of the workpiece is high.

2. On the other hand, by reducing the workpiece peripheral speed, self-excited vibration due to regenerative effect on the workpiece can be restrained. This, in turn, leads to generation of self-excited vibration due to the regenerative effect on the grinding wheel surface. Although vibration(s) of this type progress(es) relatively slowly, the grinding conditions fall in an unstable area. This is because the wheel surface must be adjusted (trued or dressed), at a point when the gradually progressing amplitude of vibration reaches the allowable limit. Due to the dressing/truing, the end of the service life of the grinding wheel can be reached. It is, therefore, necessary to select such grinding conditions that would restrain the progress of vibration and thereby extend the service life of the grinding wheel.

2.4 Chatter detection and control

One of the major causes of low efficiency in the grinding process is vibration, that is, either self-induced (chatter) or forced vibration [19]. The forced vibration is caused by factors that do not result directly from the grinding operation, and they include: (i) wear of the bearings and other machine parts, (ii) spindle misalignment and (iii) lack of proper spindle geometry, caused by such factors as worn out belts and bent shafts. Regenerative, i.e., chatter vibration starts as a slip-slide interaction between wheel and workpiece, and then causes the regenerative effect, which is produced when the tool passes through a previously cut surface. Under certain cutting conditions, this effect causes the undulations of the workpiece to regenerate, leading to chatter vibrations [20]. Chatter is caused by a number of factors that include: (i) a heavy

cut, (ii) non-uniformity of the workpiece profile, (iii) change of material properties, which could be as a result of cast materials or hardening of the material being ground and (iv) too much or too low feed rate.

Vibrations in cylindrical grinding affect the quality of the finished surface, the roundness of the workpiece, and also the lifetime of the machine and the tool [21]. Forced vibrations can to a certain extent be controlled through proper maintenance of machine. Therefore, to a large extent, the productivity of material removal machining operations is primarily limited by the presence of chatter vibration [20].

Oscar *et al* [22] developed a technique for chatter detection on ground cylindrical parts. In their work, the waviness was measured with a mechanical stylus profiler with a diamond tip, and then converted into height values with the help of a precision displacement transducer. The output signal was later converted to digital form and transformed to the time-frequency domain by means of the wavelet transform, which allowed its coefficients to grow as a function of surface defects and chatter marks. The method was validated experimentally. This technique could measure the depth of the defects, and give information on the location of the chatter marks on the surface.

Hassui *et al* [23] studied the relationship between the process vibration signals and the workpiece quality parameters, namely mean roughness, circularity and burning. The purpose of the study was to use these signals to decide the exact moment to dress the wheel. In order to reach this goal, several experiments were carried out in a plunge cylindrical grinding operation of an AISI 52100 quenched and tempered steel, having as input variables, the dressing overlap ratio, the spark out time and

the workpiece velocity. The output variables were the workpiece surface roughness and circularity and also the process vibration during both the cutting phase and the spark out phase of the grinding cycle. The study revealed that it was possible to have good workpiece quality even with a vibration level much higher than that obtained with a recently dressed wheel. In addition, vibration during cutting phase and at the end of complete spark out could be used to monitor the wheel condition, at least when high dressing overlap ratio was used. Furthermore, the decrease in the spark out time made the vibration at the end of spark out increase but did not cause any significant damage in surface finish.

Fernandes *et al* [24] applied a novel process approach to simulate an active vibration control system in a centerless grinding machine. Based on the updated finite element model of the machine, the structural modifications performed to incorporate active elements were detailed, as well as the subsequent reduction procedure to obtain a low-order state space model. This reduced structural model was integrated in the cutting process model to give a tool that was adapted for the purpose of simulating different control laws.

Shaw *et al* [25] used magnetic Barkhausen noise method to develop a control system for the grinding process. The controller was used to detect small changes in the level of surface residual stress and hardness which would allow the detection of grinding damage at its onset. The controller that was developed focused on detection and avoidance of destruction of the workpiece.

Jason *et al* [26] carried out a study on cylindrical grinding open architecture and

feed rate control by power feedback. The controller that was developed applied PID control techniques. It used Kalman filter and state variable feedback to control the velocity and hence the feed rate.

Janez *et al* [4] developed two methods for automatic chatter detection in outer diameter plunge feed grinding using acoustic emissions. The methods employed entropy and coarse-grained information rate (CIR) as indicators of chatter. Entropy was calculated from a power spectrum, while CIR was calculated directly from fluctuations of a recorded signal. The methods were verified using signals of the normal grinding force and Root Mean Square (RMS) acoustic emission. The results showed that entropy and CIR performed equally well as chatter indicators. Based on the normal grinding force, they detected chatter in its early stage, while only cases of strong chatter were detected based on RMS acoustic emission.

Lee et al [27] investigated the characteristics of external plunge grinding using the current signals of the spindle motor through a hall sensor. Grinding experiments were conducted under various grinding conditions such as wheel speeds, workpiece speeds and feed rates with a conventional vitrified bonded wheel. Analysis of the current signal of the spindle motor was done and a relationship between current signals and the metal removal rate in terms of the feed rate was shown. It was also shown that, a hall sensor has similar capabilities in evaluation of grinding behavior as those of the acoustic emission (AE) signals, which are useful for monitoring the grinding process.

Jae *et al* [28] developed a trouble diagnosis system for the grinding process. The acoustic emission signals generated during machining were analyzed to determine

the relationship between grinding related troubles and characteristics of changes in signals. Furthermore, a neural network, was applied to the diagnosis system. The neural network was optimized with a momentum coefficient (m), a learning rate (γ), and a structure of the hidden layer in the iterative learning process.

Hodge *et al* [1] developed an adaptive force controller for the grinding process. The controller was achieved by use of a real-time grinding model, where an adaptive pole-zero cancelation technique was developed and implemented to reduce the grinding process variation. Real-time model parameter estimation and controller designs were implemented to achieve higher bandwidth control capability. However, the controller developed used an approximation model for the grinding process, which may vary from the actual grinding process due to the complex nature of the process.

Albizuri *et al* [29] employed a novel method to reduce chatter vibrations in a centerless grinding machine, using actively controlled piezoelectric actuators. A simplified model of the machine was used to simulate the behavior of several commercially available piezoelectric actuators in two different locations of the machine. Based on these simulations, a selection of proper actuators and their optimal location was obtained and the control system was implemented experimentally.

Junkar *et al* [30] investigated the plunge grinding process by use of power spectrum of vibration signals. In order to predict the process evolution, certain predefined spectral attributes were extracted and process performance classes were assessed by an expert. Training examples described in terms of the attribute values and corresponding classes were submitted to an inductive machine learning system. As a result,

classification rules were synthesized, predicting the grinding wheel performance from the spectral attributes. Training data was refined severally to increase the accuracy of the induced rules and reduce the complexity. The controller was used to predict the grinding wheel performance in real time.

Saravanan *et al* [31] developed a Genetic Algorithm (GA) based optimization procedure. The algorithm was used to optimize grinding conditions, that is, wheel speed, workpiece speed, depth of dressing and lead of dressing, using multi-objective function model with a weighted approach for surface grinding process. The procedure evaluated the production cost and production rate for the optimum grinding condition subject to constraints such as thermal damage, wheel wear parameters, machine tool stiffness and surface finish. The new GA procedure was illustrated with an example and optimum results such as production cost, surface finish and material removal rate were compared with quadratic programming techniques.

Ding [32] used a neural network (NN) and fuzzy logic approach in prediction and control of workpiece size in the grinding process. Dynamic Elman neural network was used in the prediction model. The hidden layer structure was modified, and the first and the second derivative of the actual amount removed from the workpiece were added into the network input, which greatly improved the prediction accuracy. A fuzzy control model with flexible factor was used to control workpiece size. Simulation and experiments were done to verify the ability of the proposed algorithm in workpiece size prediction, and precision control.

2.5 Conclusion

Previous research studies have used varied approaches to controlling the grinding process. However there is none that can be said to be fully efficient on its own. Also, there have been little attempt to control the vibrations during the grinding process. This could be due to the complex nature of the process, which makes it difficult to develop analytical models for the process. Therefore, the current work seeks to develop a control system that would optimize the grinding process by controlling the machining vibrations without the need for an accurate process model. The controller will minimize process vibrations by selection of the optimum process and input parameters hence boosting production while at the same time reducing production cost, and improving the quality of the products as well as improve tool life.

CHAPTER 3

3 ADAPTIVE NEURAL FUZZY INFERENCE SYSTEMS (ANFIS)

3.1 Background

The design of modern control systems is characterized by stringent performance and robustness requirements and therefore relies on model-based design methods. This introduces a strong need for effective modeling techniques. Many systems are not amenable to conventional modeling approaches due to strongly nonlinear behaviour and lack of precise knowledge of the process under study. Nonlinear identification is therefore becoming an important tool which can lead to improved control systems along with considerable savings of time and cost. Among the different nonlinear identification techniques, methods based on fuzzy sets are gradually becoming established [33].

Adaptive control is a method of designing a controller with some adjustable parameters and an embedded mechanism for adjusting these parameters. Adaptive methods have been used mainly to improve the controller's performance online [34]. For each control cycle, the adaptive algorithm is normally implemented in three basic steps, namely,

1. Observable data is collected to calculate the controller's performance.

2. The controller's performance is used to calculate the adjustment to a set of controller parameters.

3. The controller's parameters are then adjusted to improve the performance of the controller in the next cycle.

Normally, an adaptive controller is designed based on one of the available techniques. Each technique is originally designed for a specific class of dynamic systems. The controller is then adjusted, as data is collected during run time to extend its effectiveness to control a larger class of dynamic systems.

ANFIS, which is derived from the term Adaptive Network Based Fuzzy Inference System, was first proposed by Jang [35], and later changed to Adaptive Neural Fuzzy Inference System. This system is designed to allow IF-THEN rules and membership functions (fuzzy logic) to be constructed based on the historical data and also includes the adaptive nature for automatic tuning of the membership functions.

3.2 Fuzzy logic

Fuzzy logic has two different meanings. In a narrow sense, fuzzy logic is a logical system, which is an extension of multivalued logic. However, in a wider sense fuzzy logic is almost synonymous with the theory of fuzzy sets, a theory which relates to classes of objects with unsharp boundaries in which, membership is a matter of degree [36].

The word *fuzzy* is used to describe terms that may be, are not well-known, or are not clear enough, or terms whose closer specification depends on subjectivity, estimation, and even the intuition of the person who is describing these terms. In everyday life, there are many situations characterized by a certain degree of ambiguity whose description includes terms and expressions such as *majority*, *many*, *several*, *not exactly*,

or *quite possible*, all of which can be qualified as fuzzy terms. On the other hand, terms like *false*, *true*, *possible*, *necessary*, *none*, or *all* reflect crisp meanings, and in such a context, represent exact terms [37].

The mathematics of fuzzy set theory, and by extension fuzzy logic were developed in 1965 by Zadeh [38]. New operations for the calculus of logic were proposed, and were in principle, a generalization of classical logic [39]. This theory proposed making the membership function (or the values False and True) operate over the range of real numbers [0.0, 1.0]. The notion central to fuzzy systems is that truth values in fuzzy logic or membership values in fuzzy sets are indicated by a value in this range, with 0.0 representing absolute Falseness and 1.0 representing absolute Truth [40].

There is a distinction between fuzzy systems and probability [41]. Although both operate over the same numeric range, and at first glance, both have similar values: 0.0 representing False (or non- membership), and 1.0 representing True (or membership), there is a difference between the two theories in that the probability theory indicates the chances of an event happening, while the fuzzy set theory indicates the extent to which the event will occur.

Fuzzy logic control refers to a technique of embodying human thinking into a control system. Fuzzy logic controllers are designed to emulate human deductive thinking, that is, the process people use to infer conclusions from what they know [36].

Fuzzy logic systems are rule-based systems in which an input is first fuzzified, that is, converted from a crisp number to a fuzzy set, and subsequently processed by an

inference engine that retrieves knowledge in the form of fuzzy rules contained in a rule-base. The fuzzy sets that are computed by the fuzzy inference as the output of each rule are then combined and defuzzified, that is, converted from a fuzzy set to a crisp number. A fuzzy logic system is a nonlinear mapping from the input to the output space [42].

3.3 Fuzzy IF-THEN rules and fuzzy inference systems

Fuzzy IF-THEN rules or fuzzy conditional statements are expressions of the form IF A THEN B, where A and B are labels of fuzzy sets that are characterized by appropriate membership functions [38]. Due to their concise form, fuzzy IF-THEN rules are often employed to capture the imprecise modes of reasoning that play an essential role in the human ability to make decisions in an environment of uncertainty and imprecision [43]. An example that describes a simple fact is *IF pressure is high, THEN volume is small*, where *pressure* and *volume* are *linguistic variables*, *high* and *small* are *linguistic values* or *labels* that are characterized by membership functions. Another form of fuzzy IF-THEN rule, proposed by Takagi and Sugeno [44], has fuzzy sets involved only in the premise part. By using Takagi and Sugeno's fuzzy IF-THEN rule for example, the resistant force on a moving object can be described as follows:

IF velocity is high, THEN force $= k(velocity)^2$

where, again, *high* in the premise part is a linguistic label characterized by an appropriate membership function. However, the consequent part is described by a nonfuzzy equation of the input variable, velocity. Both types of fuzzy IF-THEN rules have been used extensively in both modeling and control.

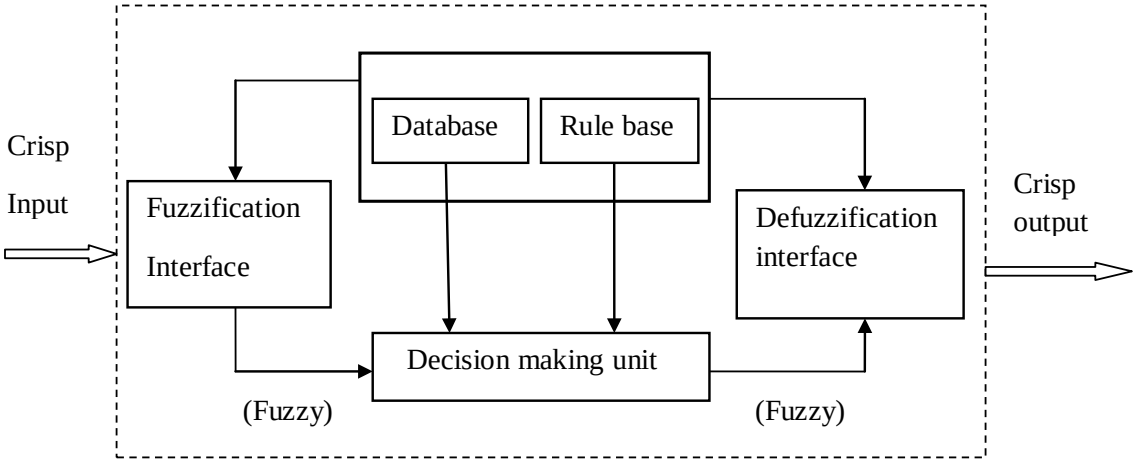

Figure 3.1: Fuzzy inference system

Through the use of linguistic labels and membership functions, a fuzzy IF-THEN rule can easily capture decision making capability of humans [35]. Also, due to the qualifiers on the premise parts, each fuzzy IF-THEN rule can be viewed as a local description of the system under consideration. Fuzzy IF-THEN rules form a core part of a fuzzy inference system.

Fuzzy inference systems are also known as fuzzy-rule-based systems, fuzzy models, fuzzy associative memories (FAM), or fuzzy controllers when used as controllers. A fuzzy inference system is composed of five functional blocks as shown in Figure 3.1. The functional blocks are as follows:

- A *rule base* containing a number of fuzzy IF-THEN rules.
- A *database* which defines the membership functions of the fuzzy sets used in the fuzzy rules.

- A *decision-making unit* which performs the inference operations on the rules.
- A *fuzzification interface* which transforms the crisp inputs into degrees of match with linguistic values.
- A *defuzzification interface* which transform the fuzzy results of the inference into a crisp output.

Usually, the rule base and the database are jointly referred to as the knowledge base.

The steps of fuzzy reasoning (inference operations upon fuzzy IF-THEN rules) performed by fuzzy inference systems are:

1. Compare the input variables with the membership functions on the premise part to obtain the membership values of each linguistic label. This process is often called *fuzzification*.
2. Combine the membership values on the premise part to get *firing strength* or *weight* of each rule through a specific T-norm operator.
3. Generate the qualified consequent of each rule depending on the firing strength.
4. Aggregate the qualified consequents to produce a crisp output.

Several types of fuzzy reasoning have been proposed in the past [45]. Depending on the types of fuzzy reasoning and fuzzy IF-THEN rules employed, most fuzzy inference systems (FIS) can be classified into three types as shown in Figures 3.2 through 3.4.

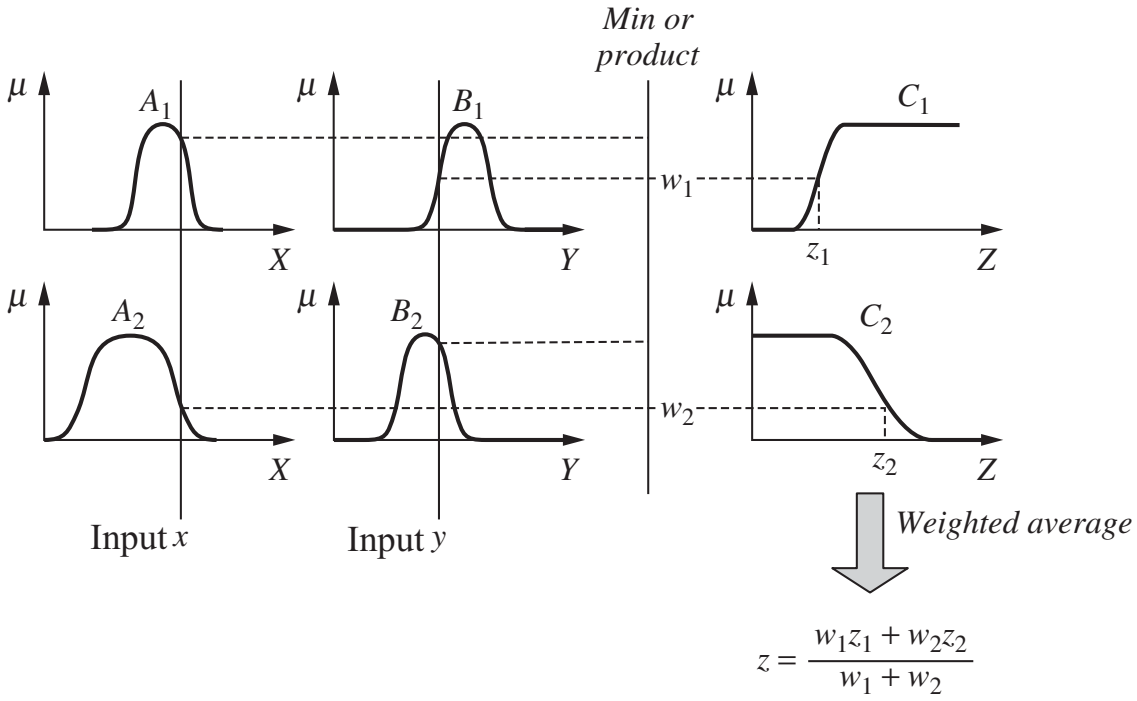

Figure 3.2: Type 1 FIS

1. **Type 1 FIS:** The overall output is the weighted average of each rules crisp output induced by the rule's firing strength. It is obtained as the product or minimum of the degrees of match between the premise part and the output membership functions. The output membership functions used in this scheme must be monotonic functions [45]. This type of FIS is illustrated in Figure 3.2. In this figure the output is given by z.

2. **Type 2 FIS:** The overall fuzzy output is derived by applying 'max' operation to the qualified fuzzy outputs. Various schemes have been proposed to choose the final crisp output based on the overall fuzzy output; some of them are centroid of area, bisector of area, mean of maxima, maximum criterion, etc [45]. This type of FIS is illustrated in Figure 3.3, in which y* represents the crisp output.

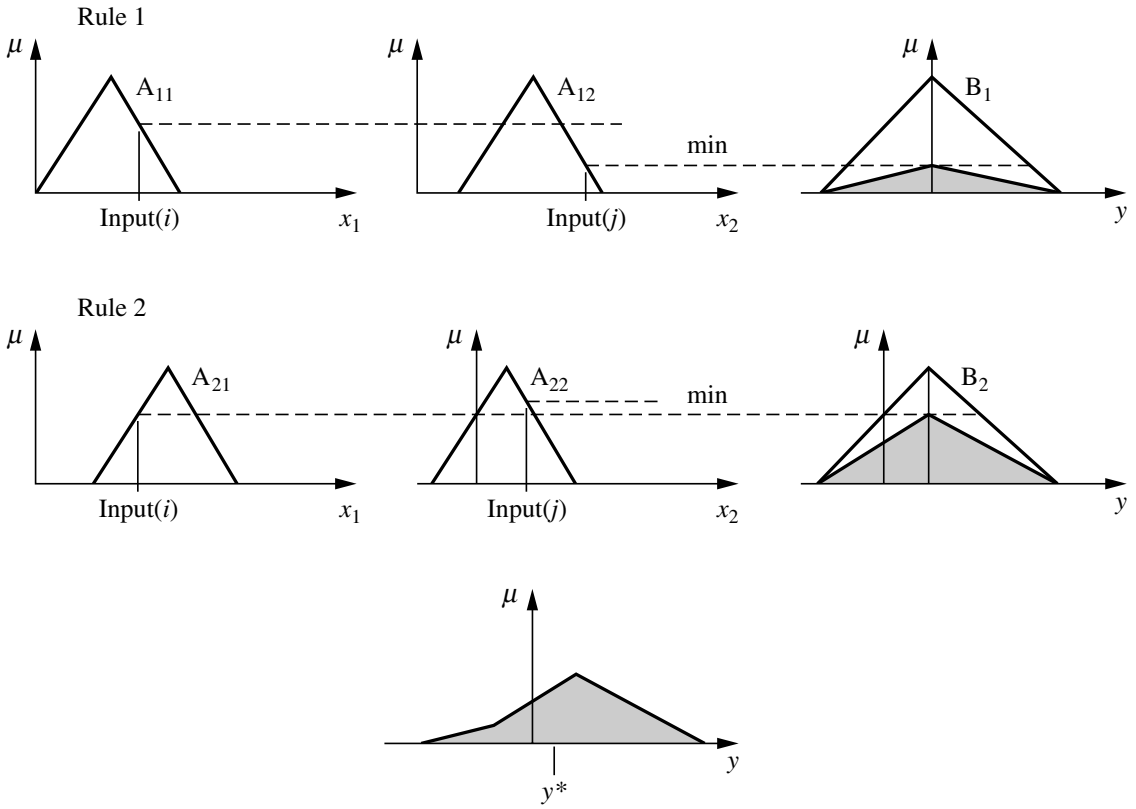

Figure 3.3: Type 2/Mamdani FIS

3. **Type 3 FIS:** In this type, Takagi and Sugeno's fuzzy IF-THEN rules are used. The output of each rule is a linear combination of input variables plus a constant term, and the final output is the weighted average of the rules' outputs [46]. Figure 3.4 illustrates this type of FIS, in which p, q and r are constants, and the output is given by z.

Figures 3.2 through 3.4 utilize a two-rule two-input fuzzy inference system to show the different types of fuzzy rules and fuzzy reasoning. In these figures, μ is the universe of discourse, while A, B and C represent the membership functions. Also, w_i represents the i rule's firing strength. As noted, most of the differ-

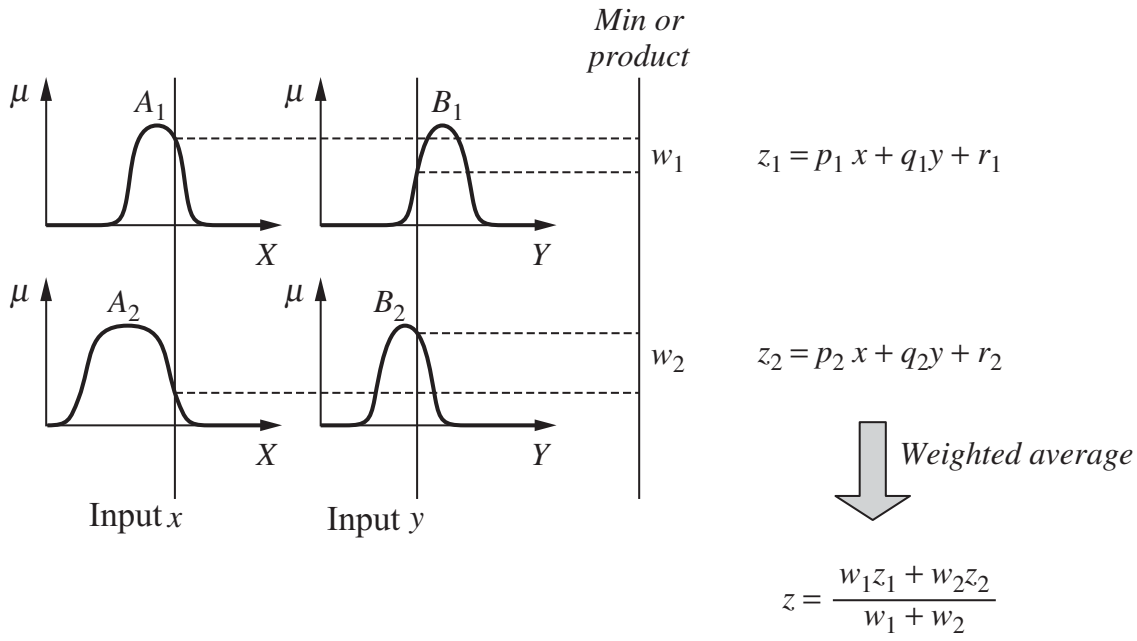

Figure 3.4: Type 3/Takagi-Sugeno FIS

ences in the fuzzy inference systems are in the specification of the consequent part, which may be monotonically non-decreasing, bell-shaped, trapezoidal or triangular membership functions, or crisp function and thus the defuzzification schemes are also different. However, the inference systems' outputs are defuzzified into crisp outputs and the output is always crisp, no matter the inference system used.

The most widely used inference mechanisms are the Mamdani and Takagi-Sugeno inference mechanisms. The Mamdani inference mechanism is used where there is need to capture human knowledge, while Takagi-Sugeno is used in nonlinear control due to its ability to model nonlinear processes.

3.4 Structure of ANFIS

An example of a zero-order Takagi Sugeno fuzzy model with two rules represented as a neural fuzzy network is shown in Figure 3.5. It shows the basic architecture of ANFIS with two inputs and one output. The ANFIS architecture shown is a multilayer feed-forward network where each node will perform a particular function on the incoming input signals. Each node will adapt and be trained by changing its parameters and/or formulae.

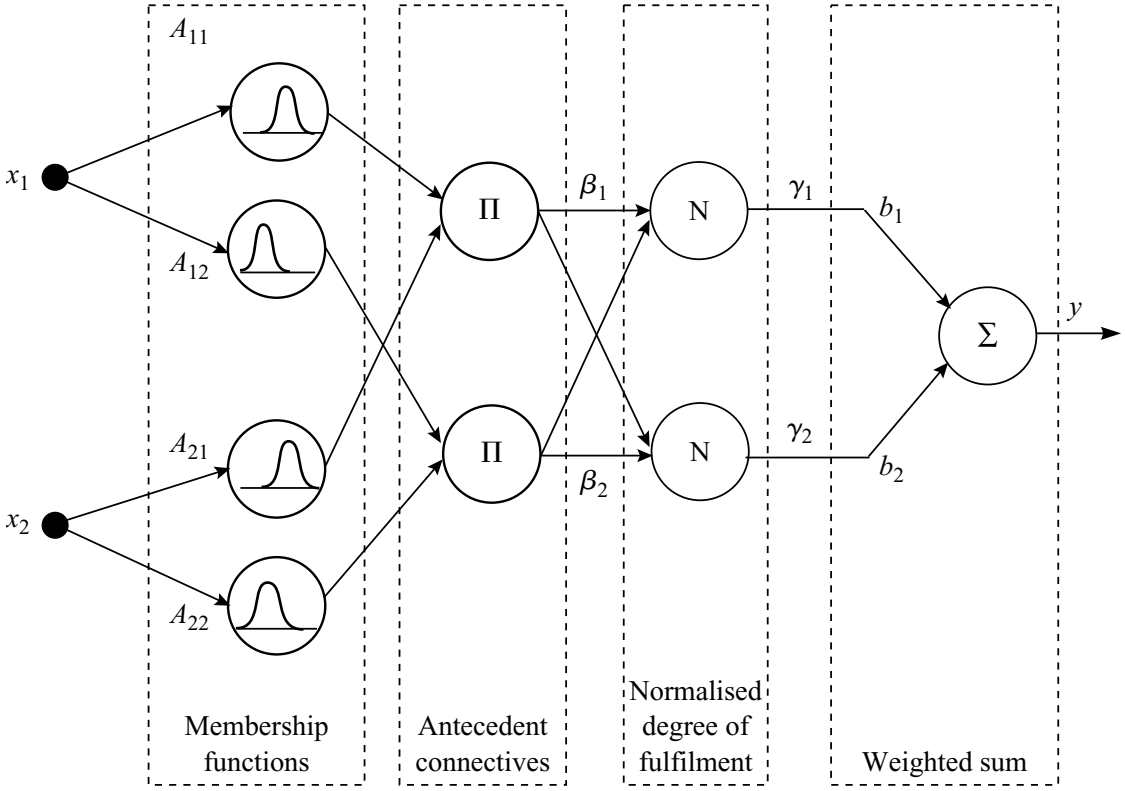

Figure 3.5: An example of a two rule Takagi-Sugeno ANFIS

Jang [35] proposed that the functions of the nodes are grouped into five different layers:

- Layer 1: Here, the membership functions are defined hypothetically and usually bell-shaped membership function shown in equation 3.1 is chosen [47]. This is because of the greater ability of this type of membership function to represent the vagueness associated with non-linear systems, as compared to triangular and trapezoidal membership functions.

$$u_{A_i}(x) = \frac{1}{1 + \left[\left(\frac{x - c_i}{a_i}\right)^2\right]^{b_i}} \tag{3.1}$$

  where $u_{A_i}(x)$ is the membership function of A_i, and it specifies the degree to which the given x satisfies the quantifier A_i. $u_{A_i}(x)$ has maximum value of 1 and minimum value of 0 and $\{a_i, b_i, c_i\}$ is the parameter set, with a_i and b_i being the inputs and c_i the output.

  When the values change, the bell-shaped membership functions will also change accordingly. In this layer, the parameters involved in the process are known as the premise parameters.

- Layer 2: In this layer, each output of the node defines the firing strength of the rules in the fuzzy inference engine.

- Layer 3: This layer calculates the ratio of the i^{th} rule's firing strength [35]. The result is the normalized firing strength, $\hat{\alpha}_i$, shown in equation 3.2.

$$\hat{\alpha}_i = \frac{\alpha_i}{\alpha_1 + \alpha_2} \tag{3.2}$$

where α_i is the firing strength of the rule i.

- Layer 4: The parameters of the nodes in this layer are called the consequent parameters. The nodes in this layer adapt with an output node.

- Layer 5: Nodes in this layer are fixed and they sum all incoming signals from the previous layers.

3.5 Training of ANFIS

An adaptive network, is a network structure consisting of nodes and directional links through which the nodes are connected. Moreover, part or all of the nodes are adaptive, which means that, their outputs depend on the parameter(s) pertaining to these nodes, and the learning rule specifies how these parameters should be changed to minimize a prescribed error measure [35].

The basic learning rule of adaptive networks is based on the gradient descent and the chain rule [47]. Jang [48] generalized the formulas for the basic learning rule that were proposed by Werbos [49]. Also, due to the fact that the rule is based on the gradient method, it has slowness and tendency to become trapped in the local minima. Jang [40] used this property to develop a hybrid learning rule which can speed up the learning process substantially. Both the batch learning and the pattern learning that comprise the hybrid learning rule are discussed below.

The training algorithm for the ANFIS that is developed is based on the hybrid learning algorithm. In this algorithm, the premise and consequent parameters are to be updated after each set of data that is presented into the algorithm. This is known as

pattern learning. The training algorithm consists of a forward pass and a backward pass. In the forward pass, the signal is moved forward until layer 4, and parameters are trained using least mean square method. On the other hand, in the backward pass, errors calculated will be passed back and the premise parameters will be adjusted using the gradient descent method.

3.6 Architecture of ANFIS and its basic learning rule

An adaptive neural network (see Figure 3.6) is a multilayer feedforward network in which each node performs a particular function called node function on incoming signals as well as a set of parameters pertaining to this node. The formulas for the node functions may vary from node to node, and the choice of each node function depends on the overall input-output function which the adaptive network is required to carry out [35]. The links in an adaptive network only indicate the flow direction of signals between nodes; no weights are associated with the links. To reflect different adaptive capabilities, circle and square nodes are used in an adaptive network. A square node which is an adaptive node has parameters while a circle node which is a fixed node has none. The parameter set of an adaptive network is the union of the parameter sets of each adaptive node. In order to achieve a desired input-output mapping, these parameters are updated according to given training data and a gradient-based learning procedure.

As an example, suppose that a given adaptive network has L layers and the k^{th} layer has k nodes. The node in the i^{th} position of the k^{th} layer can be denoted by k, i and its node function (or node output) by O_i^k. Since a node output depends on its

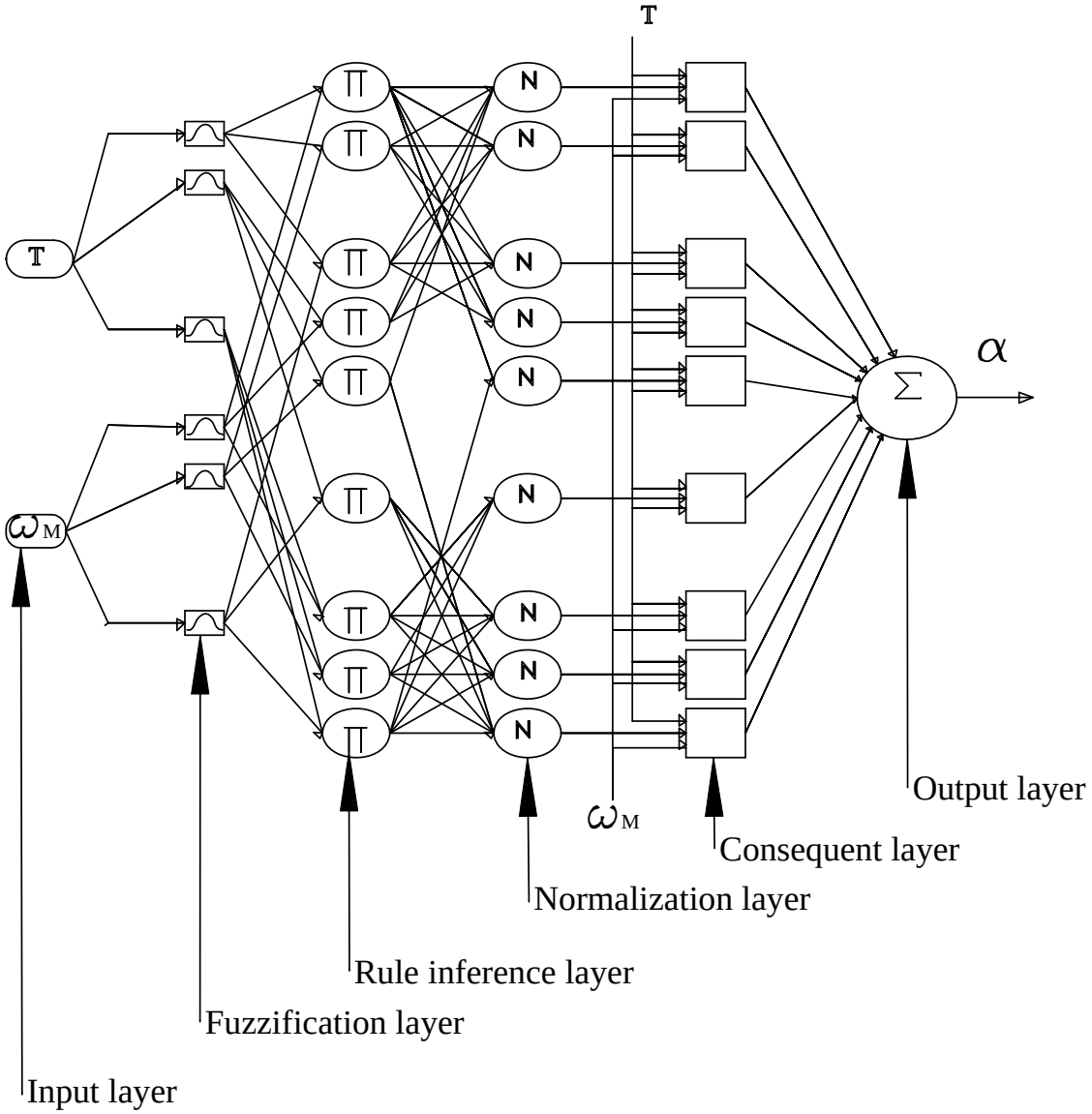

Figure 3.6: An Adaptive network

incoming signals and its parameter set, then;

$$O_i^k = O_i^k(O_i^{k-1}, ...O_{\sharp(k-1)}^{k-1}, a, b, c, ...) \tag{3.3}$$

where a, b, c, etc., are the parameters pertaining to this node, and $\sharp$ represents a number indicating the position of the node in the layer. O_i^k is used as both the node

output and node function.

Assuming that the given training data set has P entries, the error measure for the p^{th} $(1 \leq p \leq P)$ entry of training data can be defined as the sum of squared errors:

$$E_p = \sum_{m=1}^{\sharp(L)} (T_{m,p} - O_{m,p}^L)^2 \tag{3.4}$$

where $T_{m,p}$ is the m^{th} component of p^{th} target output vector, and $O_{m,p}^L$ is the m^{th} component of actual output vector produced by the presentation of the p^{th} input vector. The overall error measure is;

$$E = \sum_{p=1}^{P} E_p \tag{3.5}$$

In order to develop a learning procedure that implements gradient descent in E over the parameter space, first the error rate $\frac{\partial E}{\partial O}$ for p^{th} training data and for each node output O is calculated. The error rate for the output node at (L, i) can be calculated from [35]:

$$\frac{\partial E_p}{\partial O_{i,p}^L} = -2(T_{i,p} - O_{i,p}^L) \tag{3.6}$$

For the internal node at (k, i), the error rate can be derived by the chain rule:

$$\frac{\partial E_p}{\partial O_{i,p}^k} = \sum_{m=1}^{\sharp} (k+1) \frac{\partial E_p}{\partial O_{m,p}^{k+1}} \frac{\partial O_{m,p}^{k+1}}{\partial O_{i,p}^k} \tag{3.7}$$

where $1 \leq k \leq L$ - 1. That is, the error rate of an internal node can be expressed as a linear combination of the error rates of the nodes in the next layer. Therefore for all $1 \leq k \leq L$ and $1 \leq i \leq \sharp(k)$, we can find $\frac{\partial E_p}{\partial O_{i,p}^k}$ by equations 3.6 and 3.7. If α is a parameter of the given adaptive network, then equation 3.7 becomes;

$$\frac{\partial E_p}{\partial \alpha} = \sum_{O^* \in S} \frac{\partial E_p}{\partial O^*} \frac{\partial O^*}{\partial \alpha}, \tag{3.8}$$

where S is the set of nodes whose outputs depend on α. Then the derivative of the overall error measure E with respect to α is,

$$\frac{\partial E_p}{\partial \alpha} = \sum_{p=1}^{P} \frac{\partial E_p}{\partial \alpha} \tag{3.9}$$

Accordingly, the update formula for the generic parameter α is,

$$\Delta\alpha = -\eta \frac{\partial E}{\partial \alpha} \tag{3.10}$$

in which η is a learning rate. The learning rate can be further expressed as [35];

$$\eta = \frac{k}{\sqrt{\sum_{\alpha} (\frac{\delta E}{\partial \alpha})^2}} \tag{3.11}$$

where k is the step size, the length of each gradient transition in the parameter space. Usually, the value of k is changed to vary the speed of convergence.

There are two learning algorithms for adaptive networks. With the *batch learning* or *off-line learning*, the update formula for parameter α is based on equation 3.9 and the update action takes place only after the whole training data set has been presented, i.e., only after each *epoch* or *sweep*. On the other hand, if the parameters are to be updated immediately after each input-output pair has been presented, then the update formula is based on equation 3.8 and is referred to as the *pattern learning* or *on-line learning*.

3.7 Hybrid learning rule: Batch (off-line) learning

Hybrid learning rule combines the gradient method and the least squares estimate (LSE) to identify parameters [48]. If the adaptive network under consideration has

only one output, then

$$output = F(\vec{I}, S) \tag{3.12}$$

where $\vec{I}$ is the set of input variables and S is the set of parameters. If there exists a function H such that the composite function $H \circ F$ is linear in some of the elements of S, then these elements can be identified by the least squares method. More formally, if the parameter set S can be decomposed into two sets

$$S = S_1 \oplus S_2 \tag{3.13}$$

where $\oplus$ represents sum such that $H \circ F$ is linear in the elements of S_2, then upon applying H to equation 3.12, we have;

$$H(output) = H \circ F(\vec{I}, S) \tag{3.14}$$

which is linear in the elements of S_2. Now given values of elements of S_1, training data which can be denoted by P, can be input into equation 3.14 and a matrix equation obtained:

$$AX = B \tag{3.15}$$

where X is an unknown vector whose elements are parameters in S_2. Let $|S_2| = M$, then the dimensions of A, X and B are $P \times M, M \times 1$ and $P \times 1$, respectively. Since P, the number of training data pairs is usually greater than M, the number of linear parameters, this is an overdetermined problem, and generally there is no exact solution to equation 3.15. Instead, LSE of X and X^*, is sought to minimize the squared error $\|AX - B\|^2$. The most well-known formula for X^* uses the pseudo-inverse of X [50].

$$X^* = (A^T A)^{-1} A^T B \tag{3.16}$$

While equation 3.16 is concise in notation, it is expensive in computation when dealing with the matrix inverse and, moreover, it becomes ill defined if $A^T A$ is singular. As a result, sequential formulae are employed to compute the LSE of X. This sequential method of LSE is more efficient, especially when M is small and can be easily modified to an on-line version i.e., for systems with changing characteristics. Specifically, let the ith row vector of matrix A defined in equation 3.15 be a_i^T and the ith element of B be b_i^T, then X can be calculated iteratively using the following sequential formulae in [50, 51];

$$X_{i+1} = X_i + S_{i+1} a_{i+1} (b_{i+1}^T - a_{i+1}^T X_i) \tag{3.17}$$

$$S_{i+1} = S_i - \frac{S_i a_i + 1 a_{i+1}^T S_i}{1 + a_{i+a}^T S_i a_{i+1}} \qquad i = 0, 1, ..., (P-1) \tag{3.18}$$

where S_i is the covariance matrix, and the least squares estimate X^* is equal to X_p. The initial conditions to bootstrap equations 3.17 and 3.18 are $X_0 = 0$ and $S_0 = \gamma I$, where γ is a positive large number and I is the identity matrix of dimension $M \times M$. When dealing with multi-output adaptive networks, output in equation 3.12 is a column vector and equations 3.17 and 3.18 still apply except that b_i^T is the i^{th} row of matrix B.

The gradient method and the least squares estimate can be combined to update the parameters in an adaptive network. Each epoch of this hybrid learning procedure is composed of a forward pass and a backward pass. In the forward pass, input data is supplied and functional signals go forward to calculate each node's output until the matrices A and B in equation 3.15 are obtained. The parameters in S_2 are identified

by the sequential least squares formulas in equations 3.17 and 3.18. After identifying parameters in S_2, the functional signals keep going forward until the error measure is obtained. In the backward pass, the error rates or the differential error measure with respect to each node output, (see equations 3.6 and 3.7) propagate from the output end toward the input end, and the parameters in S_1 are updated by the gradient descent method in equation 3.10.

For given fixed values of parameters in S_1, the parameters in S_2 thus found are guaranteed to be the global optimum point in the S_2 parameter space due to the choice of the squared error measure. Not only does this hybrid learning rule decrease the dimension of the search space in the gradient method, but, in general, it also cuts down substantially the convergence time.

Taking an example of one-hidden-layer back-propagation neural network with sigmoid activation functions. If this neural network has p output units, then the output in equation 3.12 is a column vector. Let $H(\circ)$ be the inverse sigmoid function given by,

$$H(x) = \ln(\frac{x}{1-x}) \tag{3.19}$$

then equation 3.14 becomes a linear function such that each element of H is a linear combination of the parameters pertaining to layer 2. In other words, S_1 and S_2 are the thresholds of hidden and output layers, respectively. Therefore, the back-propagation learning rule can be applied to tune the parameters in the hidden layer, and the parameters in the output layer can be identified by the least squares method. However, by using the least squares method on the data transformed by $H(\circ)$, the

parameters that are obtained are optimal in terms of the transformed squared error measure instead of the original one.

3.8 Hybrid learning rule: Pattern (on-line) learning

If the parameters are updated after each data presentation, then this is referred to as pattern learning or on-line learning. This learning paradigm is vital to the on-line parameter identification for systems with changing characteristics. To modify the batch learning rule to its on-line version, the gradient descent should be based on E_p (see equation 3.7) instead of E.

For the sequential least squares formula to account for the time-varying characteristics of the incoming data, there is need to decay the effects of old data pairs as new data pairs become available. This problem is well studied in the adaptive control and system identification literature and a number of solutions are available [51]. The simplest method is to formulate the squared error measure as a weighted version that gives higher weighting factors to more recent data pairs. This amounts to the addition of a *forgetting factor* λ to the original sequential formula:

$$X_{i+1} = X_i + S_{i+1}a_{i+1}(b_{i+1}^T - a_{i+1}^T X_i) \tag{3.20}$$

$$S_{i+1} = \frac{1}{\lambda}[S_i - \frac{S_i a_i + 1 a_{i+1}^T S_i}{\lambda + a_{i+a}^T S_i a_{i+1}}] \qquad i = 0, 1, ..., P-1 \tag{3.21}$$

where the value of λ is between 0 and 1. The smaller λ is, the faster the effects of old data decay.

3.9 Application of ANFIS in the control of machining processes

Due to their ability to capture human knowledge and predict nonlinear and complex processes, adaptive neural fuzzy control systems have become an attractive alternative to conventional control systems in machining processes [47].

However, adaptive neural fuzzy inference systems are a relatively new technique. Although they have almost an unlimited capability in machining process control applications, they have mostly been employed in prediction systems.

CHAPTER 4

3 THEORETICAL ANALYSIS OF CHATTER VIBRATION IN THE CYLINDRICAL PLUNGE GRINDING PROCESS

4.1 Introduction

In this chapter, a theoretical model for the prediction of chatter vibrations is developed. First, a static force model is used to estimate the resultant and normal grinding forces at the initial state of excitation of the system.

An instantaneous dynamic model is used in the calculation of the tangential and normal components of velocity of the workpiece. These are in turn used for the calculation of normal and tangential forces, and finally the deflections in the respective directions. The dynamic model is developed based on the dynamic interaction of the grinding wheel and the workpiece.

4.2 Static model for the cylindrical plunge grinding process

Figure 4.1 shows a schematic representation of the static model for the cylindrical grinding process. In this figure, the inputs into the process are the grinding wheel surface velocity, v_g, workpiece surface velocity, v_w, and infeed rate, f_r. System stiffness, K_{eq}, is a process parameter which is a function of the grinding wheel and machine stiffness, K_s, and, the workpiece stiffness, K_w. The resultant tangential and normal grinding forces at the point of contact of the grinding wheel and the workpiece are indicated as F_t and F_n respectively. The grinding wheel and machine stiffness, (K_s),

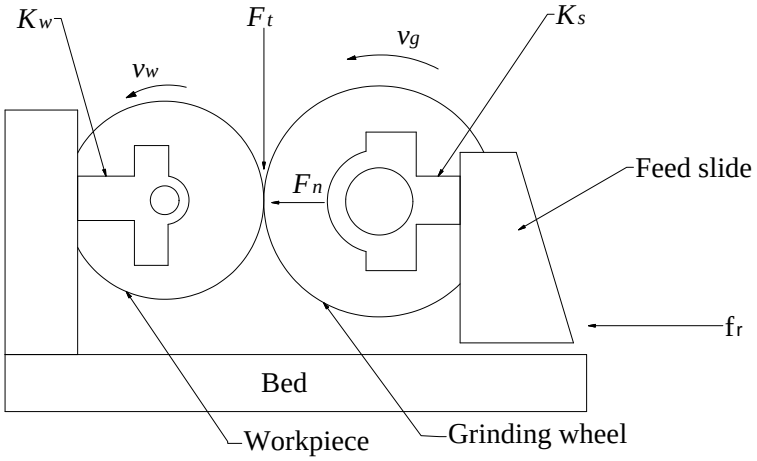

Figure 4.1: Schematic of cylindrical grinding

represent a pair of springs connected in series, i.e.,

$$K_s = \frac{K_g K_m}{K_g + K_m} \tag{4.1}$$

where K_m is the machine stiffness and K_g is the grinding wheel stiffness.

The cylindrical plunge grinding process dynamics can be represented as a mass-spring system, as shown in Figure 4.2. In this figure, M is the system mass, Z is the slide position, Y is the grinding wheel position and u represents all the input parameters into the cylindrical grinding process. The equivalent stiffness of the cylindrical grinding set up, denoted as K_{eq}, can be modeled as three springs in series as shown in equation 4.2.

$$\frac{1}{K_{eq}} = \frac{1}{K_m} + \frac{1}{K_g} + \frac{1}{K_w} \tag{4.2}$$

$$K_{eq} = \frac{(K_m K_g K_w)}{(K_m K_g + K_w K_g + K_m K_w)} \tag{4.3}$$

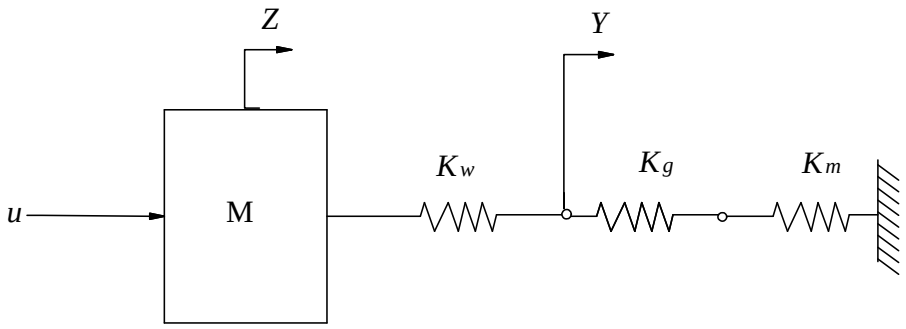

Figure 4.2: Spring mass representation of the cylindrical grinding process

where K_w is the stiffness of the workpiece. From Figure 4.2 the resultant workpiece-grinding wheel deflection / displacement δ can be given as;

$$\delta = Z - Y \tag{4.4}$$

The material removal rate, M_{rr}, can be determined as [52];

$$M_{rr} = \pi b_s d_w f \tag{4.5}$$

where b_s is the width of the grinding wheel, d_w is the diameter of the workpiece and f is the actual infeed, which is different from the control infeed, f_r. For a constant radial feed, the relationship between the control infeed and the actual infeed is given by the equation;

$$f_r - f = \frac{d}{dt}(\frac{F_n}{K_{eq}}) \tag{4.6}$$

The normal force, F_n, can be approximated as [52];

$$F_n = c\pi d_w b_s f \tag{4.7}$$

where c is the proportionality constant describing the grinding wheel's dullness (which ranges between 0.1 and 1).

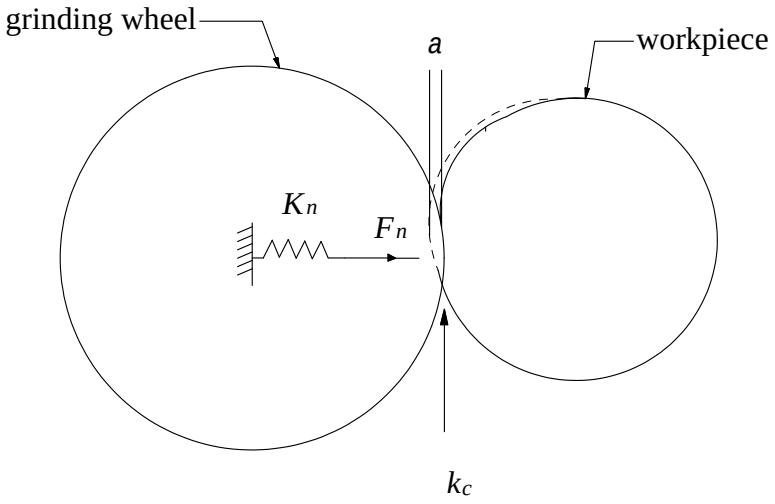

Figure 4.3: Interaction of wheel and workpiece

Assuming a linear cutting force model, the following relationship can be used to describe the cylindrical grinding system [53].

$$F_n = K_{eq}\delta \tag{4.8}$$

where F_n is the normal force, and δ is the resultant deflection. From Figure 4.3 the normal force can also be approximated as [54];

$$F_n = k_c \times a = K_n \times \delta \tag{4.9}$$

where a is the instantaneous depth of cut and k_c is the grinding coefficient which is a function of workpiece material properties, grinding wheel formulation, coolant, etc. K_n is the normalized normal grinding force coefficient. k_c can be obtained from the relationship shown in [54] and [55];

$$k_c = \mu \times e_c \times \frac{\Omega_w \times R_w}{\Omega_g \times R_g} \tag{4.10}$$

where Ω_w and Ω_g are the rotational speeds for the workpiece and the grinding wheel, μ is the coefficient of grinding and, R_w and R_g are the radii of the workpiece and the grinding wheel respectively. The specific grinding energy e_c i.e., the energy that must be expended to remove a unit volume of workpiece material, given by the equation;

$$e_c = \sqrt{\frac{v_g}{v_w}.C.r\sqrt{\frac{d_e}{a_e}}} \tag{4.11}$$

In equation 4.11, v_g and v_w represent wheel and workpiece surface velocities, while C is the active grit density and r is the grit cutting point shape factor (ratio of grit thickness to its width), d_e the equivalent wheel diameter, and a_e the equivalent depth of cut. The equivalent diameter is given by the relationship in [56];

$$d_e = \frac{d_g \times d_w}{d_g + d_w} \tag{4.12}$$

where d_g is the diameter of the grinding wheel.

The coefficient of grinding, μ, is a function of the normal and tangential grinding forces given by [8];

$$\mu = \frac{F_t}{F_n} \tag{4.13}$$

where F_t is the tangential grinding force. The resultant grinding force, F, can be calculated by the formula shown in [54];

$$F = e_c \times a \times \frac{\Omega_w}{\Omega_g}\frac{R_w}{R_g} \tag{4.14}$$

4.3 Dynamic model for the cylindrical plunge grinding process

In the dynamic model, chatter vibration is assumed to be a two dimensional problem as shown in Figure 4.4. In the figure, an arbitrary coordinate system is used with

X and Y as the two orthogonal axes. The coordinate system depends on the instantaneous positions of the grinding wheel and the workpiece. During the grinding process, the coordinate system is displaced (rotated) to the X' and Y' positions for the X and Y axes respectively. The displacement along the X axis is indicated as $(X_g - X_w)$, while that along the Y axis is indicated as $(Y_g - Y_w)$. β_w represents the angular displacement for the workpiece and β_g shows the angular displacement for the grinding wheel. ψ is the angular displacement of the grinding wheel relative to the fixed workpiece coordinate system, herein referred to as phase shift. After an infeed f, the following relationship holds for the displacement in the X direction;

$$(X_g - X_w) = \{R_w \sin(\beta_w - \psi) + R_g \sin(\beta_g - \psi) - ft\} \cos\psi \tag{4.15}$$

For small β, $\sin\beta \cong \beta$, hence,

$$(X_g - X_w) = \{R_w(\beta_w - \psi) + R_g(\beta_g - \psi) - ft\} \cos\psi \tag{4.16}$$

Also for the displacement in the y direction, the following relationship holds,

$$(Y_g - Y_w) = \{R_g(\beta_g - \psi) + R_w(\beta_w - \psi) - ft\} \sin\psi \tag{4.17}$$

Differentiation of equations 4.16 and 4.17 with respect to time, yields the velocity terms in both the X and Y directions respectively;

$$\begin{aligned}(\dot{X}_g - \dot{X}_w) =& \{R_g(\Omega_g - \dot{\psi}) + R_w(\Omega_w - \dot{\psi}) - f\} \cos\psi \\ & - \{R_w(\beta_w - \psi) + R_g(\beta_g - \psi) - ft\} \sin\psi\end{aligned} \tag{4.18}$$

$$\begin{aligned}(\dot{Y}_g - \dot{Y}_w) =& \{R_g(\Omega_g - \dot{\psi}) + R_w(\Omega_w - \dot{\psi}) - f\} \sin\psi \\ & + \{R_w(\beta_w - \psi) + R_g(\beta_g - \psi) - ft\} \cos\psi\end{aligned} \tag{4.19}$$

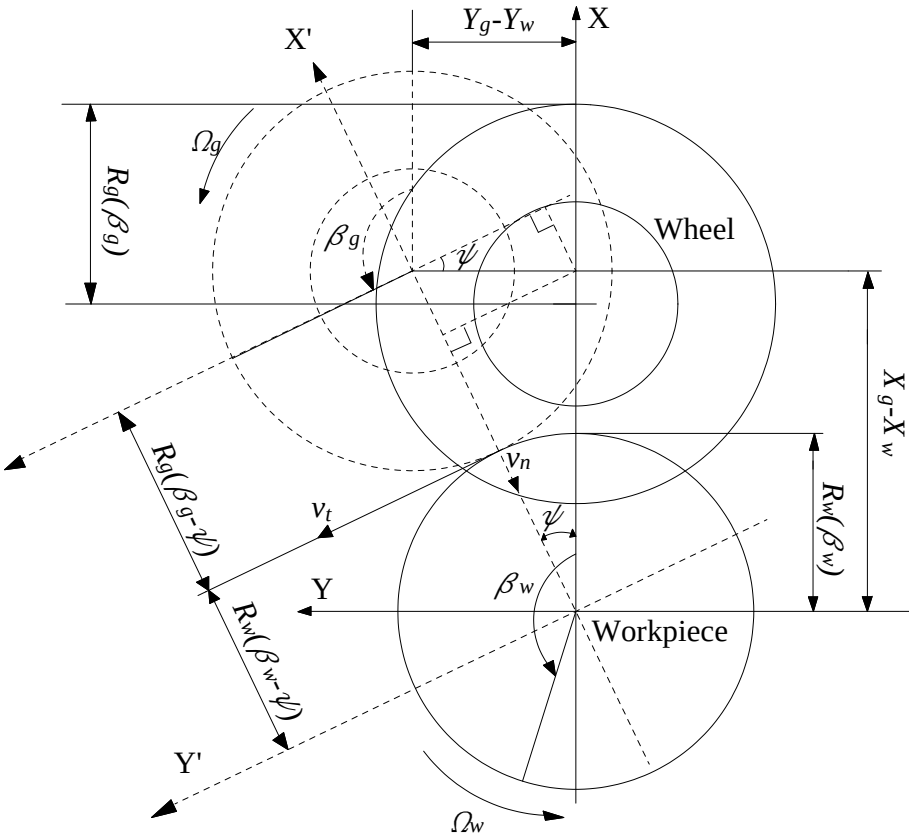

Figure 4.4: Kinematics of a plunge grinding process

The phase shift ψ can be obtained from the following geometric relation,

$$R_g + R_w = R_g(\beta_g - \psi) + R_w(\beta_w - \psi) \tag{4.20}$$

from which the expression for ψ becomes,

$$\psi = \frac{R_g\beta_g + R_w\beta_w - R_g - R_w}{R_g + R_w} \tag{4.21}$$

The instantaneous velocity terms v_t and v_n in the tangential and normal directions respectively, are,

$$v_t = \Omega_w R_w(\beta_w - \psi) + (\dot{x}_g - \dot{x}_w)\sin\psi - (\dot{y}_g - \dot{y}_w)\cos\psi \tag{4.22}$$

and

$$v_n = -(\dot{x}_g - \dot{x}_w)\cos\psi + (\dot{y}_g - \dot{y}_w)\sin\psi \tag{4.23}$$

The dynamic model for the cylindrical plunge grinding process assumes distributed force along the wheel/workpiece contact. The contact length along the wheel is discretized into segments and each segment subtends an angle $\Delta\beta_i$, at the center of the wheel, as shown in Figure 4.5. The normalized instantaneous chip thickness, C_t can be given as [57];

$$C_t = 2\pi\frac{v_t}{\Omega_g}\sin\Delta\beta_{g_i} + 2\pi\frac{v_n}{\Omega_g}\cos\Delta\beta_{g_i} \tag{4.24}$$

The specific forces per unit width of each contacted segment in radial and tangential directions can be represented as functions of the normalized chip thickness, C_t in the form

$$\begin{pmatrix} f'_n \\ f'_t \end{pmatrix} = \begin{pmatrix} K_n \\ K_t \end{pmatrix} C_t(R_g, \Delta\beta_{g_i}), \tag{4.25}$$

where

$$\begin{aligned} f'_n =& \frac{2\pi}{\Omega_g} K_n\{[\Omega_w R_w(\beta_w - \psi) - \{R_g(\beta_g - \psi) + R_w(\beta_w - \psi)\} + ft]\sin\beta_g \\ &+ [\{R_g(\Omega_g - \dot{\psi}) + R_w(\Omega_w - \dot{\psi}) - f\}(-\cos 2\psi) + \{R_g(\beta_g - \psi) \\ &+ R_w(\beta_w - \psi)\}\sin 2\psi - 2ft\sin\psi\cos\psi]\cos\beta_g\}, \end{aligned} \tag{4.26}$$

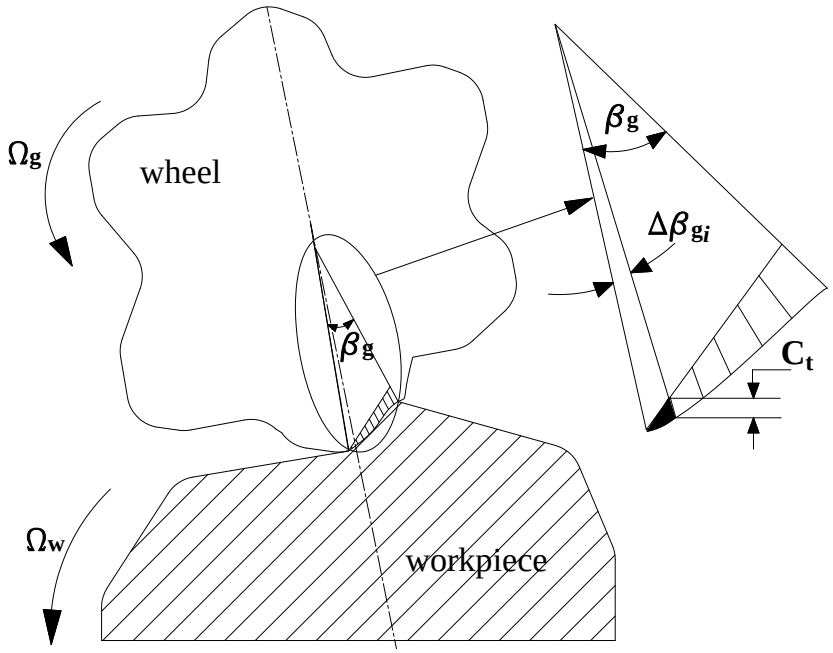

Figure 4.5: Geometrical interaction between wheel and workpiece

and

$$\begin{aligned} f_t' =& \frac{2\pi}{\Omega_g} K_t \{ [\Omega_w R_w(\beta_w - \psi) - \{R_g(\beta_g - \psi) + R_w(\beta_w - \psi)\} + ft] \sin\beta_g \\ &+ [\{R_g(\Omega_g - \dot{\psi}) + R_w(\Omega_w - \dot{\psi}) - f\}(-\cos 2\psi) + \{R_g(\beta_g - \psi) \\ &+ R_w(\beta_w - \psi)\} \sin 2\psi - 2ft \sin\psi \cos\psi] \cos\beta_g \} \end{aligned} \tag{4.27}$$

The constants K_n and K_t are the normalized force coefficients for the radial and tangential directions respectively. The total segment forces F_n' and F_t' in the normal and tangential directions respectively, can be obtained by summing up the segmental forces in the respective directions, i.e.,

$$\begin{pmatrix} F_n' \\ F_t' \end{pmatrix} = \sum_{i=1}^{N} \begin{pmatrix} K_n \\ K_t \end{pmatrix} C_t(R_g \Delta\beta_{g_i}); \qquad \text{where} \quad N = \text{int}\big(\frac{\beta_g}{\Delta\beta_{g_i}}\big) \tag{4.28}$$

The total specific grinding forces F_n and F_t in the X and Y directions can be calculated by transforming the total segment forces, F'_n and F'_t in the Cartesian coordinate system;

$$\begin{pmatrix} F_n \\ F_t \end{pmatrix} = \begin{bmatrix} \cos(\beta_g + \psi) & -\sin(\beta_g + \psi) \\ \sin(\beta_g + \psi) & \cos(\beta_g + \psi) \end{bmatrix} \times \begin{pmatrix} F'_n \\ F'_t \end{pmatrix} \tag{4.29}$$

Therefore, the values of F_n and F_t can be obtained as;

$$\begin{pmatrix} F_n \\ F_t \end{pmatrix} = \begin{pmatrix} F'_n \cos(\beta_g + \psi) - F'_t \sin(\beta_g + \psi) \\ F'_n \sin(\beta_g + \psi) + F'_t \cos(\beta_g + \psi) \end{pmatrix} \tag{4.30}$$

The deflections δ_n and δ_t in the normal and tangential directions, respectively, can be obtained as follows;

$$\delta_n = F_n / K_{eq} \tag{4.31}$$

$$\delta_t = F_t / K_{eq} \tag{4.32}$$

Where K_{eq} is the dynamic grinding stiffness which was determined experimentally as detailed in APPENDIX A. The deflection δ can, therefore, be obtained as shown in the following equation;

$$\delta = \delta_n \sqrt{\mu^2 + 1} \tag{4.33}$$

4.3.1 Theoretical results of displacements

A computer program shown in APPENDIX B was used to solve equations 4.31 and 4.32 for the normal and tangential displacements. The flowchart of the program is shown in Figure 4.6. The values of the parameters that were used are shown in Table 4.1. The coefficient of grinding, μ, was determined experimentally as detailed

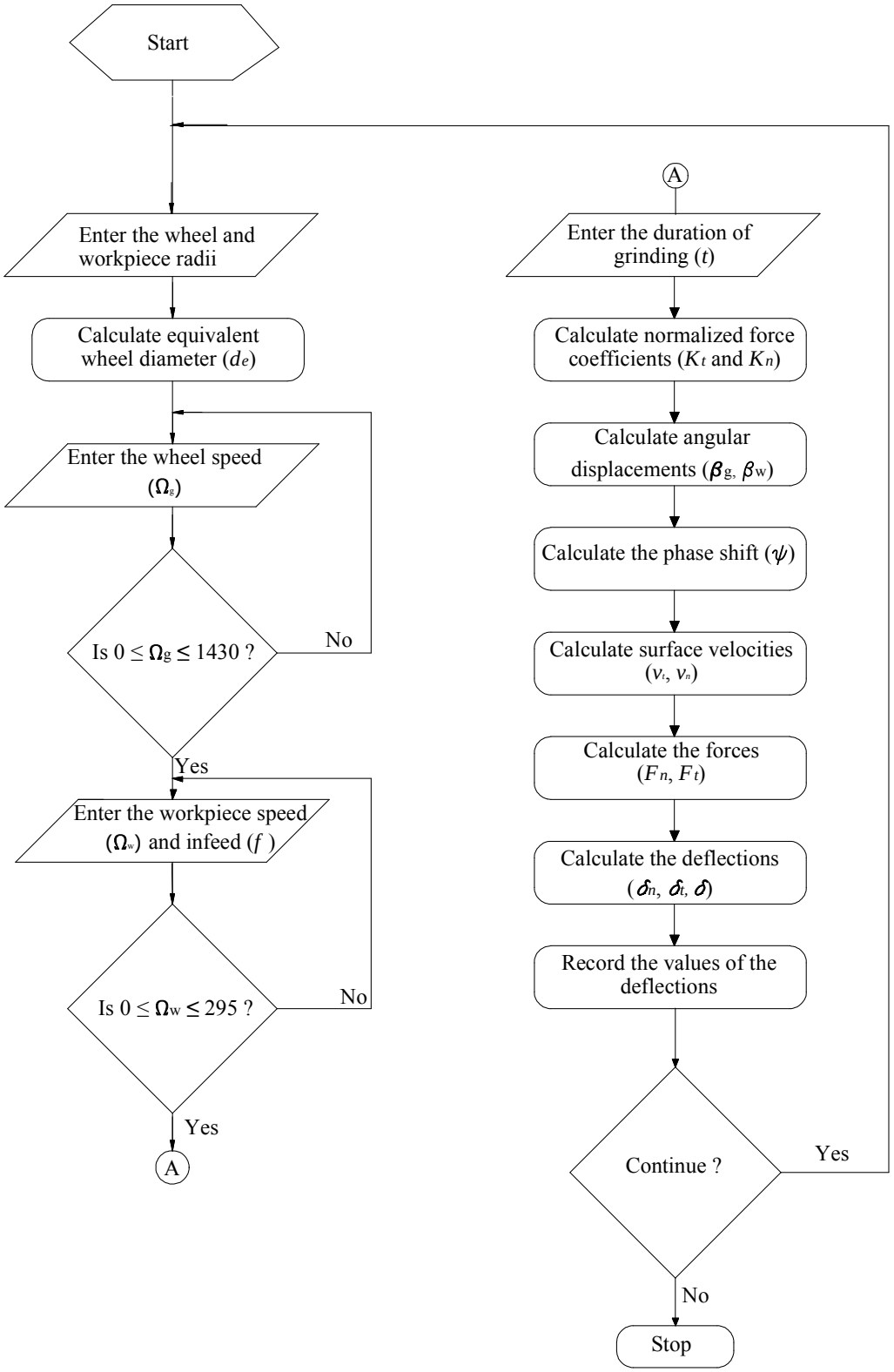

Figure 4.6: Flowchart for the execution of the simulation program.

Table 4.1: Grinding parameters

Parameter	**Value**
Active grit density (C)	9.5
Coefficient of grinding (μ)	0.5
Grit shape factor (r)	1
Grinding wheel diameter (d_g)	405 mm
Workpiece diameter (d_w)	30 mm

in APPENDIX C, and the grit shape factor assumed to be of uniform grit. The grit density for B126 CBN grinding wheel is $9.5/\text{mm}^2$.

The grinding wheel speed was taken to vary between 0 rpm and 1430 rpm and workpiece speed was taken to vary between 55 rpm and 295 rpm. This was done so as to make them correspond to those of the machine used in the experiments.

Figures 4.7 - 4.8 show the displacements of the grinding wheel in the normal direction. It can be noted from these figures that, the amplitudes of vibration are in the order of 10^{-1} μm. An interesting phenomenon is seen in Figure 4.7 (a), in which there is growth of amplitudes of vibration (displacement) in every cycle. This can be attributed to the regenerative effect of chatter vibration, which causes the amplitude to increase in each consecutive cycle. This occurs due to the fact that, initially, cutting forces excite a vibration of the machine workpiece system.

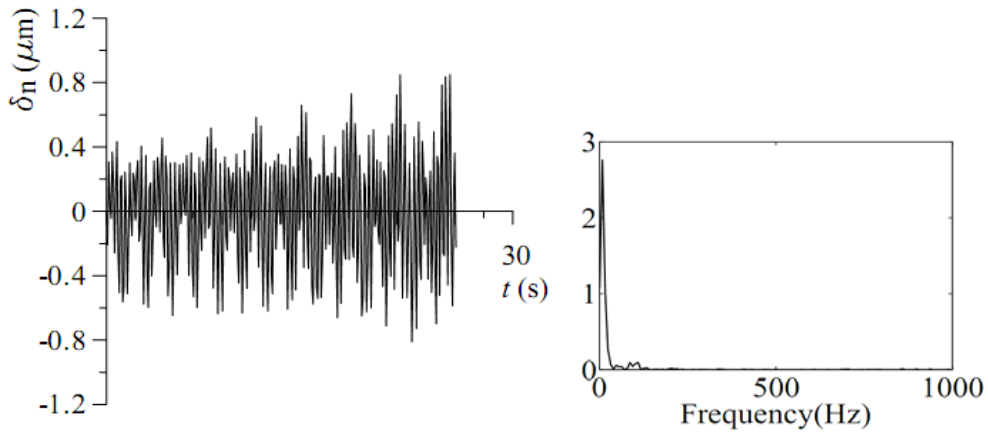

(a) displacements: the RMS value is 0.4689 (b) power spectrum

Figure 4.7: Vibration at wheel speed of 1430 rpm and workpiece speed of 295 rpm and infeed of 0.05 mm

This leaves a wavy surface finish on the workpiece. During the next revolution, another wavy surface is produced in the same way. Depending on the phase shift between these two waves, the maximum chip thickness can grow and oscillate at a particular frequency that is close to the natural frequency of the machine workpiece system [4].

From Figure 4.7 (b), power spectrum shows the frequencies of vibration at 1 Hz and 100 Hz. These multiple modes of vibration are due to the fact that, the waviness and roughness generated on the workpiece surface vary due to the cutting conditions, such as, the grinding wheel and workpiece speeds, and infeed. The presence of the regeneration effect in the grinding process also contributes to the presence of multiple modes of vibration [17]. Regeneration occurs when the waves generated on the work-

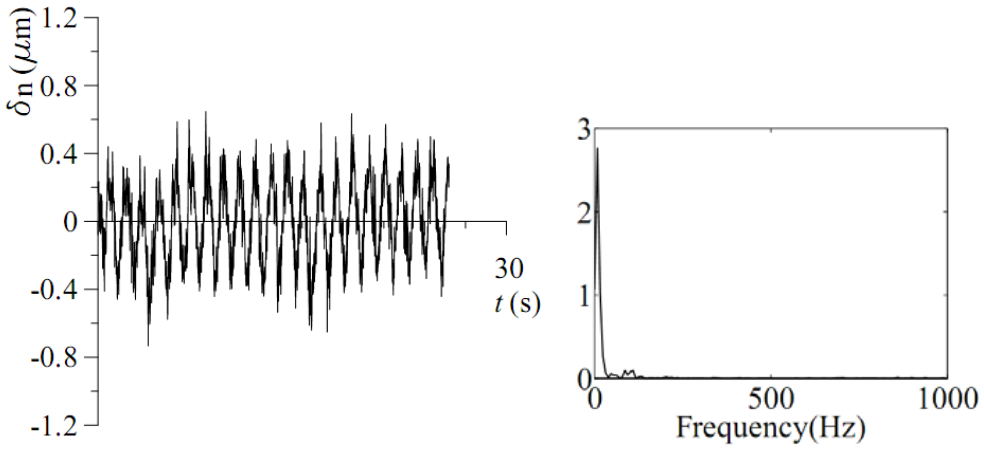

(a) displacement: the RMS value is 0.2344 (b) power spectrum

Figure 4.8: Displacements at wheel and workpiece speeds of 1430 rpm and 55 rpm, respectively and infeed of 0.05 mm

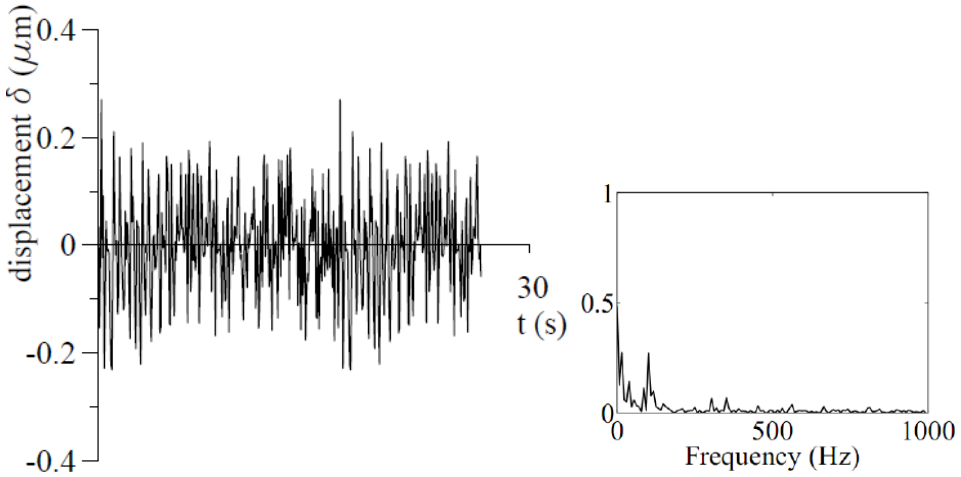

(a) displacements: the RMS value is 0.4123 (b) power spectrum

Figure 4.9: Displacements at an infeed of 0.07 mm (wheel speed and workpiece speed are 1430 rpm and 295 rpm, respectively)

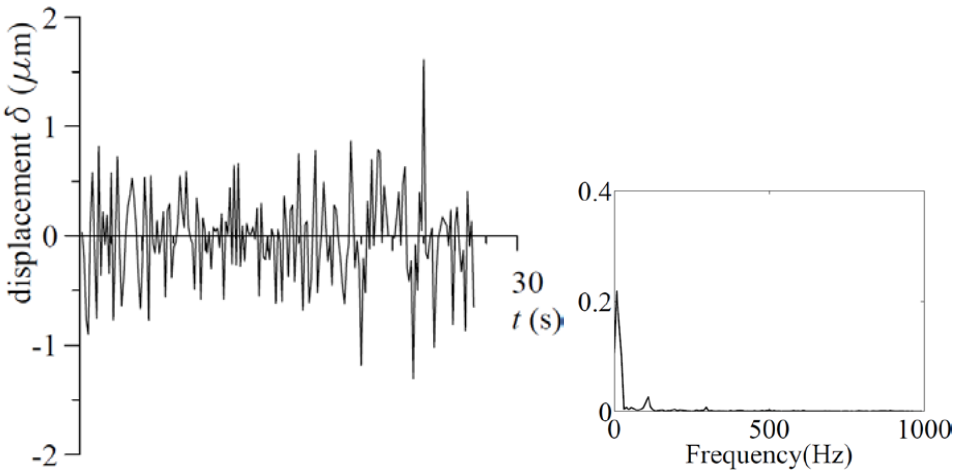

(a) displacements: the RMS value is 0.0968 (b) power spectrum

Figure 4.10: Displacements at an infeed of 0.03 mm (wheel speed and workpiece speed are 1430 rpm and 295 rpm, respectively)

piece as well as on the grinding wheel surfaces envelop the relative vibration between them.

Comparing Figures 4.7 and 4.8, and the RMS values for the two cases, it can be seen that reduction in the workpiece speed causes variation in the vibration amplitudes, in this case, a decrease. Other results, shown in Figures 4.9 and 4.10 indicate a decrease in the vibration amplitude with decrease in infeed.

The effectiveness of the model in predicting vibration amplitudes, represented by the RMS values, and the frequencies of vibration obtained from power spectral analysis, is validated through a series of experiments described in the next chapter.

CHAPTER 5

4 MEASUREMENT OF VIBRATIONS IN GRINDING

5.1 Introduction

This chapter describes a series of experiments that were carried out to test the validity of the theoretical model for cylindrical plunge grinding process, that was presented in chapter three.

5.2 Apparatus and experimental procedure

The grinding experiments were carried out on a universal HIGH-GLOSS 450-H grinding machine from Kondo Machine Works Co. Ltd., Japan. The machine has a spindle rotational speed of 1430 rpm and a workpiece rotational speed that can be adjusted to either 55 rpm, 130 rpm, 215 rpm or 295 rpm. The machine has a provision for feeding in two orthogonal axes, that is X and Y, and can be automatically fed in the X direction only. The minimum infeed attainable was 0.01 mm. A B126 Cubic Boron Nitride (CBN) wheel with a grit density of $9.5/\text{mm}^2$, outer diameter of 405 mm, inner diameter of 203 mm and thickness of 75 mm was used. A contact type displacement sensor, DT-10D, with a range of 10 mm and a piezo-electric dynamometer (AST-MH) were used for displacement and force measurements, respectively.

Before any measurements were made, the displacement sensor and the tool dynamometer were calibrated as indicated in APPENDIX D. Measurements of forces and displacements were taken simultaneously in order to determine the dynamic

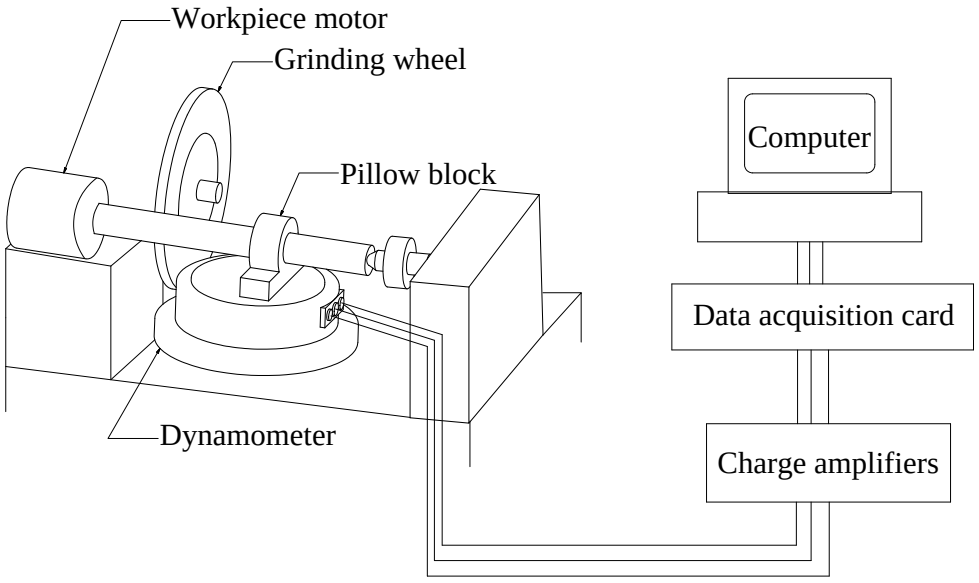

Figure 5.1: Schematic of the experimental setup

grinding stiffness. The displacement and force signals were recorded in a computer via a Peripheral Component Interconnect (PCI) data acquisition card (NI PCI-6259), which was connected to a displacement and strain amplifier via a 68-pin shielded connector block (NI SCB-68 pin). LabVIEW® software was used for data acquisition. A schematic diagram of the experimental apparatus for the measurement of cutting forces is shown in Figure 5.1.

The displacements in the normal and tangential directions were recorded for different combinations of grinding wheel and workpiece speeds, and for two different materials. A photograph of the machine setup is shown in Figure 5.2. Also a screen shot for the LabVIEW environment used for data collection is shown in figure 5.3.

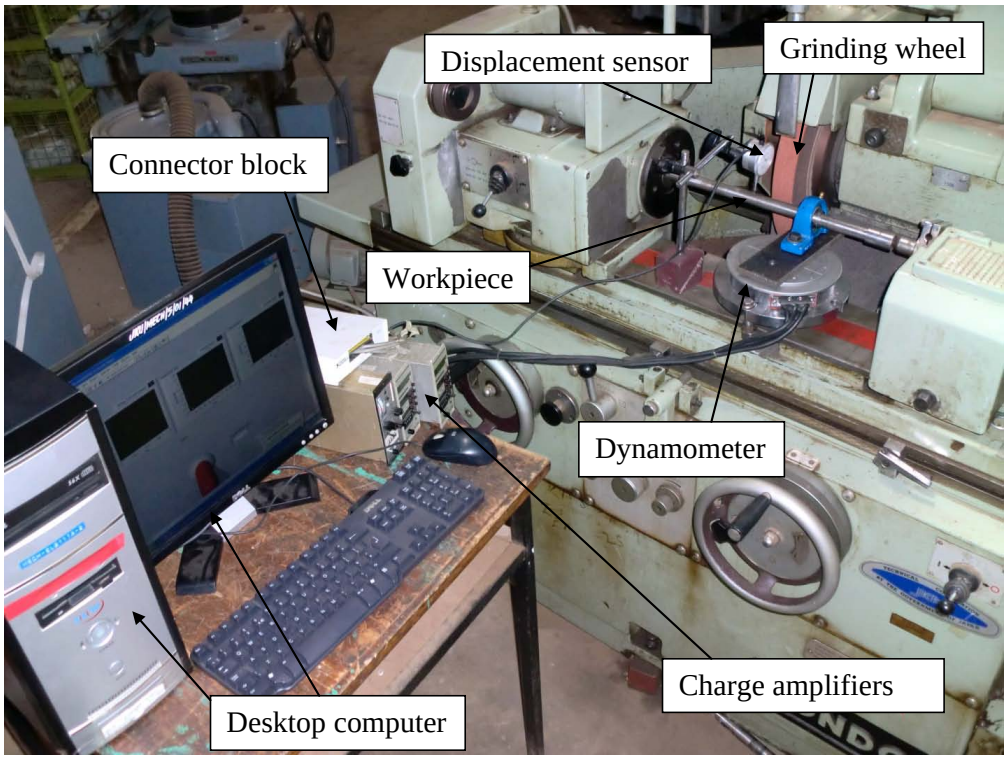

Figure 5.2: Experimental setup for measurement of displacements

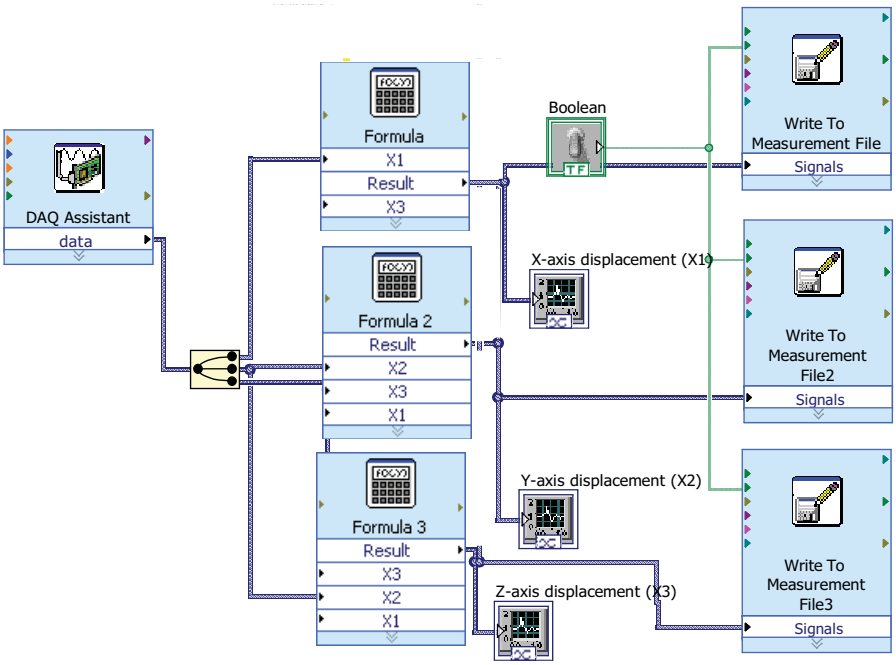

Figure 5.3: Screen shot of the LabVIEW environment used for data collection

5.3 Model validation

Figures 5.4 - 5.6 show waveforms of predicted and measured normal displacements for two sets of workpiece and grinding wheel speeds. Also, shown in the figures are the power spectra for the corresponding vibrations. From the power spectral analysis it can be seen that, there are more vibration modes during the grinding process, than in the model predictions.

This could be attributed to vibrations from the machine structure. The RMS values for each of the given cases indicate that the predicted values at lower grinding speeds are closer to the experimental values than at higher speeds. This is due to the fact that, while grinding at high speeds, there is generation of higher temperatures which contribute to higher grit breakage as shown in the relationship 5.1, [8].

$$T \alpha \sqrt{a_e.v_s.C.r} \tag{5.1}$$

where T is the temperature at the contact surface, a_e is the depth of cut (the depth of work material removed per revolution), v_s is the surface velocity of the grinding wheel, C is the active grit density and r is the grit cutting point shape factor. This effect was not accounted for in the model.

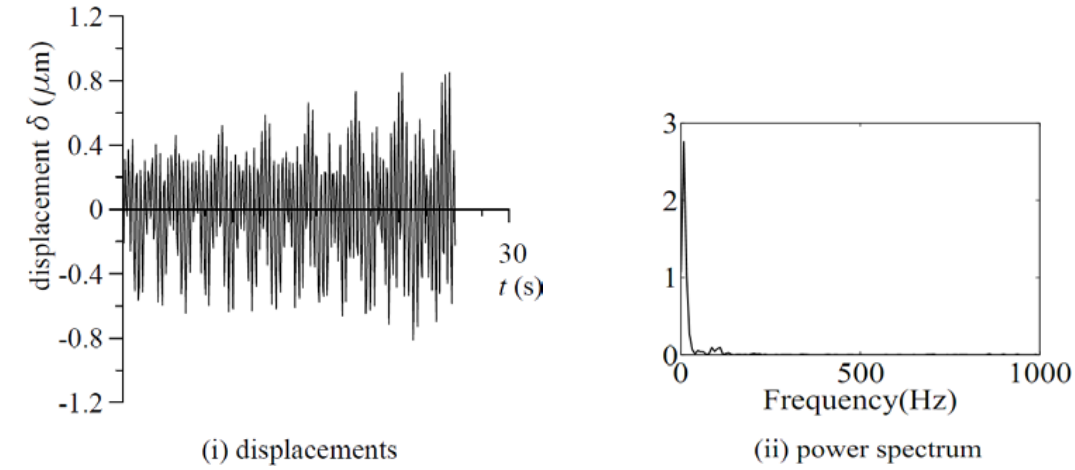

(a) predicted displacements: the RMS value is 0.4689

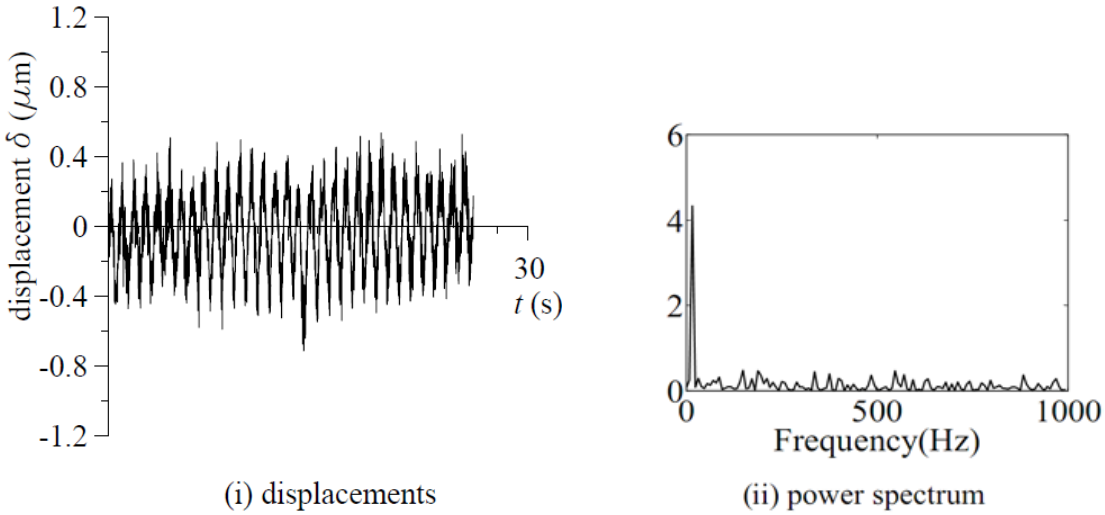

(b) measured displacements: the RMS value is 0.2199

Figure 5.4: Vibrations in grinding (grinding wheel speed, 1430 rpm; workpiece speed, 295 rpm; infeed 0.05 mm)

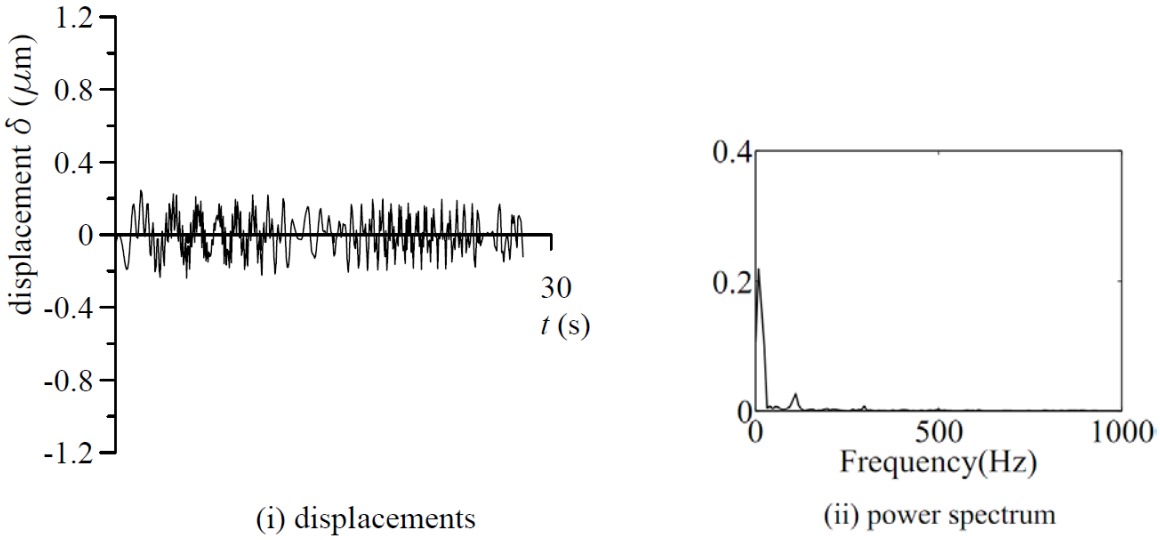

(a) predicted displacements: the RMS value is 0.1039

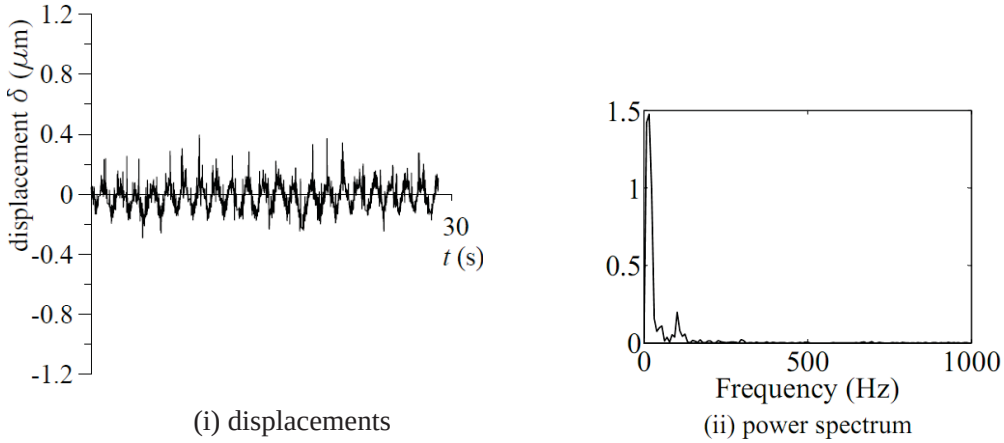

(b) measured displacements: the RMS value is 0.0824

Figure 5.5: Vibrations in grinding (wheel speed, 700 rpm; workpiece speed, 130rpm; infeed, 0.05 mm)

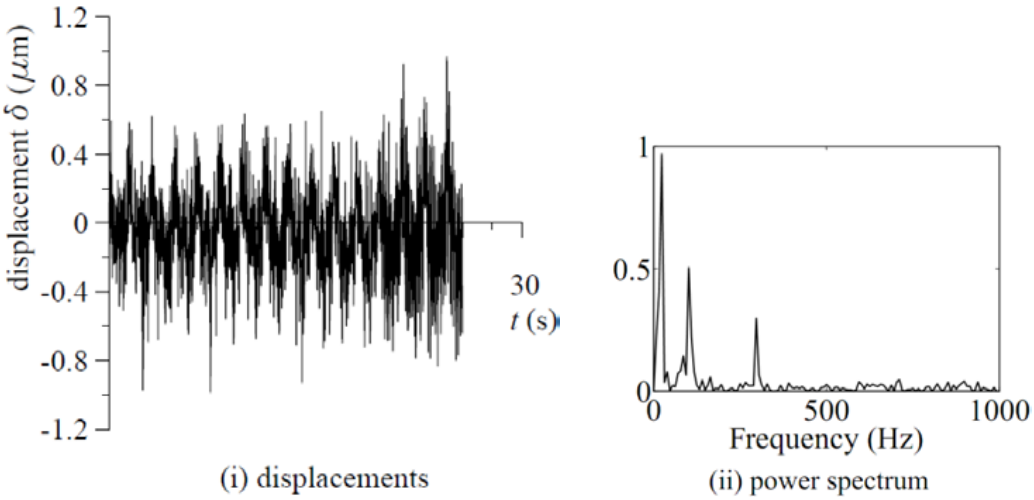

(a) predicted displacement: the RMS value is 0.2635

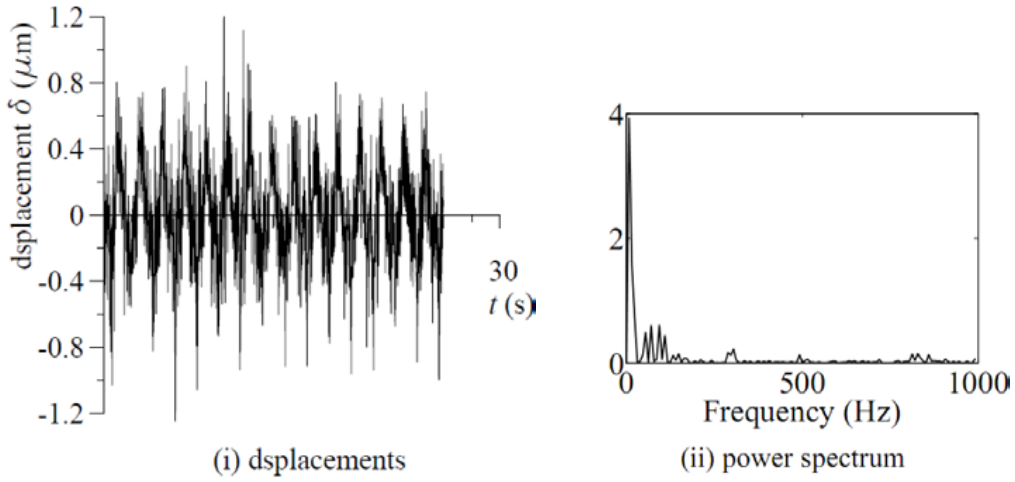

(b) measured: the RMS value is 0.2941

Figure 5.6: Vibrations in grinding (wheel speed, 500 rpm; workpiece speed, 295 rpm; infeed, 0.05 mm)

5.3.1 Effect of variation of workpiece speed on vibration amplitudes

The workpiece speed was varied in order to investigate its effect on the vibration amplitudes at grinding wheel speed of 1430 rpm and an in-feed of 0.05 mm. The results are as shown in Figure 5.7. In this figure the variation of the predicted values of vibration from the measured values is within 15-20 percent. This also shows there is great correlation between the measured and the predicted values. It can also be seen that, the lowest values of the vibration amplitudes are obtained at a workpiece speed of and 55 rpm, while the highest predicted and measured values of the displacement are at workpiece speeds of 295 rpm and 130 rpm, respectively. This phenomenon could be explained by the fact that, the model assumed a fully elastic system, while in actual sense, the system is not fully elastic.

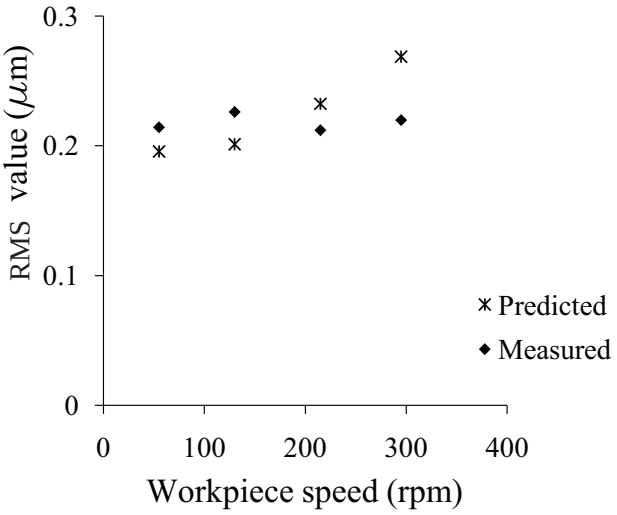

Figure 5.7: Variation of RMS values of displacements with workpiece speed in grinding mild steel (wheel speed; 1430 rpm, infeed; 0.05 mm)

5.3.2 Effect of variation of wheel speed on vibration amplitudes

Analysis on the effect of variation of wheel speed on amplitudes of vibration shows similar results as for the effect of the variation of workpiece speed for grinding mild steel, that is, non-linear relationship between the amplitudes of vibration and the wheel speed as shown in Figure 5.8.

Again from the figure, the variation of the predicted displacements from the measured displacements is within 15-20 percent range. It is also seen on this figure that, the lowest values of the vibration amplitudes (displacements) are obtained at grinding wheel speed of 700 rpm, while the highest predicted and measured values of displacements are at wheel speeds of 1200 rpm and 500 rpm, respectively. As noted, the grinding process varies randomly, due to the fact that the process parameters change with time, and there are complex relationships between them [18].

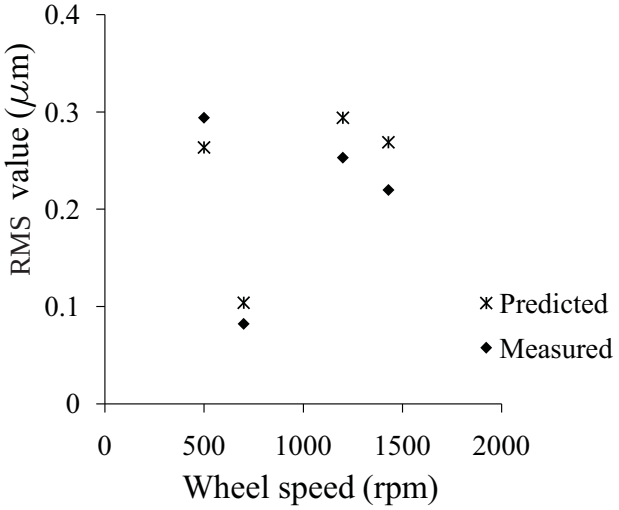

Figure 5.8: Variation of RMS values of displacements with wheel speed in grinding mild steel (workpiece speed; 130 rpm, infeed; 0.05 mm)

5.3.3 Effect of variation of infeed on vibration amplitudes

The in-feed was varied with the workpiece and wheel speed at 295 rpm and 1430 rpm, respectively, in order to investigate the effect of variation of in-feed on the vibration amplitudes.

The predicted and measured values of displacement indicate that, vibration amplitudes increase nonlinearly with in-feed and are withn 15-20 percent range. From Figure 5.9, the highest value of the displacement occur at in-feed of 0.07 mm and the lowest occur at in-feed of 0.01 mm in grinding mild steel. As is expected, increasing the feed means increasing the load on the workpiece, and hence, the higher the feed, the higher the deflections [56]. From the three cases considered above, it can be seen that, the model predictions vary from the measured values with up to a maximum of 0.05 μm.

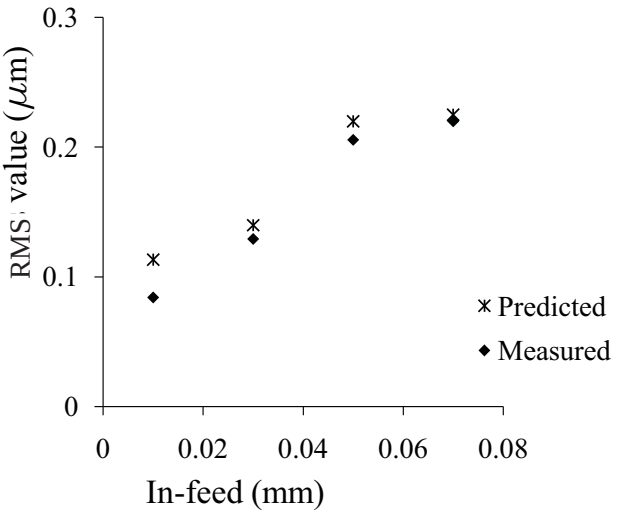

Figure 5.9: Variation of RMS values of displacements with infeed in grinding mild steel

It can be seen from Figures 5.7 - 5.9 that,

- a change in either the wheel or the workpiece speed causes change in the vibration amplitudes and the number of vibration modes in an unpredictable manner. This could be attributed to the variation of the process parameters associated with the complex nature of the process [18].

- increase in infeed causes increase in amplitudes of vibration and decrease in infeed causes decrease in amplitudes of vibration [9].

- the vibration amplitudes from model the prediction are within a ± 0.03 μm tolerance from the measured values.

- the model predicted values of vibration follow a similar pattern to those of the experimental measurement.

CHAPTER 6

5 DESIGN OF ADAPTIVE NEURAL FUZZY INFERENCE SYSTEM AND FUZZY LOGIC CONTROLLER

6.1 Introduction

This chapter outlines the procedure for designing, training, testing and implementing the ANFIS based fuzzy logic controller. The ANFIS based FLC is applied because of its ability to improve both the system performance and adaptability. A set of training data is presented to the ANFIS. Then, the membership functions, their number, and the rule base for the FLC are obtained from the ANFIS, and are used for tuning the fuzzy logic controller. The fuzzy logic controller works in a closed loop to control the vibrations resulting from the grinding process by selecting the appropriate grinding parameters based on the inputs from the displacement sensors.

6.2 Fuzzy logic controller design

The proposed controller has two inputs, namely, the amplitude of vibration in the normal direction (δ_n) and in the tangential direction (δ_t). Figure 6.1 shows the block diagram for the proposed fuzzy logic controller.

The Fuzzy logic controller design involves the following steps;

- Identification of the inputs, outputs and their ranges.
- Design of the fuzzy membership functions for each input and output by the use of ANFIS.

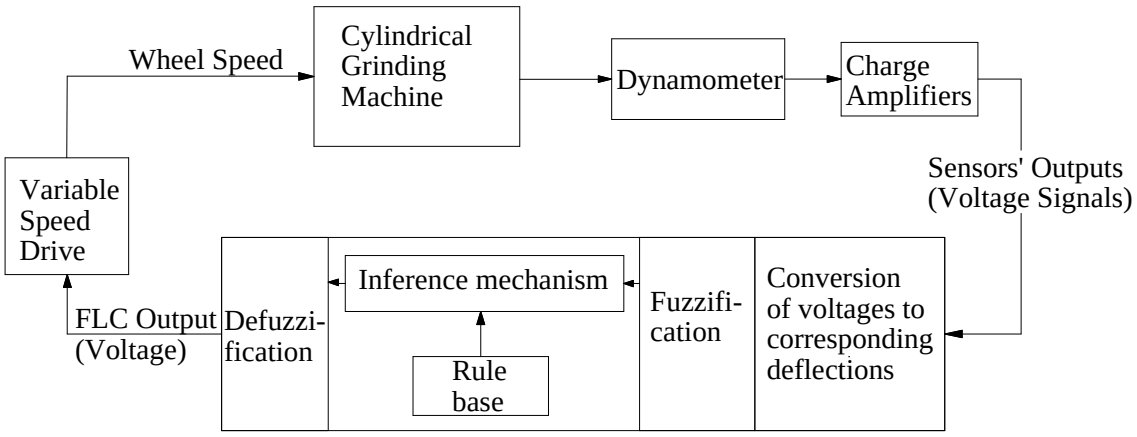

Figure 6.1: Schematic diagram for the control of cylindrical grinding process using FLC

- Construction of the knowledge base that contains the fuzzy rules which are used for fuzzy reasoning. The knowledge base is constructed by ANFIS.

- Mapping of the fuzzy logic controller's output to the corresponding crisp values by use of center of gravity defuzzification procedure.

6.2.1 Identification of inputs, outputs and their ranges

The inputs into the fuzzy logic controller are the amplitudes of the displacements in the normal and tangential directions, that is, δ_n and δ_t respectively. The displacements were chosen to range from negative 10 μm to positive 10 μm. These values were arrived at from the experimental work, in which the highest value of displacement was seen to be around 4 μ m. The output of the FLC is the grinding wheel speed which ranges from 0 rpm to 1430 rpm.

6.2.2 Design of membership functions and the rule base

The design of membership functions is achieved by use of ANFIS as follows:

- A set of training data, which constitutes the optimum grinding conditions and the expected output, is presented to the ANFIS. This set of data is generated from the model for cylindrical plunge grinding process that was presented in chapter 3.

- The ANFIS is generated by use of grid partitioning, which is a method for grouping data into clusters based on their similarity. The ANFIS is then trained by use of hybrid learning rule. The hybrid learning rule combines the gradient method and the least squares estimate (LSE).

- The ANFIS is then tested against a set of testing data which is also generated from the model presented in chapter 3.

- Different sets of data are presented to the ANFIS, and based on the input-output relationship of the ANFIS, the membership functions for the FLC are constructed.

- The rule base for the FLC is generated based on the execution of the ANFIS. This is because, ANFIS automatically generates its own rule base depending on its set of training data.

The ANFIS that is used in the tuning of fuzzy membership functions is explained using Figures 6.2 through 6.6. The proposed ANFIS uses Sugeno inference mechanism.

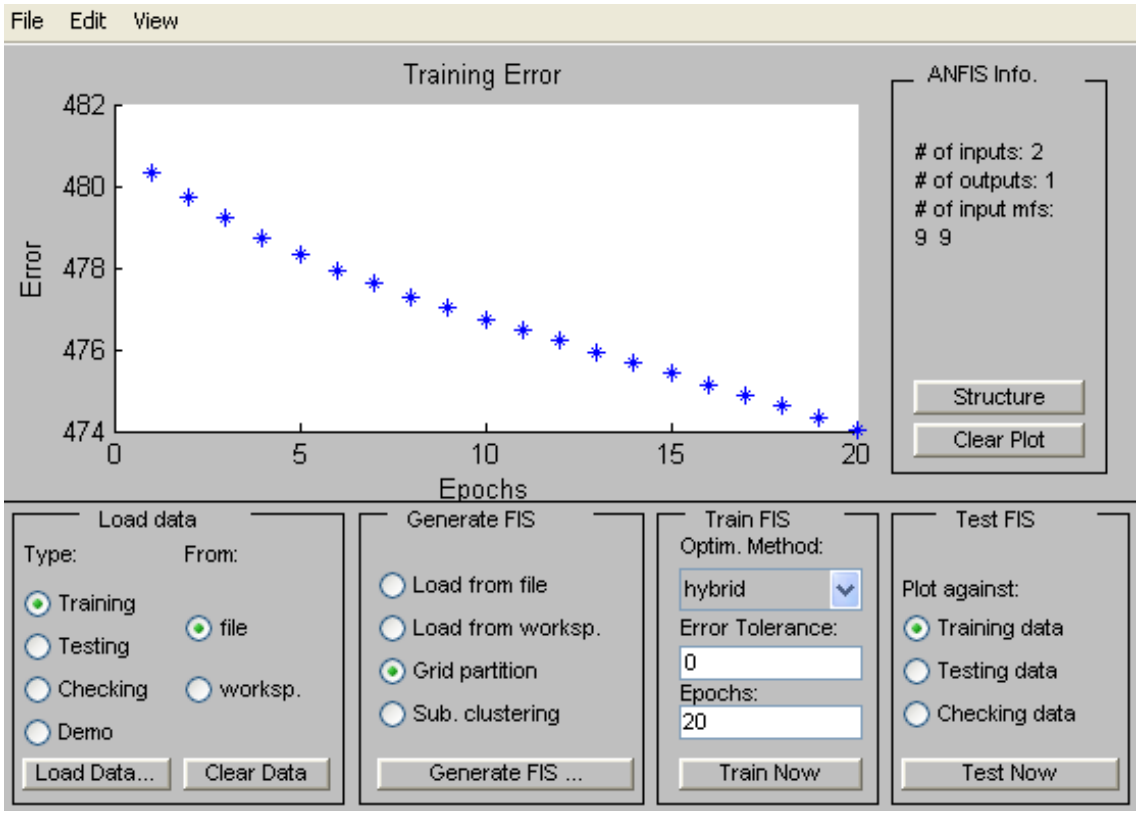

Figure 6.2: A screen shot of the ANFIS editor for the cylindrical plunge grinding process

The main reason for the use of Sugeno inference mechanism is the ability of the inference mechanism to model non-linear problems. In this type of inference mechanism, the output is a function of the inputs and is a fuzzy singleton. Figure 6.2 is a screen shot of the ANFIS editor. It shows a plot of the training error after the training process. As is shown in the Figure, the ANFIS is generated with grid partitioning fuzzy inference mechanism, where each input is assigned nine membership functions, and then trained with 20 epochs (number of iterations for training) using hybrid learning rule. Figure 6.3 shows the block representation of the ANFIS which uses Sugeno inference system. In this Figure N-deflection and T-deflection are the instan-

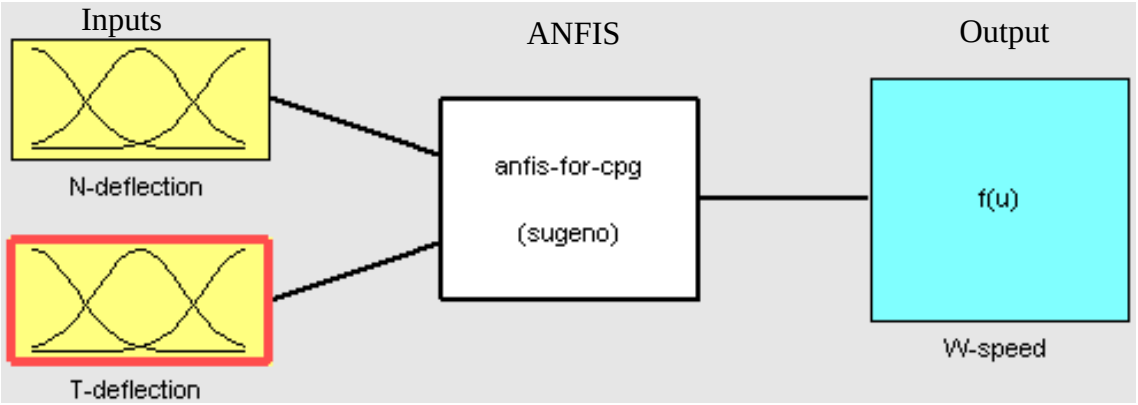

Figure 6.3: Block representation of the ANFIS

taneous normal and tangential deflection at the point of measurement, respectively, and W-speed is the optimum grinding wheel speed. Figure 6.4 shows the structure of

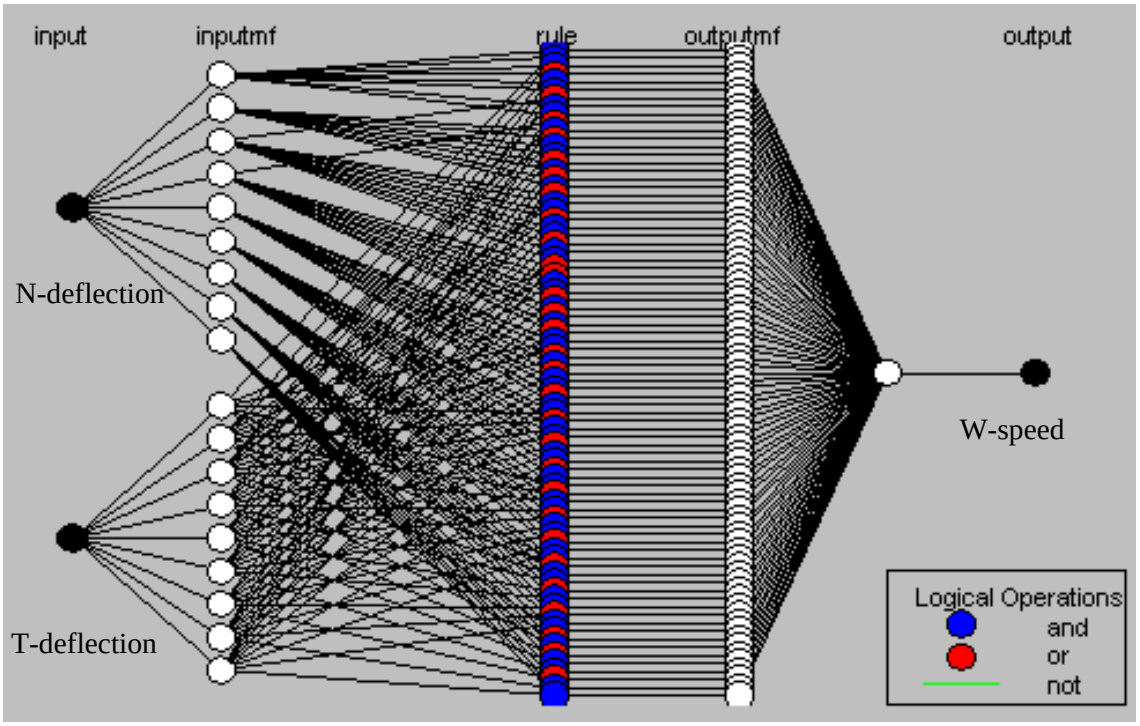

Figure 6.4: Structure of the ANFIS

the ANFIS and the parameters used in its execution process. In this figure, 'input' represents the inputs which are T-deflection and N-deflection and 'inputmf' represents the input membership functions. Also in this figure, 'rule' represents the rules, 'outputmf' represents the output membership functions and 'output' the output.

Figure 6.5 represents Gaussian type membership functions for the two inputs, namely, N-deflection and T-deflection. This type of membership function is used because it represents the nonlinear nature of the problem in a better way than triangular or trapezoidal membership functions. In this figure, the membership functions are as indicated in Table 6.1.

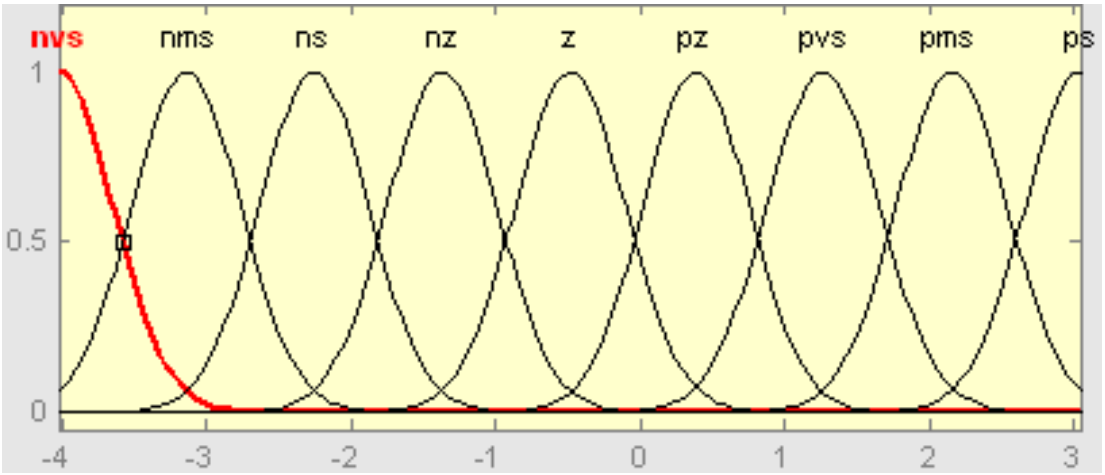

Figure 6.5: Membership functions of the inputs

Table 6.1: Definition of membership functions

Membership function	**Definition**
nvs	negative very small
nms	negative medium small
ns	negative small
nz	negative zero
z	zero
pz	positive zero
pvs	positive very small
pms	positive medium small
ps	positive small

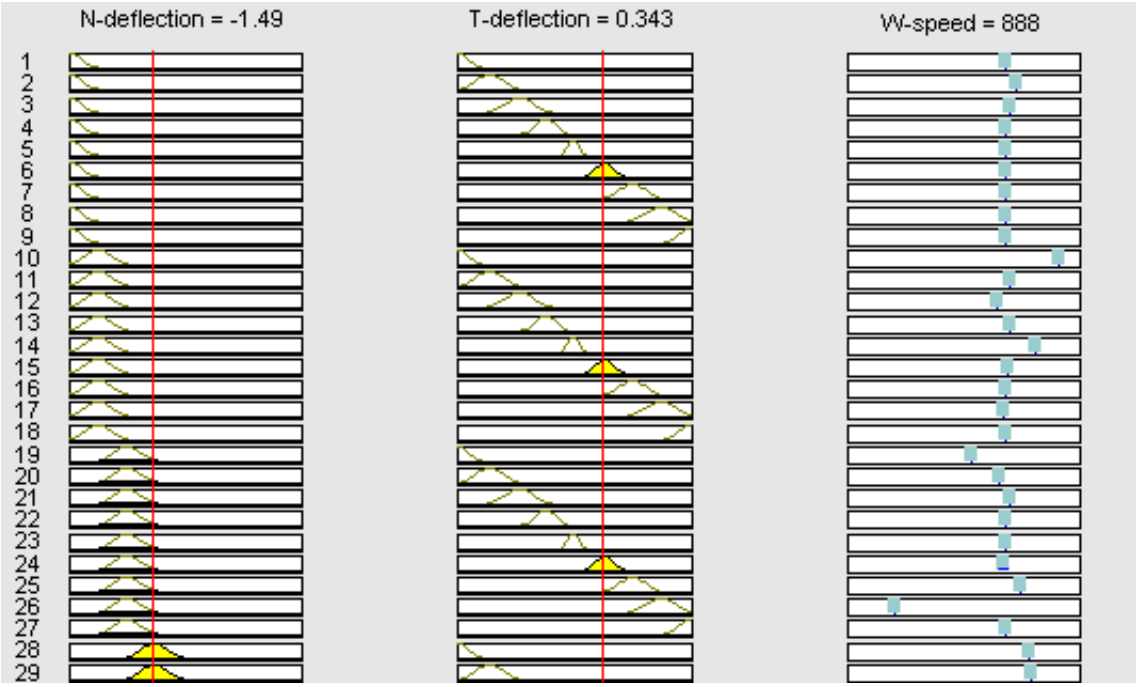

Figure 6.6: Part of the rule base generated by the ANFIS

Figure 6.6 shows a screen shot of diagrammatic representation of some of the rules for the ANFIS. It shows the crisp output (wheel speed) of 888 rpm with inputs as normal deflection of -1.49 μm and tangential deflection of 0.343 μm. There are 81 (9^2) rules in total. If one or the two of the input values are changed, then, the output changes as per the rules to give the optimum grinding wheel speed. The ANFIS was presented with different input sets so as to simulate a machining situation. The results were used in the design of the input and output membership functions as well as in the generation of the rules for the Fuzzy Logic Controller.

6.2.3 Implementation of the fuzzy logic controller

Figure 6.7 shows the block diagram for the proposed controller which was implemented in LabVIEW® software. The experimental setup that has the controller connected is shown in Figure 6.8. The output from the controller was a voltage that varied from 0 V to 10 V. The voltage was matched to motor speeds between 0 and 1430 rpm, that is, 0 V for 0 rpm (the lowest speed) and 10 V for 1430 rpm (highest possible speed). There was a linear relationship between the wheel speed and the control voltage as shown in Figure 6.9. The rule base for the FLC used *OR* and *AND* conjunctions and the consequents were singletons.

The output from the controller was connected to a variable frequency drive (VFD) which was used to control the grinding wheel speed. This variable speed drive had a control terminal whose input voltages were 0 V to 10 V. This enabled the control of the motor speed. The VFD was connected to a three phase input power, and, gave a three phase output power to the motor. A photo of the machine setup with controller

in place is shown in Figure 6.10.

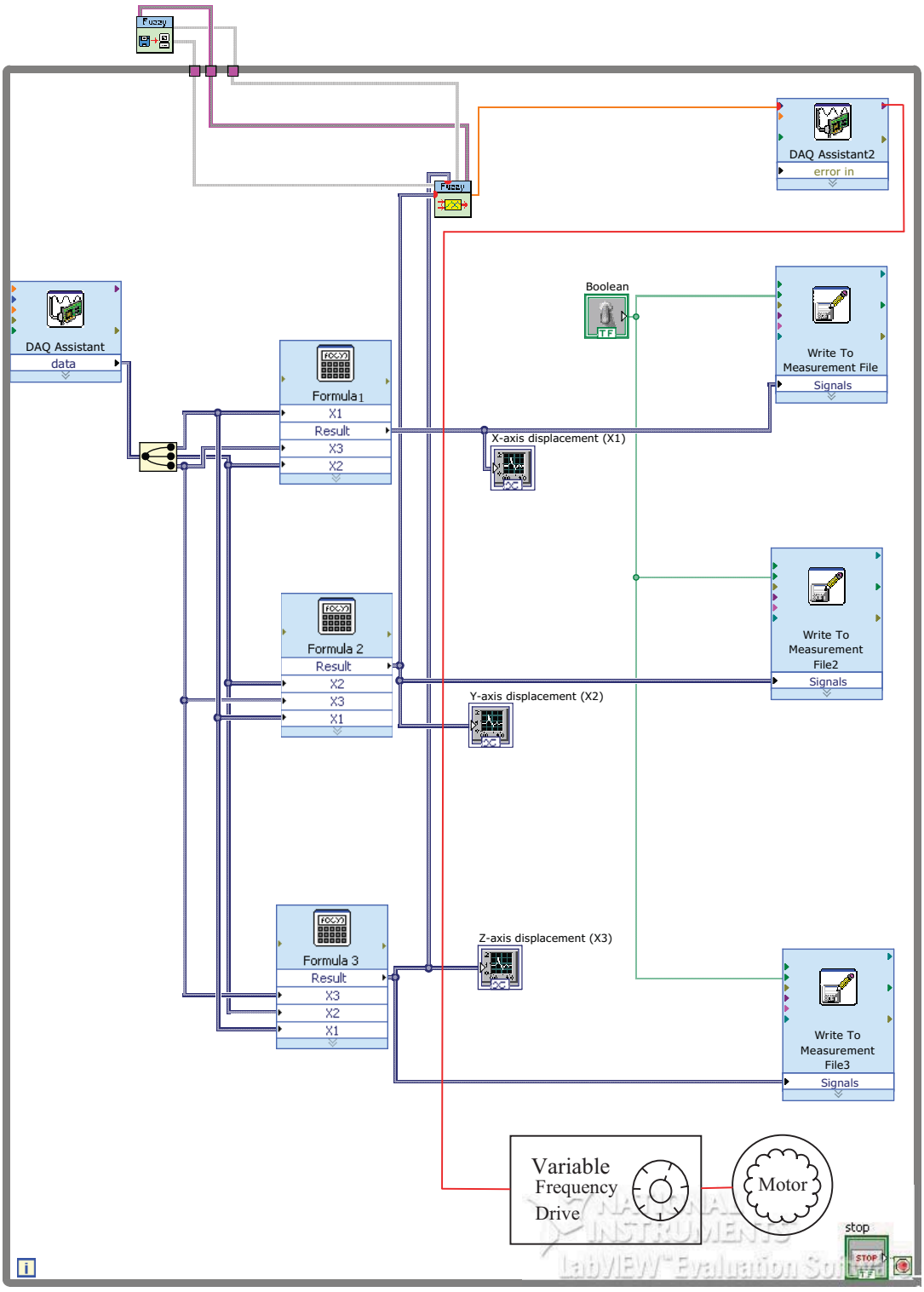

Figure 6.7: Controller block

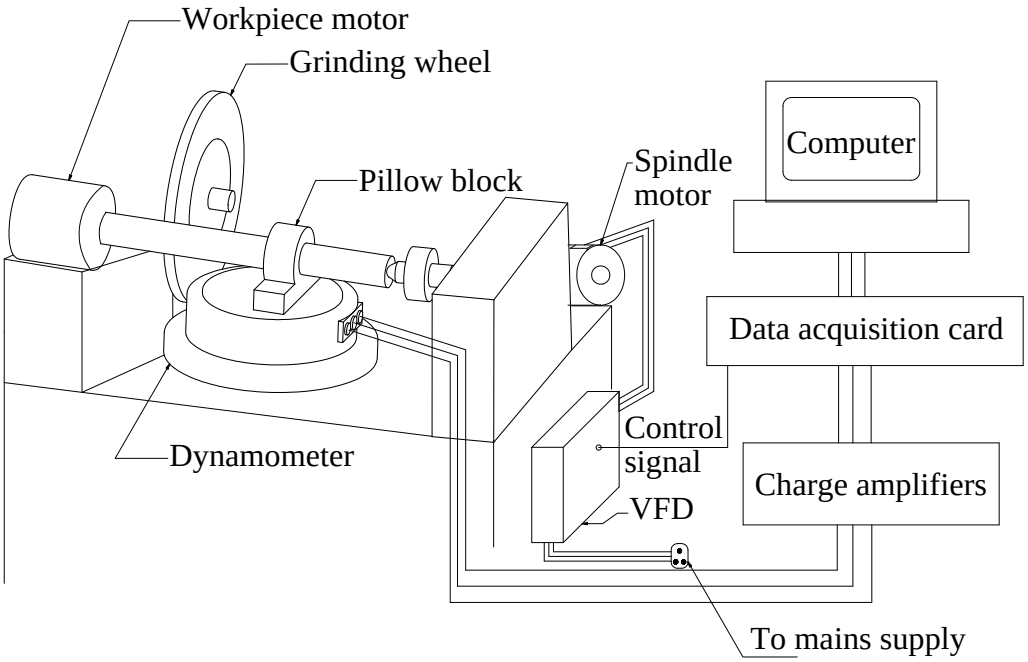

Figure 6.8: Experimental setup of machine with controller

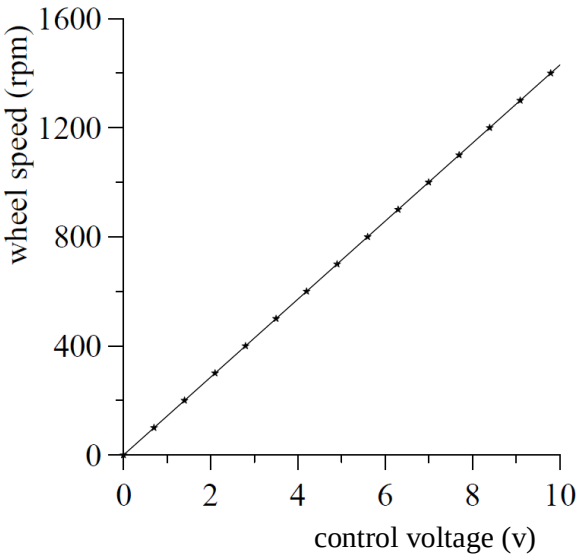

Figure 6.9: Controller calibration curve

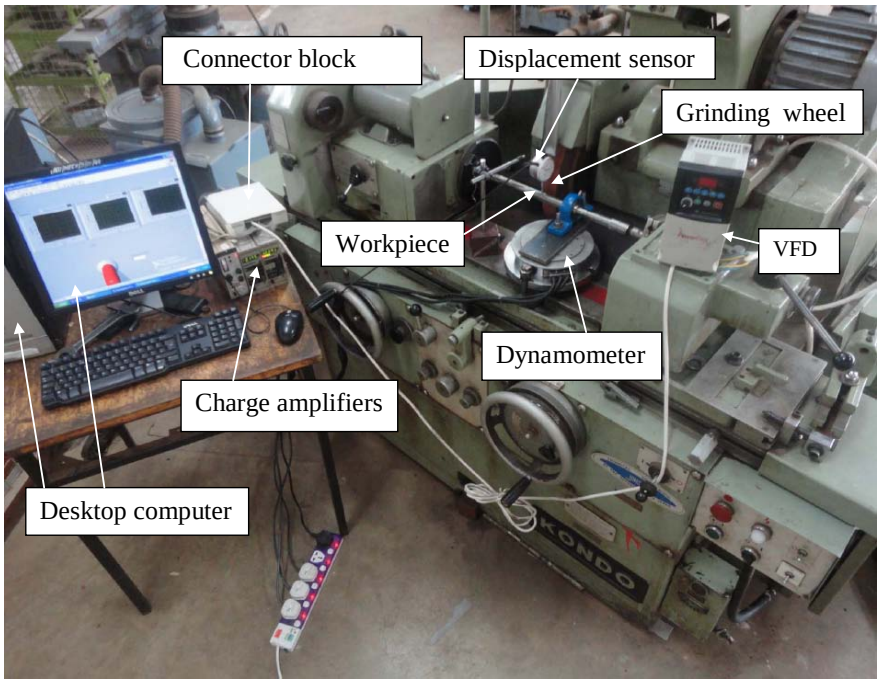

Figure 6.10: Setup of the machine and controller

6.2.4 Results and discussion

To test the effectiveness of the controller, measurements of vibrations are taken at different workpiece speeds and infeeds. These vibrations are then compared with the vibrations that result, when grinding without controller. This is done for two materials, namely, mild steel and EN9 steel.

6.2.4.1 Effect of variation of workpiece speed on vibration

To test the effect of workpiece speed on vibrations, the workpiece speed is varied and measurements of the vibrations taken at an infeed of 0.05 mm. Figures 6.11 - 6.19 show the waveforms and power spectra of vibrations in grinding mild steel, with and without the ANFIS based fuzzy logic controller. The power spectra for both the

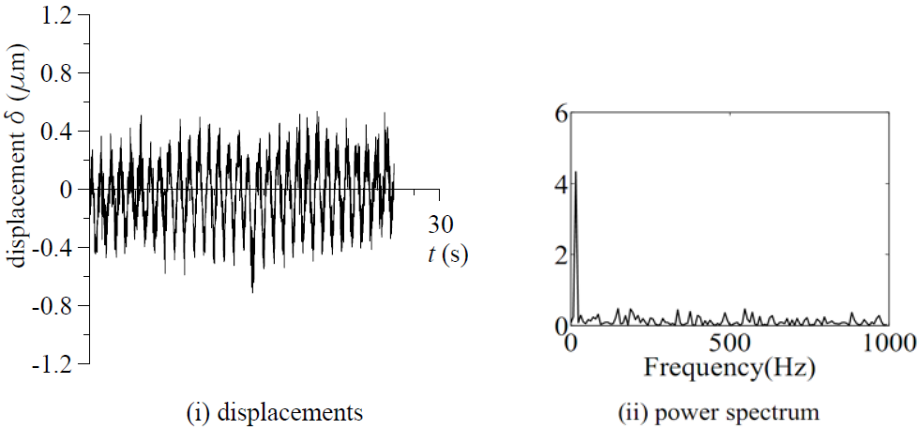

(a) without controller: the RMS value is 0.2199

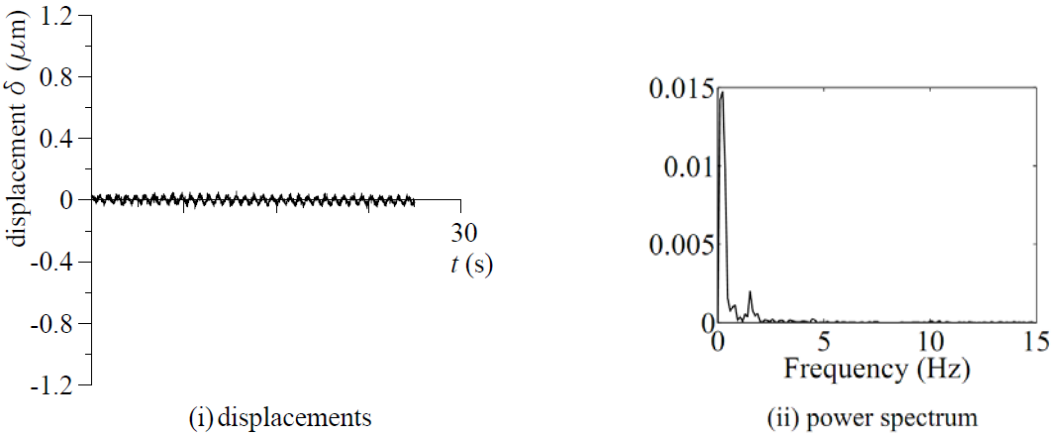

(b) with FLC controller: the RMS value is 0.0183

Figure 6.11: Vibrations in grinding mild steel (workpiece speed, 295 rpm)

controlled and uncontrolled cases show presence of multiple modes of vibration. The variation of the vibration amplitudes with either the workpiece speed, the grinding wheel speed or the infeed when grinding without the controller as can be seen varies in an unpredictable manner.

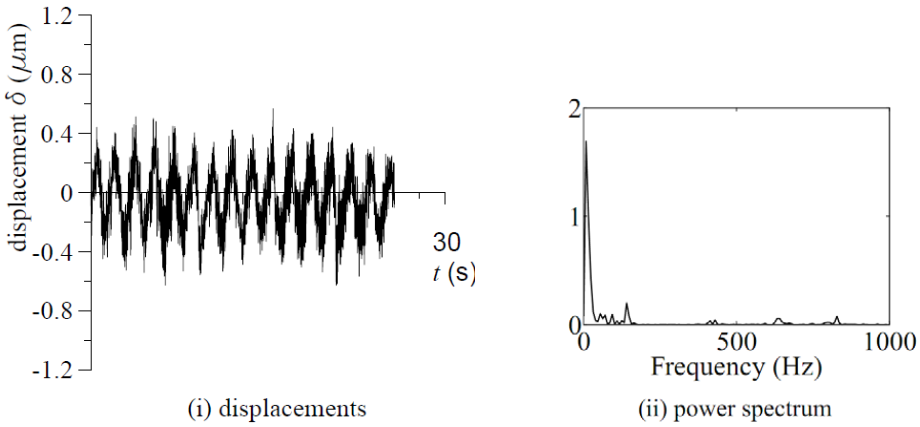

(a) without controller: the RMS value is 0.2121

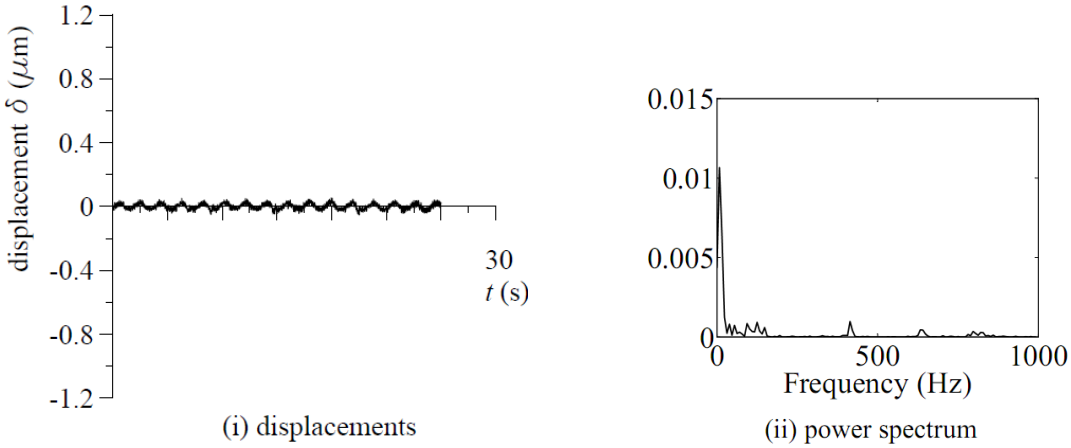

(b) with FLC controller: the RMS value is 0.0184

Figure 6.12: Vibrations in grinding mild steel (workpiece speed, 215 rpm)

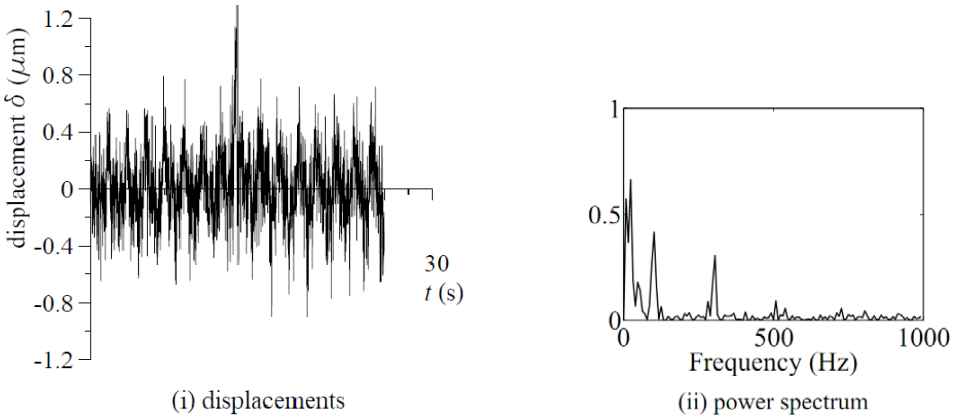

(a) without controller: the RMS value is 0.2462

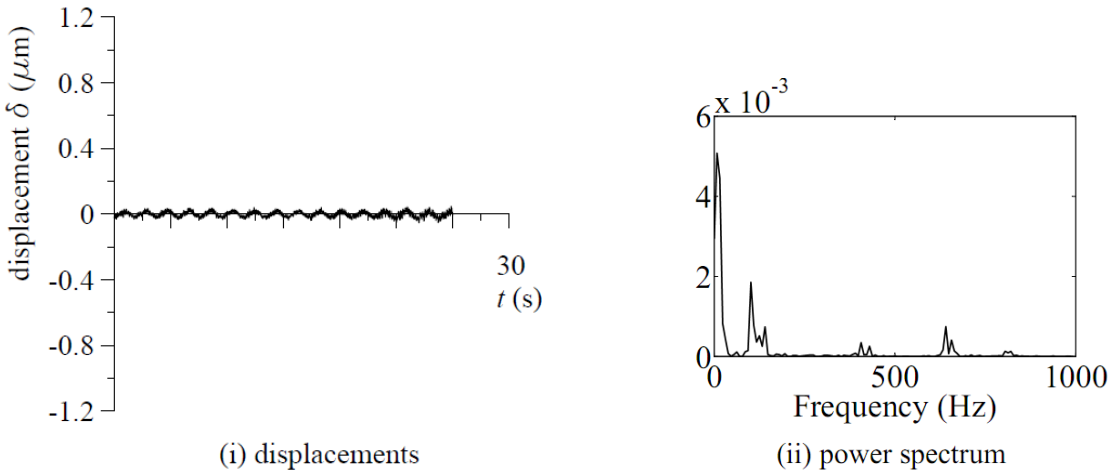

(b) with FLC controller: the RMS value is 0.0159

Figure 6.13: Vibrations in grinding mild steel (workpiece speed, 130 rpm)

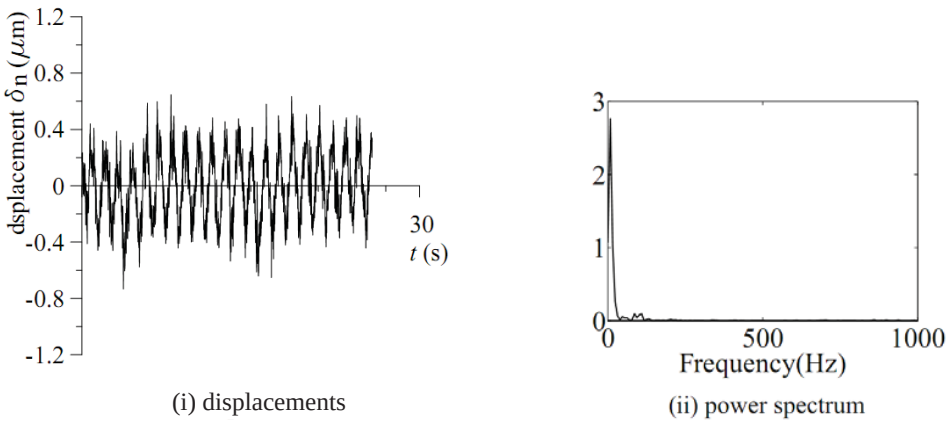

(i) displacements (ii) power spectrum

(a) without controller: the RMS value is 0.2344

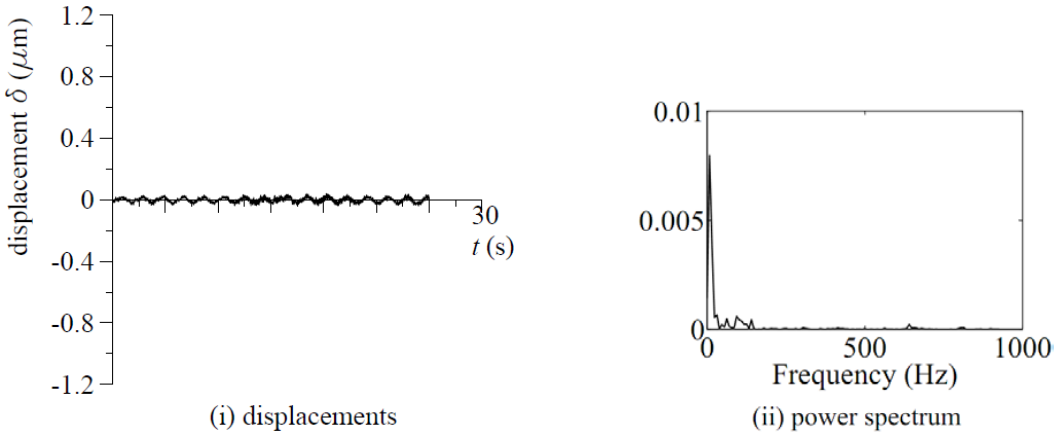

(i) displacements (ii) power spectrum

(b) with FLC controller: the RMS value is 0.0154

Figure 6.14: Vibrations in grinding mild steel (workpiece speed, 55 rpm)

These figures show that, the vibration amplitudes in grinding mild steel for the FLC controlled cases are in the order of 10^{-5} mm, and those ones for non-controlled cases are in the order of 10^{-4} mm. This shows a great reduction in the vibration amplitudes by the FLC.

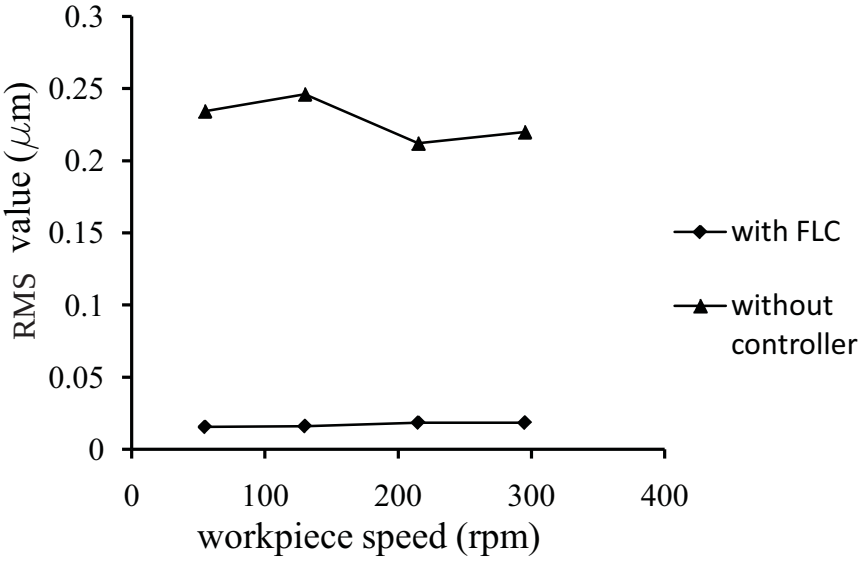

Figure 6.15: Variation of RMS values of displacement with workpiece speed in grinding mild steel

Figure 6.15 shows the relationship between the workpiece speed and the RMS values when grinding mild steel. It can be seen in this figure that when grinding without a controller, the RMS values of the vibrations vary between 0.2 μm and 0.25 μm for the cases considered. However, when grinding under the control of the FLC, the RMS values are much lower and vary within a narrow range of 0.015 μm and 0.018 μm. This shows that the controller is able to maintain low vibration amplitudes regardless of the value of the workpiece speed. This is a very desirable characteristic of the ANFIS based FLC.

Tests similar to those in grinding mild steel were done for EN9 steel. The results shown in Figures 6.16 - 6.20 present the comparison of the waveforms and power spectra for two cases; with and without controller.

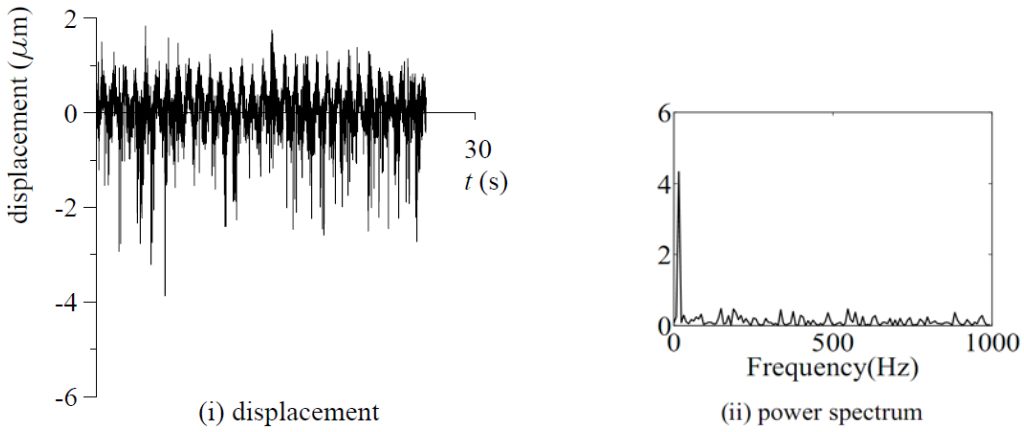

(a) without controller: the RMS value is 0.4704

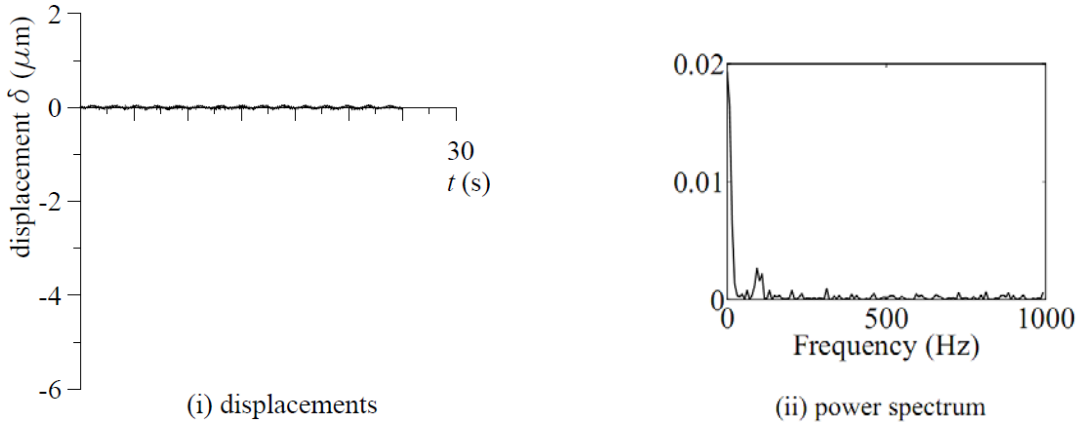

(b) with FLC controller: the RMS value is 0.0821

Figure 6.16: Vibrations in grinding EN9 steel (workpiece speed, 295 rpm)

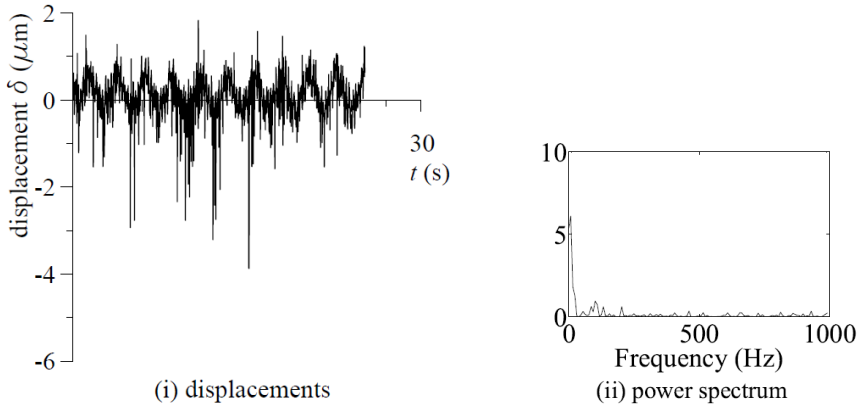

(a) without controller: the RMS value is 0.4661

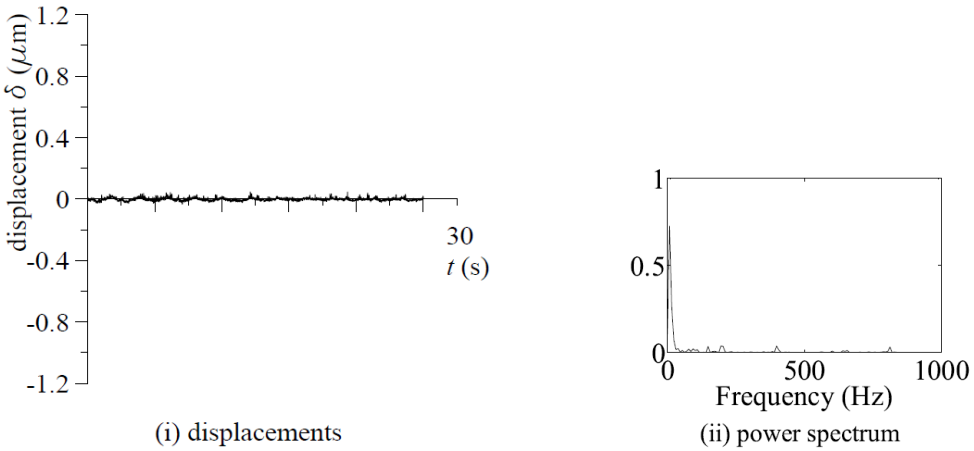

(b) with FLC controller: the RMS value is 0.0947

Figure 6.17: Vibrations in grinding EN9 steel (workpiece speed, 215 rpm)

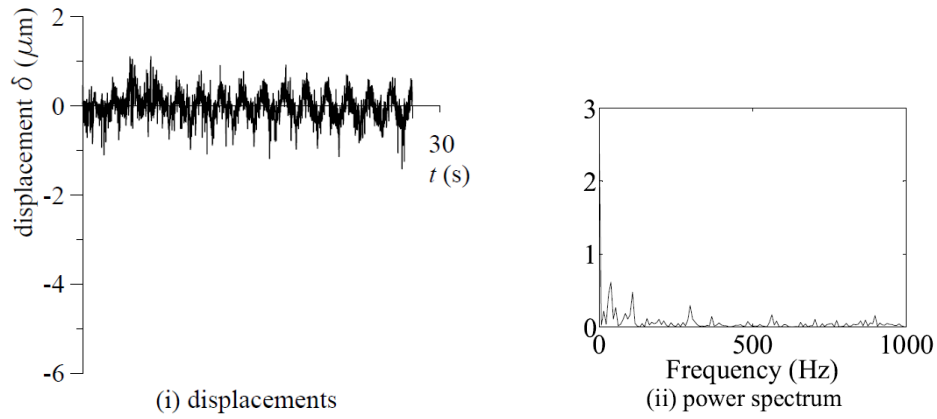

(a) without controller: the RMS value is 0.3042

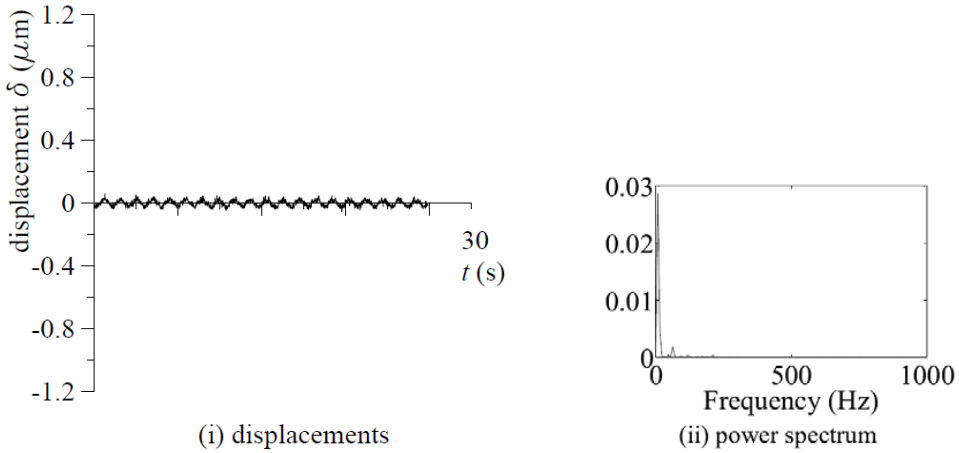

(b) with FLC controller: the RMS value is 0.0180

Figure 6.18: Vibrations in grinding EN9 steel (workpiece speed, 130 rpm)

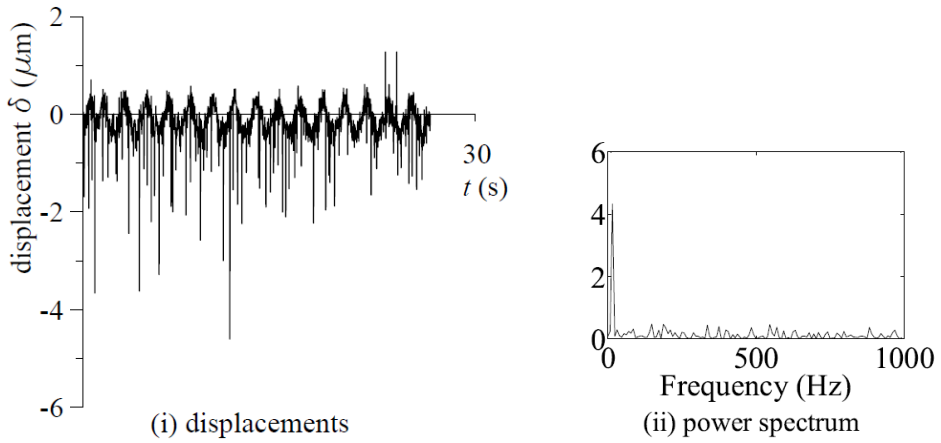

(a) without controller: the RMS value is 0.3667

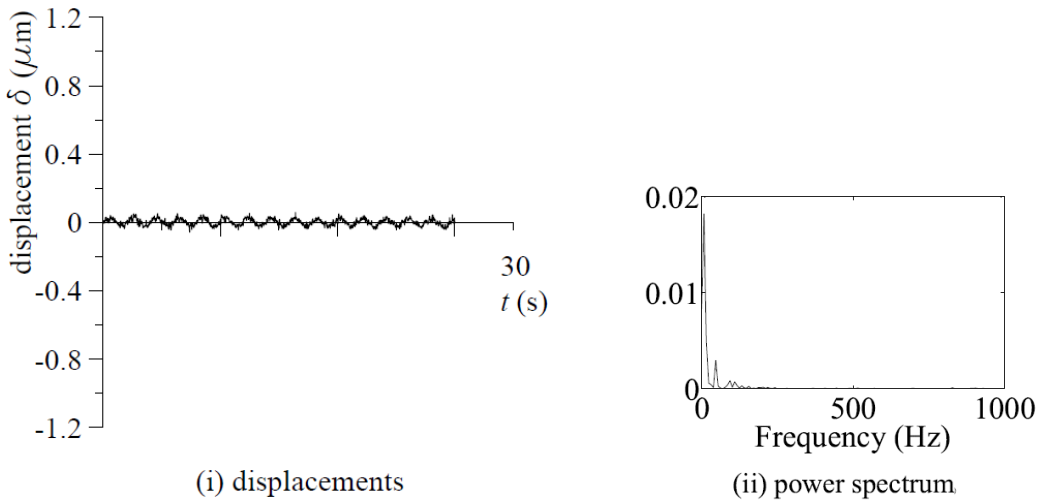

(b) with FLC controller: the RMS value is 0.0191

Figure 6.19: Vibrations in grinding EN9 steel (workpiece speed, 55 rpm)

From these figures, it is seen that, the vibration amplitudes in grinding under the control of FLC are in the order of 10^{-5} mm. However, the vibration amplitudes in griding without controller are in the order of 10^{-3} mm. The relationship between the RMS values of deflections and the workpiece speed in grinding EN9 steel is

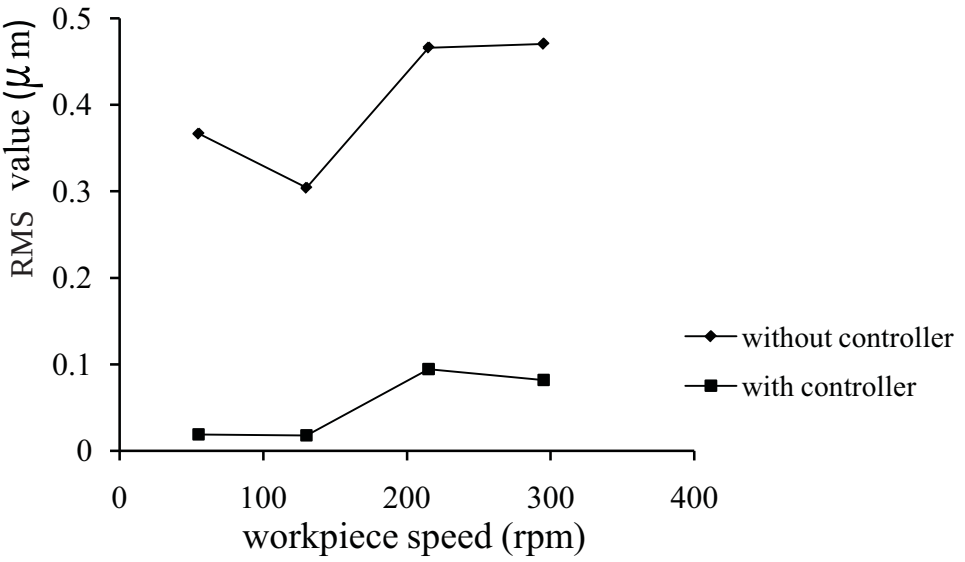

Figure 6.20: Variation of RMS values of displacement with workpiece speed in grinding EN9 steel

shown in Figure 6.20. In this figure, it can be seen that, the RMS values vary non-linearly with increase in workpiece speed. This is due to the complex nature of the relationship between the input and the output parameters, causing unpredictable process variation [18].

6.2.4.2 Effect of variation of infeed on vibrations

In order to test the effect of infeed on vibrations in grinding mild steel and EN9 steel, grinding process was carried out with workpiece speed at 295 rpm.

Figures 6.21 - 6.24 show the vibration waveforms and power spectra in grinding mild steel with different infeed.

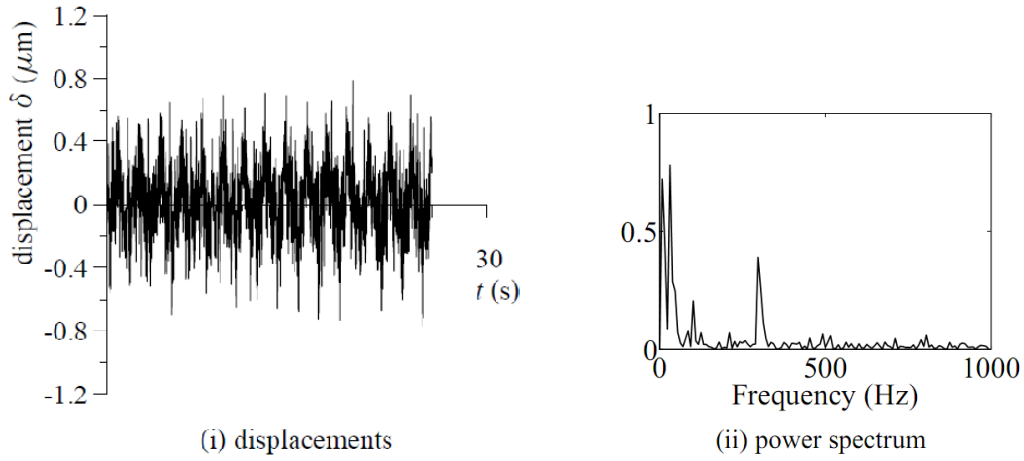

(a) without controller: the RMS value is 0.2250

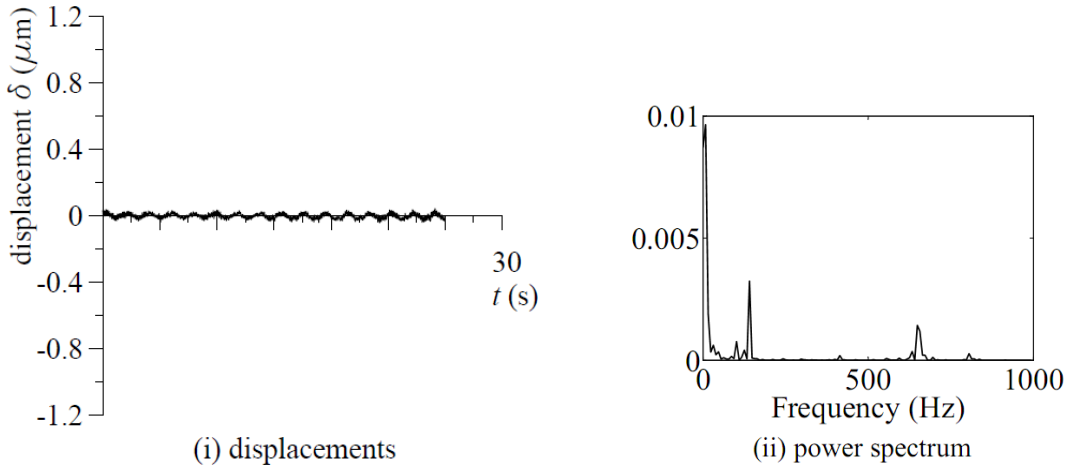

(b) FLC controlled: the RMS value is 0.0138

Figure 6.21: Vibrations in grinding mild steel (infeed, 0.07 mm)

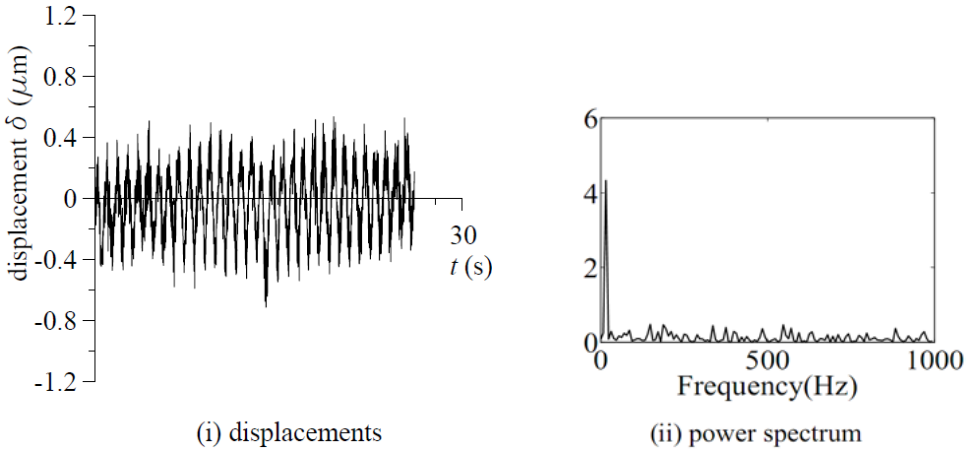

(a) without controller: the RMS value is 0.2199

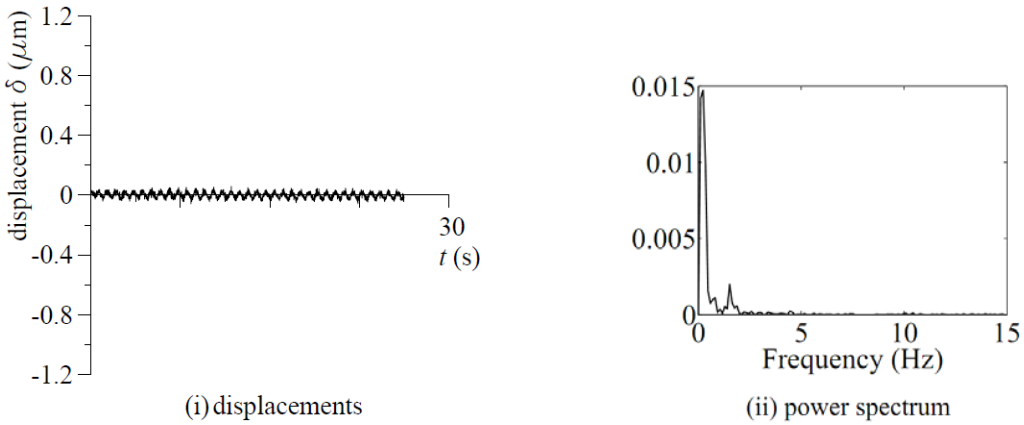

(b) FLC controlled: the RMS value is 0.0185

Figure 6.22: Vibrations in grinding mild steel (infeed, 0.05 mm)

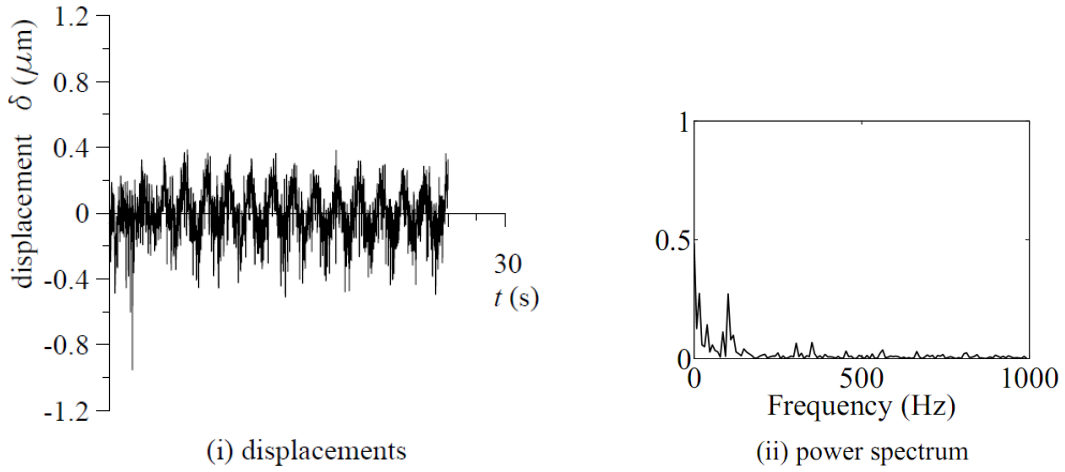

(a) without controller: the RMS value is 0.1398

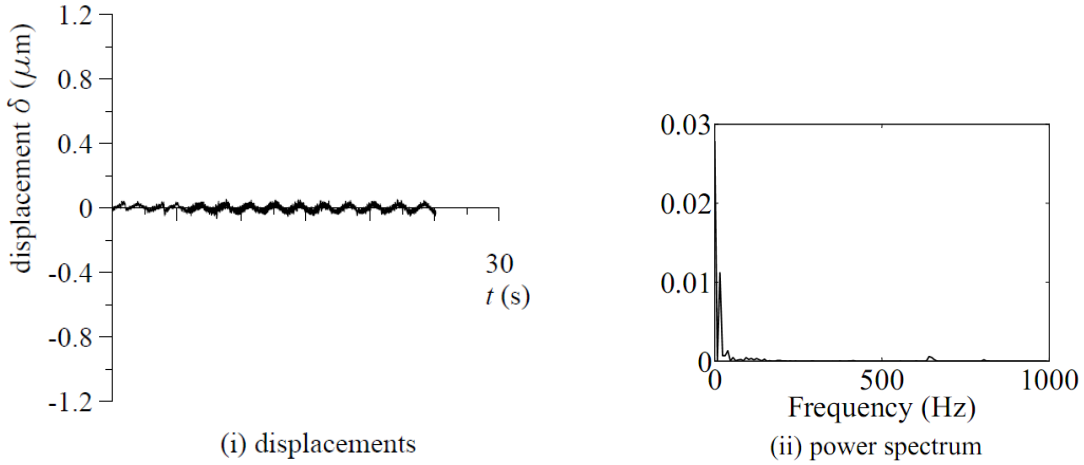

(b) FLC controlled: the RMS value is 0.0193

Figure 6.23: Vibrations in grinding mild steel (infeed, 0.03 mm)

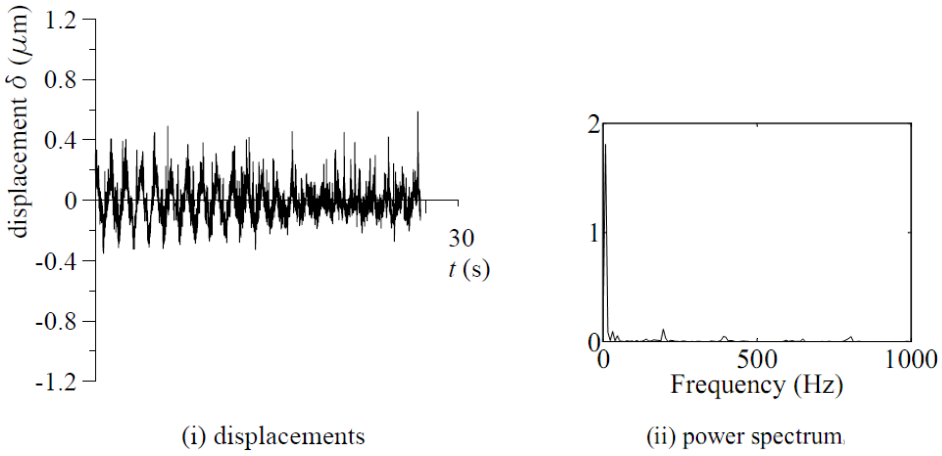

(a) without controller: the RMS value is 0.1132

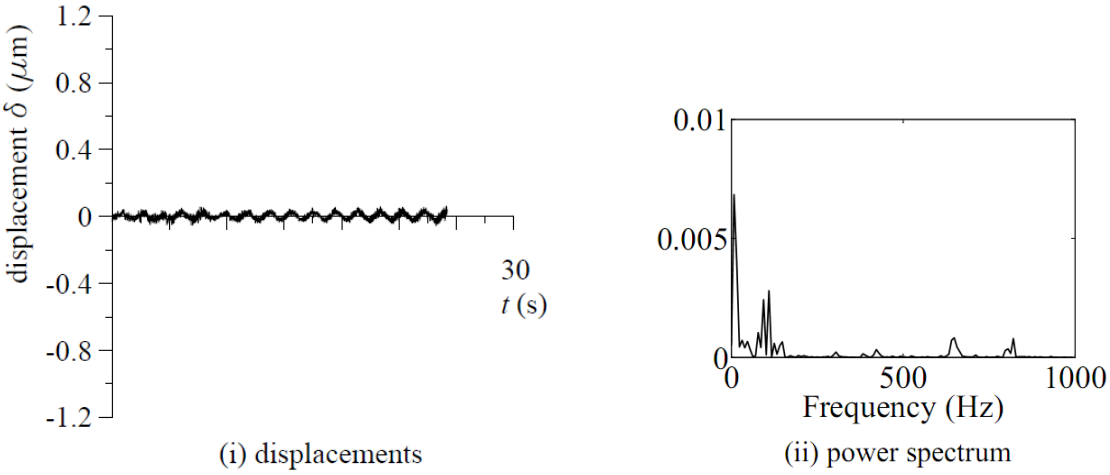

(b) FLC controlled: the RMS value is 0.0194

Figure 6.24: Vibrations in grinding mild steel (infeed, 0.01 mm)

From these figures, it can be seen that the amplitudes of vibration in the controlled grinding process are much lower than in the uncontrolled grinding process. The power spectra shows presence of multiple modes of vibration.

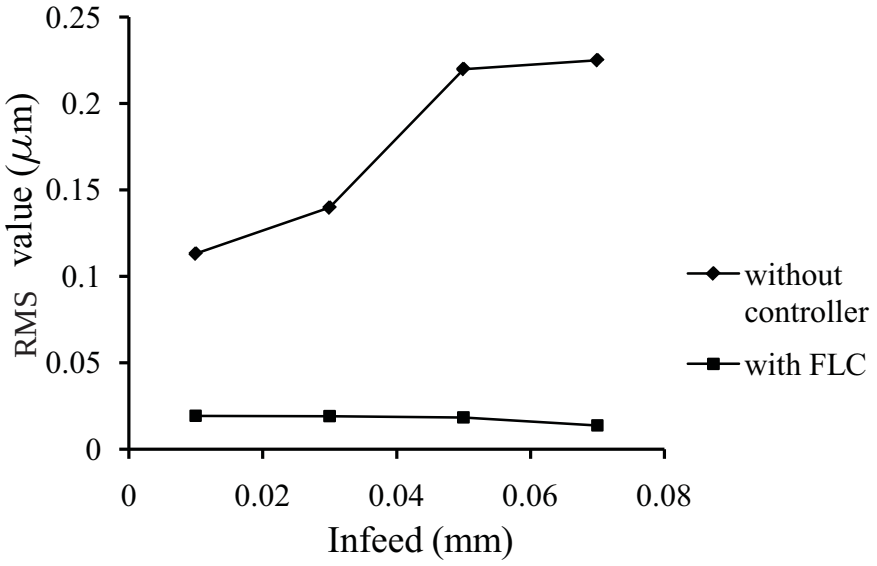

Figure 6.25: Variation of RMS values with infeed in grinding mild steel

Figure 6.25 shows the variation of the RMS values with infeed for two cases; when grinding without controller, and when grinding with the ANFIS based FLC. From this figure, it can be seen that, when grinding under the control of the ANFIS based FLC, the RMS values of the vibration are low and remain within a narrow range in all cases, as compared to the case when grinding without controller.

Tests similar to those for grinding mild steel were done for EN9 and the waveforms of vibration and power spectra are shown in Figures 6.26 - 6.29.

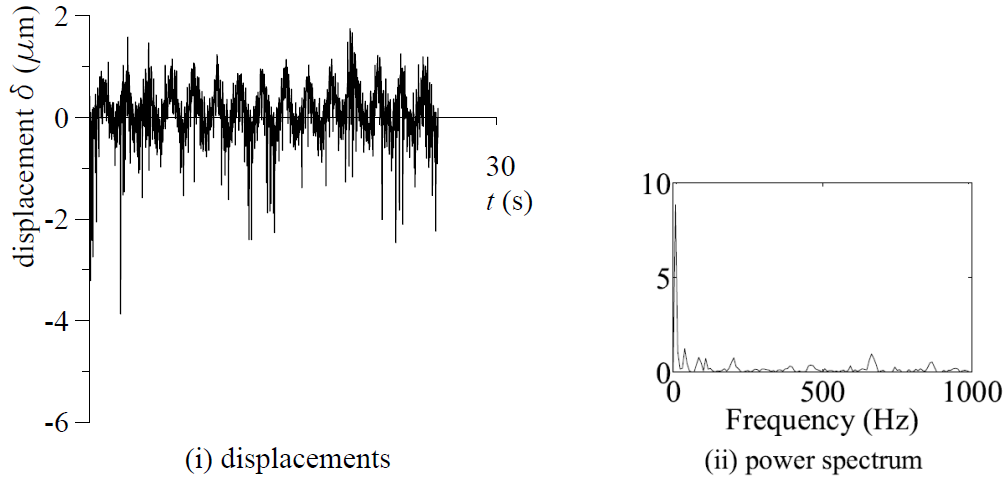

(a) without controller: the RMS value is 0.4791

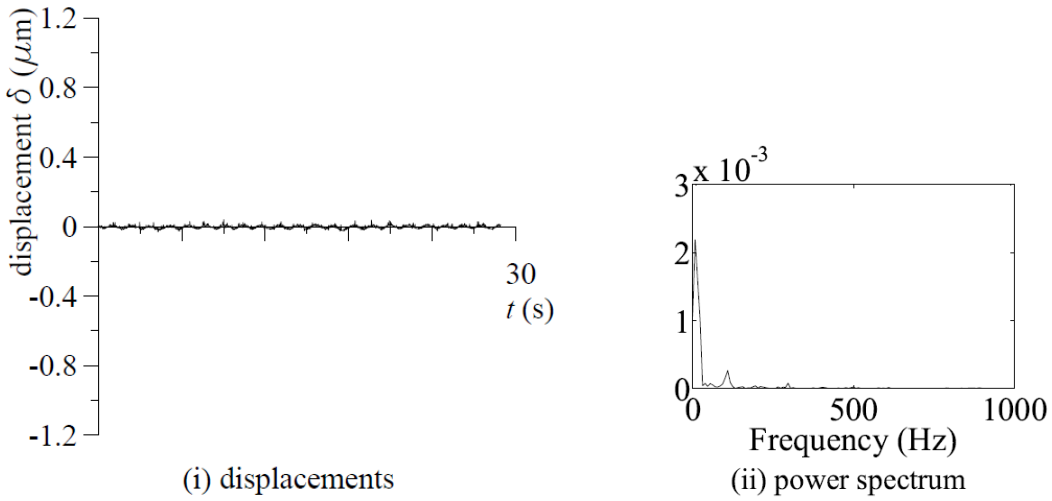

(b) FLC controlled: the RMS value is 0.0082

Figure 6.26: Vibrations in grinding EN9 steel (infeed, 0.07 mm)

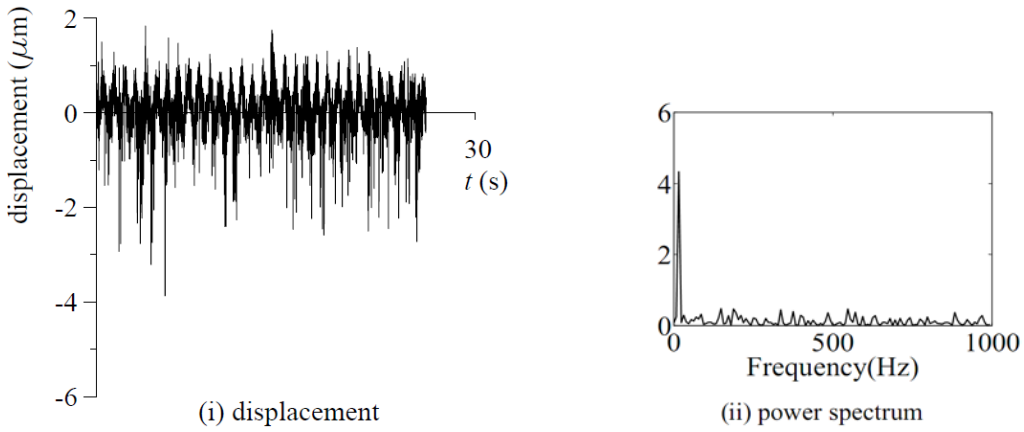

(a) without controller: the RMS value is 0.4704

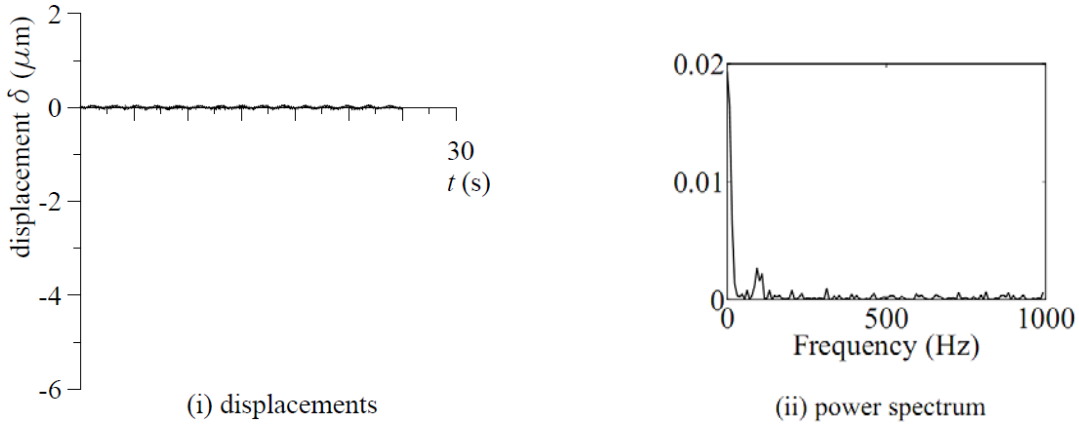

(b) FLC controlled: the RMS value is 0.0821

Figure 6.27: Vibrations in grinding EN9 steel (infeed, 0.05 mm)

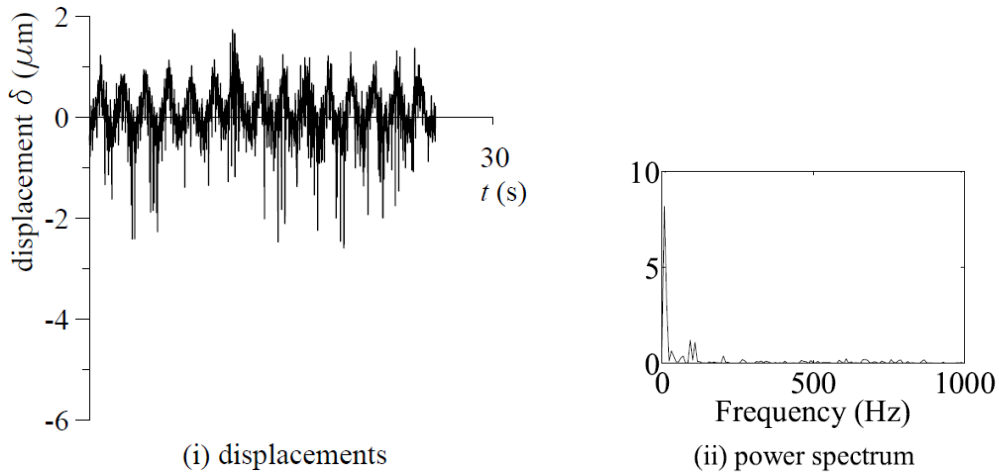

(a) without controller: the RMS value is 0.4781

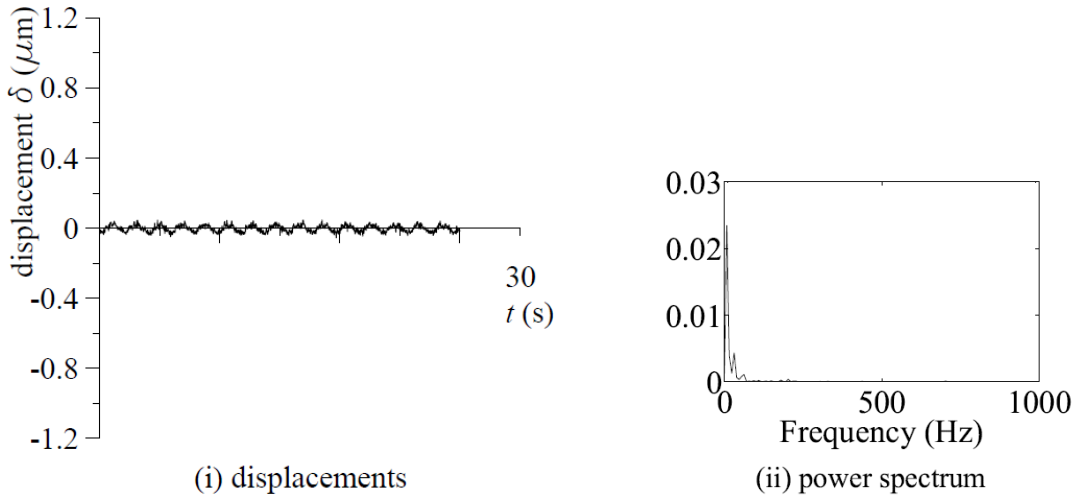

(b) FLC controlled: the RMS value is 0.0179

Figure 6.28: Vibrations in grinding EN9 steel (infeed, 0.03 mm)

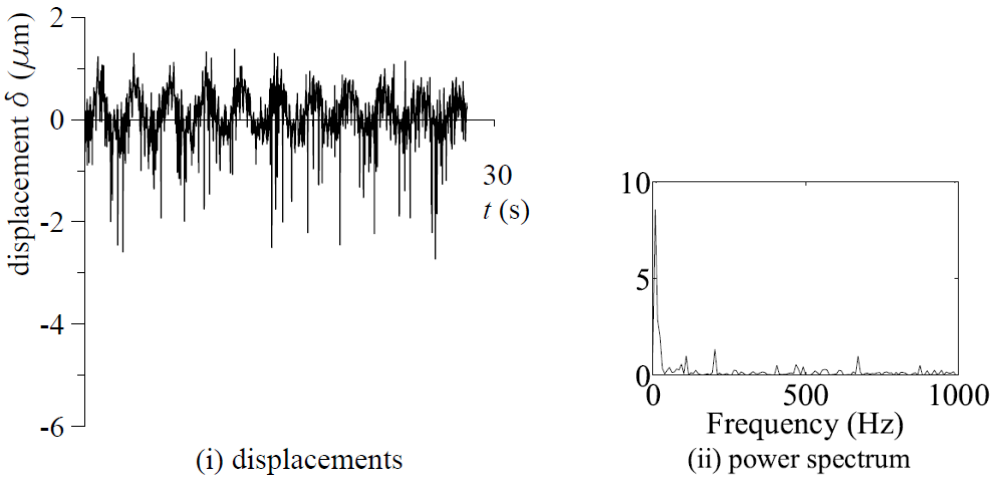

(a) without controller: the RMS value is 0.4626

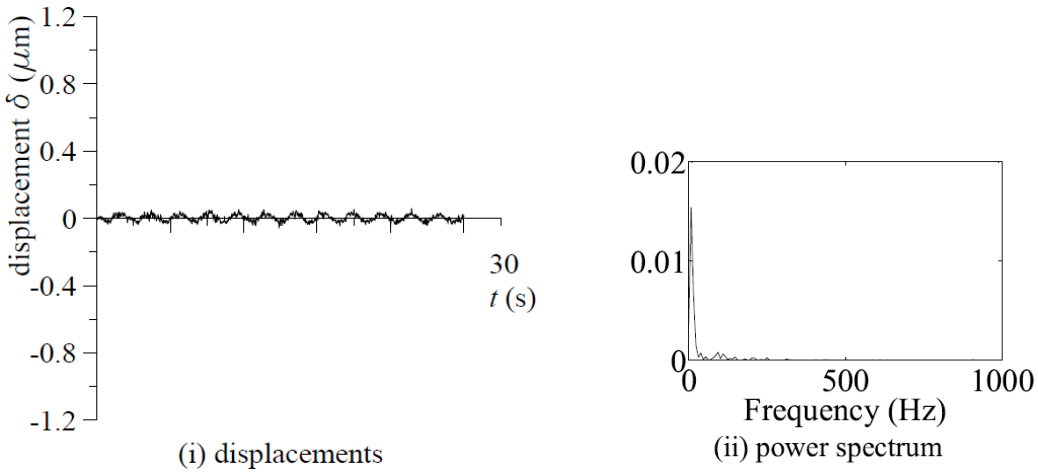

(b) FLC controlled: the RMS value is 0.0189

Figure 6.29: Vibrations in grinding EN9 steel (infeed, 0.01 mm)

As in the case of grinding mild steel, it can be seen that the amplitudes of vibration in the controlled grinding process are much lower than in the uncontrolled grinding process, and the power spectra show presence of multiple modes of vibration.

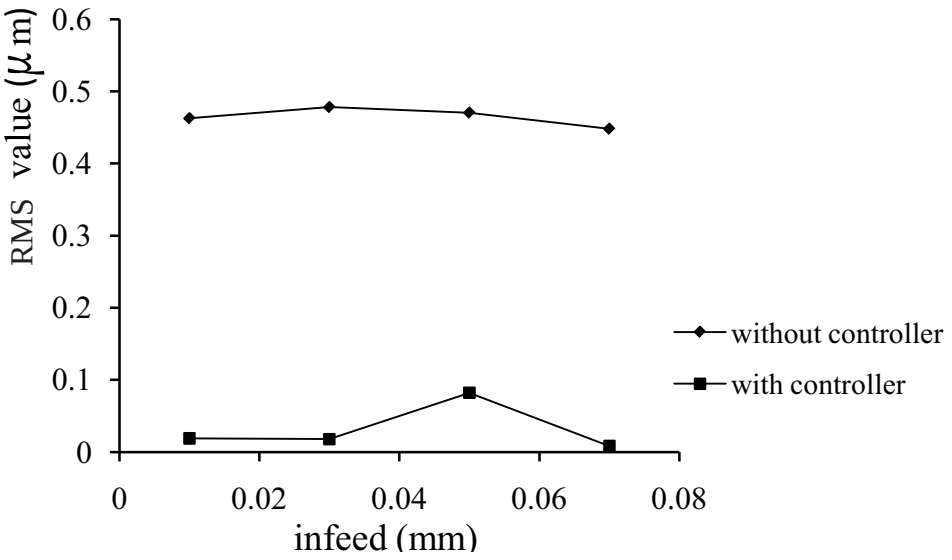

Figure 6.30: Variation of RMS values with infeed in grinding EN9 steel

Figure 6.30 shows the variation of amplitudes of vibration in grinding EN9 steel with infeed for FLC controlled and uncontrolled grinding processes. A non-linear relationship exists between the vibration amplitudes and infeed. It can be noted that the vibration amplitudes are in the order of 10^{-5} mm for the controlled process while those of the uncontrolled process are in the order of 10^{-3} mm. Further tuning and increase of membership functions could help increase the sensitivity of the controller hence eliminating the increase in displacement at the infeed of 0.05 mm.

6.3 Summary

Comparing the waveforms of the vibrations for both non-controlled grinding, and the Fuzzy Logic Controlled grinding processes, it can be observed that;

- the amplitudes of the vibrations when grinding without controller are in the

order of 10^{-3}mm for EN9 steel and 10^{-4} mm, for mild steel. When grinding with ANFIS based FLC the amplitudes of vibration are in the order of 10^{-5} mm. This shows a great reduction in the vibration amplitudes.

- when grinding under the control of the FLC, the vibration amplitudes remain in the 10^{-5} mm range regardless of any changes in the infeed, wheel or workpiece speeds.

Thus, the proposed ANFIS based fuzzy logic controller has been seen to reduce the vibration in the grinding process by adaptively adjusting the grinding wheel speed. This reduction in vibration would lead to less noise while machining, less need for operator intervention, better quality of surface finish for the ground parts, reduction in production cost and longer tool and machine life.

The ANFIS based controller, once designed can be used on any cylindrical grinding machine without the need for retraining the ANFIS. It can be incorporated at the design stage of the machine. Once the controller is designed, it can be implemented on multiple machines.

CHAPTER 7

6 CONCLUSION AND RECOMMENDATIONS

7.1 Conclusion

In this study, a model to predict grinding process vibrations for the cylindrical plunge grinding process was developed. This model was validated through experimental work. The effects of variation of workpiece and grinding wheel speeds, as well as infeed on the grinding process vibrations were investigated. The model that was developed simulated the workpiece displacements for a given set of grinding parameters. Data generated from simulation of the model was used to train the ANFIS, which was implemented by use of a fuzzy logic controller. The proposed ANFIS based fuzzy logic controller was implemented in LabVIEW® environment. It can be concluded that;

- the proposed ANFIS based controller was able to effectively reduce the vibration in cylindrical grinding.
- the model predictions were more accurate at lower grinding wheel and workpiece speeds.
- the amplitudes of vibration in grinding increase with increase in infeed and decrease with decrease of infeed.
- the amplitudes of vibration vary non-linearly with change in workpiece speed, grinding wheel speed and workpiece material.

- when grinding EN9 and mild steels with the same grinding parameters, it was found that, the amplitudes of vibration in grinding EN9 steel were higher than those in grinding mild steel.

7.2 Recommendations

It was demonstrated that, the developed controller can effectively reduce the vibrations in cylindrical grinding. This work could be extended to other machining processes that are susceptible to chatter vibration.

Further research could be carried out to investigate the effect of controlling the speed of the workpiece on the vibrations. Also, Analysis of the effect of chatter on the grinding wheel and workpiece properties can be done. Research could also be carried out on the development of a fuzzy logic controller that has a higher number of membership functions, although this compromises the training speed of the ANFIS.

REFERENCES

[1] Hodge E. J., Thomas R. K., "Adaptive pole-zero cancellation in grinding force control," *IEEE Transactions on control systems technology*, vol. Vol. 7, No.3, pp. 363–370, 1999.

[2] Jian M., "Application of design of experiments on an engineering problem." Department of Statistics, University of Connecticut, Storrs, 2005.

[3] Glen D., "Mechanical material removal ." Lecture notes, 2003.

[4] Janez G. , Andreas B., Edvard G., Fritz K., Igor G., "Automatic chatter detection in grinding," *International Journal of Machine Tools & Manufacture*, vol. 1, pp. 1397–1403, 2003.

[5] Shyam P.K., Rajesh K., Deb K., "Multi-objective optimization of surface grinding process Using NSGA II," *First International Conference on Emerging Trends in Engineering and Technology*, vol. 3, pp. 763–767, 2008.

[6] Clarence W.S., *Vibration and shock handbook*. CRC Press, Taylor & Francis Group, 2005.

[7] Doman D. A., Warkentin A., Bauer R., "Finite element modeling approaches in grinding," *International journal of machine tools and manufacture*, vol. 49, pp. 109–116, 2009.

[8] Ioan D. M., Mike H., Eckart U., Rowe W.B., Ichiro I., *Handbook of machining with grinding wheels*. CRC Press, Taylor and Francis Group, 2007.

[9] Rogelio H., Steven L., "Plunge grinding process surface roughness model and process control." Georgia Institute of Technology, 2007.

[10] Mohammed A., Abdallah E., "Effect of grinding forces on the vibration of grinding machine spindle system," *International Journal of Machine Tools & Manufacture*, vol. 40, pp. 2003–2030, 2000.

[11] Biera J., Vinolas J. and Nieto F. J., "Time-domain dynamic modeling of external plunge grinding process," *International Journal of Machine Tools and Manufacture*, vol. 37, No. II, pp. 1555–1572, 1997.

[12] Franciszek O., Witold P., "The influence of grinding process on forced vibration damping in headstock of grinding wheel of cylindrical grinder," *International Journal of Machine Tools and Manufacture*, vol. 39, pp. 229–235, 1999.

[13] Orynski F., Pawlowski W., "The mathematical description of dynamics of the cylindrical grinder," *International Journal of Machine Tools and Manufacture*, vol. 42, pp. 773–780, 2002.

[14] Huang-Cheng C., Junz W., "A stochastic grinding force model considering random grit distribution," *International Journal of Machine Tools and Manufacture*, vol. 48, pp. 1335–1344, 2008.

[15] Sakakura M., Tsukamoto S., Fujiwara T., Inasaki I., "Visual simulation of grinding process," *IEEE*, vol. 1, pp. 233–239, 2004.

[16] Kuang-Hua F. and Shuh-Bin W., "Force modeling and forecasting in creep feed grinding using improved backpropagation (BP) neural network," *International Journal of Machine Tools and Manufacture*, vol. 37, pp. 1167–1178, 1997.

[17] lnasaki I., Karpuschewski B., Lee H., "Grinding Chatter - Origin and Suppression," *Journal of machine tools and manufacture*, vol. 4, pp. 25–32, 1999.

[18] Ichiro I., "Performance enhancement of grinding processe - Mutual interaction between the material removal processes amd the machine tool," *JKET Engineering Journal English Edition*, vol. 1004E, pp. 3–8, 2008.

[19] Hahn H., Robert S. K., *Handbook of modern grinding technology.* Chapman and Hall (New York), 1986.

[20] Garitaonandia I., Fernandes M. H., Albizuri J., Hernandez J. M., Barrenetxea D., "A new perspective on the stability study of centerless grinding process," *International Journal of Machine Tools and Manufacture*, vol. 50, pp. 165–173, 2010.

[21] Lizarralde R., Montejo M., Barrenetxea D., Marquinez J.I., Gallego I., "Intelligent Grinding: Sensorless instabilities detection," *IEEE Instrumentation & Measurement Magazine*, vol. June, pp. 30–37, 2006.

[22] Oscar G., Eduardo R., Juan C., Gilberto H, "Chattering detection in cylindrical grinding processes using the wavelet transform," *International Journal of Machine Tools and Manufacture*, vol. 46, pp. 1934–1938, 2006.

[23] Hassui A., Diniz A. E., "Correlating surface roughness and vibration on plunge cylindrical grinding of steel," *International Journal of Machine Tools and Manufacture*, vol. 43, pp. 855–862, 2003.

[24] Fernandes M. H., Garitaonandia I., Albizuri J., Barrenetxea D., "Simulation of an active vibration control system in acenterless grinding machine using a reduced updated FE model," *International Journal of Machine Tools and Manufacture*, vol. 49, pp. 239–245, 2009.

[25] Shaw B. A., Evans J.T., Wojtas A.S., Suominen L., "Grinding process control using the magnetic Barkhausen noise method," in *Electromagnetic Non-Destructive Evaluation II, Proceedings of the 3rd International Workshop on E'NDE, Reggio Calabria, Italy, September 1997*, pp. 82–87, IOS Press - Amsterdam, 1997.

[26] Jason B., Rogelio H., "Cylindrical grinding open architecture and feed rate control by power feedback." Georgia Institute of Tecnology, 2003.

[27] Eun-Sang L., Nam-Hun K., "A study on the machining characteristics in the external plunge grinding using the current signal of the spindle motor," *International Journal of Machine Tools and Manufacture*, vol. 41, pp. 937–951, 2001.

[28] Jae-Seob K., Ji-Bok S., "Trouble diagnosis of the grinding process by using acoustic emission signals," *International Journal of Machine Tools and Manufacture*, vol. 41, pp. 67–73, 2001.

[29] Albizuri J., Fernandes M. H., Garitaonandia I., Sabalza X., Uribe-Etxeberria R., Hernandez J.M., "An active system of reduction of vibrations in a center-

less grinding machine using piezoelectric actuators," *International Journal of Machine Tools and Manufacture*, vol. 47, pp. 1607–1614, 2007.

[30] Junkar M., Filipic B., "Grinding process control through monitoring and machine learning," *IEEE*, vol. 4 No. 2, pp. 77–80, 2001.

[31] Saravanan R., Asokan P., Sachidanandam M., "A multi-objective genetic algorithm (GA) approach for optimization of surface grinding operations," *International Journal of Machine Tools and Manufacture*, vol. 42, pp. 1327–1334, 2002.

[32] Ding N., Zhang D., Liu X., "Neural fuzzy prediction control of an industrial grinding process," *IEEE*, vol. 1, pp. 221–224, 2007.

[33] Robert B., "An overview of nonlinear identification and control with fuzzy systems," in *Intelligent control systems using computational intelligence technique*, 2005.

[34] Jos C. P., Neil R. E., Curt L. W., *Neural and Adaptive Systems: Fundamentals through Simulations*. Wiley, 1999.

[35] Jang J.S., Sun C.T., Mizutani E., *Neuro-Fuzzy and Soft Computing A computational approach to learning and machine intelligence*. Prentice-Hall, Inc., Upper Saddle River, New Jersey, 1997.

[36] Timothy J. Ross, *Fuzzy logic with engineering applications*. John Wiley and Sons Ltd, 2004.

[37] Claudio M., "Introduction to Fuzzy Logic." Facta Universitatis (NIS), 2000.

[38] Zadeh L. A., "Fuzzy sets," *Information and control*, vol. 8, pp. 338–353, 1965.

[39] James F. B., "Fuzzy systems- tutorial." 2004.

[40] Guanrong C., *Introduction to fuzzy sets, fuzzy logic, and fuzzzy control systems.* CRC Press, 2001.

[41] Edward T., Tanya L. and Mo J., "Introduction to Fuzzy Logic Control With Application to Mobile Robotics." NASA Center for Autonomous Control Engineering Department of Electrical and Computer Engineering University of New Mexico, 2009.

[42] Xiaolin Z., Hongwei Z., Yiming Q., Li W., "Grinding Process Fuzzy Control System Design and Application Based on MATLAB," *IEEE*, vol. 1, pp. 311–315, 2008.

[43] Hellmann M., "Fuzzy Logic Introduction." Universite de Rennes, 2005.

[44] Takagi T. and Sugeno M., "Derivation of fuzzy control rules from human operators control actions," in *In Procedings, IFAC Symposium: Fuzzy Information, Knowledge Representation and Decision Analysis*, vol. 1, 1983.

[45] Lee C. C., "Fuzzy logic in control systems: Fuzzy logic controller-Part I," *IEEE Transactions, System, Man, Cybernetics*, vol. 20, pp. 404–418, 1990.

[46] Takagi T., Sugeno M., "Fuzzy identification of systems and its applications to modeling and control," *IEEE Trans. on System, Man and Cybernetics*, vol. 4 , No. 9, pp. 116–132, 1985.

[47] Ruano A. E., " An overview of nonlinear identification and control with fuzzy systems," in *Intelligent control systems using computational intelligence techniques*, 2005.

[48] Roger J. S. R., "Fuzzy modeling using generalized neural networks and Kalman filter algorithm," in *In Proceedings of the Ninth National Coference on Artificial Intelligence*, 1991.

[49] Paul J. W., *The roots of backpropagation: from ordered derivatives to neural networks*. John Wiley and Sons Inc., 1994.

[50] Piero P. B., "Adaptive neural fuzzy inference systems (ANFIS): Analysis and applications." Lecture notes, 2000.

[51] Graham C. G., *Adaptive filtering prediction and control*. Prentice-Hall (Englewood Cliffs, N.J), 1984.

[52] Qiulin X., *Modeling and control of linear motor feed drives for grinding machines*. PhD thesis, Mechanical Engineering Department, Georgia Institute of Technology, 2008.

[53] Daniel P., "The modeling and simulation of grinding processes," in *Annals of the oradea university, fascicle of management nad technological engineering*, 1999.

[54] Alex W. Moerlein, Eric R. Marsh, Theodore R. S.Deakyne, R. Ryan Vallance, "In process force measurement for diameter control in precision cylindrical grinding," *International Journal of advanced manufacturing and technology*, vol. 42, pp. 93–101, 2008.

[55] Yi Li, S. M. Gracewski, P. D. Funkenbusch, J. Ruckman, "Chatter simulation and stability predictions for contour grinding of optical glasses," 2000.

[56] Choi T., Subrahmanya N., Li H., Shin Y., "Generalized practical models of cylindrical plunge grinding processes," *International journal of machine tools and manufacture*, vol. 48, pp. 61–72, 2007.

[57] Hongqi L., Yung C. S., "A study on chatter boundaries of cylindrical plunge grinding with process condition dependent dynamics," *International journal of machine tools and manufacture*, vol. 47, pp. 1563–1572, 2007.

APPENDIX A

A DETERMINATION OF GRINDING STIFFNESS

To determine the grinding stiffness, displacements and forces were measured simultaneously and recorded as shown in Table A.1. The grinding stiffness was determined by plotting the measured forces against displacements as shown in Figure A.1. It can be seen from this figure that, there exists a linear relationship between force and displacement. This relationship between force and displacement is the grinding stiffness, K_{eq}, and is obtained as the gradient of the curve.

Table A.1: Simultaneous forces and displacements

Displacement (mm)	Force (N)
0	0
0.0011507	0.040672
0.00143457	0.048933
0.00171844	0.057194
0.00202231	0.065456
0.00228618	0.073717
0.00257005	0.081979
0.00285392	0.09024
0.00303779	0.098501
0.00332176	0.106763
0.00360553	0.115024
0.0038894	0.123286
0.00417327	0.131547
0.00445714	0.139808
0.00474101	0.14807
0.00502488	0.157331
0.0052335	0.164859
0.0055178	0.173146

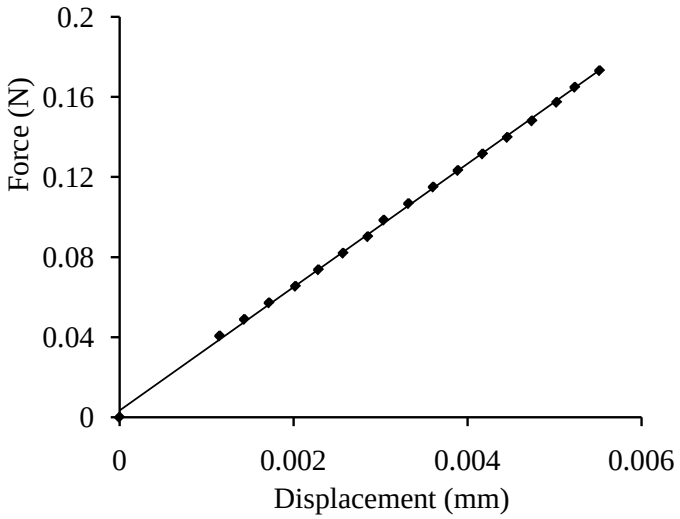

Figure A.1: Graph for determining grinding stiffness

The equation for the curve, which gives the stiffness is;

$$F = 30000\delta \tag{A.1}$$

where F is the applied force, and δ is the deflection in the direction of application of the force.

APPENDIX B

B PROGRAM FOR SIMULATION OF VIBRATIONS

```
c vibration simulation
PROGRAM VIBSIM WRITE(*,*)'ENTER THE
WORK RADIUS IN MM'
READ(*,*)RWORKMM
WRITE(*,*)'ENTER THE GRINDING WHEEL RADIUS IN MM'
READ(*,*)RWHEELMM
WRITE(*,*)'ENTER THE wheel speed in rpm'
READ(*,*)vwheeln
WRITE(*,*)'ENTER THE work speed in rpm'
READ(*,*)vworkn
WRITE(*,*)'ENTER THE INFEED'
READ(*,*)FMM
PI=3.142
F=FMM/1000
RWORK=RWORKMM/1000
RWHEEL=RWHEELMM/1000
C AE=EQUIVALENT(INSTANTANEOUS) DEPTH OF CUT,
DE=EQUIVALENT WHEEL DIAMETER, C DW=WORKPIECE
DIAMETER, DG=WHEEL DIAMETER
DW=2*RWORK
```

```
DG=2*RWHEEL
DE=(DW*DG)/(DW+DG)
AE=F
C GRINDING STIFNESS=CKG
CKG=3000
C COEFFICIENT OF GRINDING CMU
CMU=0.5
C GRIT DENSITY CR (FOR: B126 cBN=9.5/sqmm,
B151 cBN=7/sqmm, B252 cBN=3/sqmm)
C THE PAPER IS SAVED AS 'GRIT DENSITY' AND IS TITLED
C (ON CUMULATIVE DEPTH OF TOUCH-DRESSING OF
SINGLE LAYER
C BRAZED CBN WHEELS WITH REGULAR GRIT DISTRIBUTION
PATTERN)
CR=9.5
C CALCULATION OF NORMALIZED NORMAL FORCE
COEFFICIENT
C CALCULATION OF SURFACE VELOCITIES
(TST= TIME FOR STATIC MODEL)
C W=RATIO OF SURFACE WHEEL VELOCITY TO
SURFACE WORKPIECE VELOCITY
C WRITE(*,*) 'ENTER TIME TO CALCULATE
NORMALIZED FORCE COEFF. TST'
```

```
C READ(*,*) TST C WRITE(*,*)
'ENTER WHEEL SPEED AT WHICH TO
C CALCULATE Kt AND Kn IN RPM' C READ(*,*) VWHEELSN
TST=15
VWHEELSN=1500
VWHEELS=2*PI*VWHEELSN/60
VWORKSN=100
VWORKS=2*PI*VWORKSN/60
PSIS=0
VG=RWHEEL*VWHEELS
VW=RWORK*VWORKS
W=VG/VW
V=SQRT(DE/AE)
C CALCULATION OF SPECIFIC ENERGY
EC=SQRT(W*CR*V)
C CALCULATION OF THE COEFFICIENT CKS
(STATIC FORCE COEFFICIENT)
C CKS=(CMU*EC*RWORK*VWORK)/(RWHEEL*VWHEEL),
FR=CKS*AE/CMU
C CALCULATION OF RESULTANT STATIC
GRINDING FORCE=FR
FR=EC*F*W
C VWHEELSN=WHEEL SPEED ON STATIC MODEL
```

IN RPM C VWORKSN=WORKPICE

SPEED ON STATIC MODEL IN RPM C

VWHEELS=WHEEL SPEED ON STATIC

MODEL IN RADIANS C VWORKS=WORKPICE SPEED

ON STATIC MODEL IN RADIANS C LETTER S IN THE FOLLOWING

EQUATIONS DENOTES STATIC

BETAWS=VWORKS*TST

BETAGS=VWHEELS*TST

AS=VWORKS*RWORK*(BETAWS)

BS=RWHEEL*(VWHEELS)

DS=RWORK*(VWORKS)

ES=RWHEEL*(BETAGS)

GS=RWORK*(BETAWS)

HS=2*PI/VWHEELS

C CTS=CHIP THICKNESS FOR STATIC MODEL

XS=AS+(BS+DS-F)*(-COS(BETAGS))

YS=((BS+DS)*(SIN(PSIS)))*(SIN(BETAGS)+COS(BETAGS))

ZS=((ES+GS)*(COS(PSIS)))*(SIN(BETAGS))

CTS=HS*(XS+YS+ZS)

CALCULATION OF COEFFICIENTS CKN=Kn, AND CKT=Kt

CKTT=FR/(CTS*(TAN(BETAGS)*SIN(BETAGS)+COS(BETAGS)))

CKNN=FR/(CTS*CTS)

CKN=10*SQRT(CKNN*CKNN)

```
CKT=10*SQRT(CKTT*CKTT)

WRITE(*,*)CKT,CKN, FR, CTS

IF(VWHEELN.LT.1431)THEN

DO 1000 K=0,300

VWHEEL=2*PI*VWHEELN/60

VWORK=2*PI*VWORKN/60

T=T+0.01

TI=T*10

BETAG=VWHEEL*T

BETAW=VWORK*T

PSI=((RWHEEL*BETAG)+(RWORK*BETAW)-RWHEEL-RWORK)

A=VWORK*RWORK*(BETAW-PSI)

B=RWHEEL*(VWHEEL-(PSI/T))

D=RWORK*(VWORK-(PSI/T))

E=RWHEEL*(BETAG-PSI)

G=RWORK*(BETAW-PSI)

H=2*PI/VWHEEL

X=A+(B+D-F)*(-COS(BETAG+PSI))

Y=((B+D)*(SIN(PSI)))*(SIN(BETAG)+COS(BETAG))

Z=((E+G)*(COS(PSI)))*(SIN(BETAG+PSI))

CT=H*(X+Y+Z)

RFORCE=CKN*CT*COS(BETAG+PSI)-CKT*CT*SIN(BETAG+PSI)

TFORCE=CKN*CT*SIN(BETAG+PSI)+CKT*CT*COS(BETAG+PSI)
```

```
RAMPL=RFORCE/CKG*1000

TAMPL=TFORCE/CKG*1000

OPEN(1, FILE='DISPLN.DAT')

WRITE(1,*)T, RAMPL

OPEN(2, FILE='DISPLT.DAT')

WRITE(2,*)TI, TAMPL

1000 continue

ENDIF

STOP

END
```

APPENDIX C

C DETERMINATION OF GRINDING COEFFICIENT

The grinding coefficient μ was obtained graphically by plotting the measured tangential forces against the normal forces as shown in figure C.1. The forces were measured using tool dynamometer. The tool dynamometer has strain gauges arranged in such a way that, it can be used for measurement of forces in three orthogonal directions. From the plot of the tangential and normal forces, the grinding coefficient is obtained as the gradient of the curve which is 0.5.

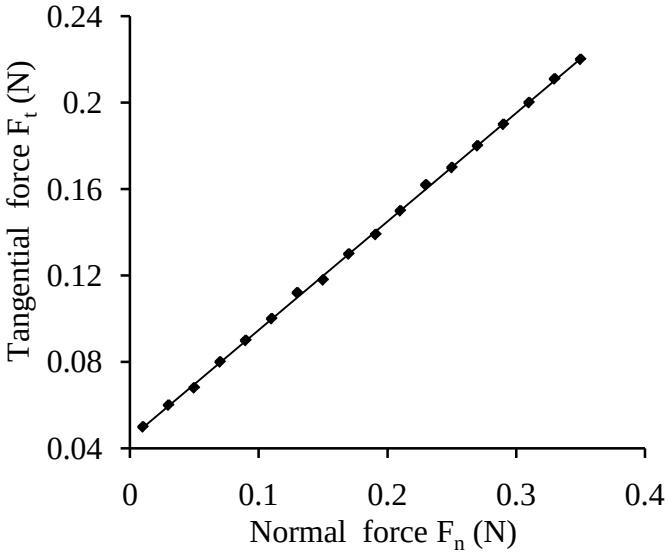

Figure C.1: Graph for the determination of grinding coefficient

APPENDIX D

D CALIBRATION OF INSTRUMENTS USED

D.1 Calibration of tool dynamometer

The tool dynamometer comprises of strain gauges arranged in such a way that they can measure forces in different directions. The tool dynamometer that is used gives analog voltages as the outputs. The voltages are proportional to the forces applied in the respective directions. Slight changes in the forces during machining can be detected and recorded in a computer via a digital to analog converter. The voltages also can be amplified to the desired level. The calibration process for the dynamometer involved applying static loads of known weights on each axis direction, that is, force in Y-direction (F_y), force in X-direction (F_x), and force in Z-direction, (F_z) as shown in Figure D.1. The loads were added one at a time and the readings in all 3 components were recorded as shown in the Table D.1.

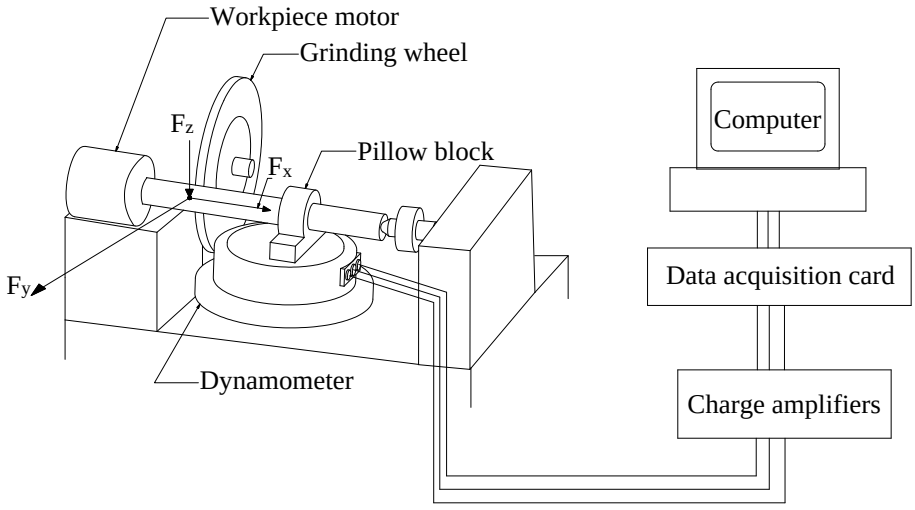

Figure D.1: Setup for tool dynamometer calibration

Table D.1: Dynamometer calibration data

Loading in X-Direction

Force (N)	X-Reading (mV)	Y-Reading(mV)	Z-Reading (mV)
0	0	0	0
5	3	0.1	0.2
35	21	0.7	2
55	33	1	3.4
75	45.2	1.4	5
95	57	1.7	6.4
115	68.7	2.1	7.9
135	80	2.5	9.5
155	91.8	2.9	11.1
175	103	3.3	12.5

Loading in Y-Direction

Force (N)	X-Reading (mV)	Y-Reading(mV)	Z-Reading (mV)
0	0	0	0
5	0.1	0.5	0.1
35	1.2	12	1.3
55	1.8	20	2
75	2.5	28.9	2.7
95	3.1	38.8	3.6
115	3.6	47.5	4.4
135	4.1	57	5.3
155	4.7	67.3	6.2
175	5.2	76.8	7.1

Loading in Z-Direction

Force (N)	X-Reading (mV)	Y-Reading(mV)	Z-Reading (mV)
0	0	0	0
30	0.3	0.5	30
50	0.5	0.7	50
70	0.7	0.9	70
90	0.9	1	90
110	1.1	1.2	110
130	1.3	1.4	130
150	1.5	1.8	150
170	1.7	2	170

It was observed that, there was cross sensitivity in all the three axes, i.e., every load applied in any direction had an effect in each of the 3-components. Calibration equations for the dynamometer were derived based on the calibration curves plotted in Figure D.2.

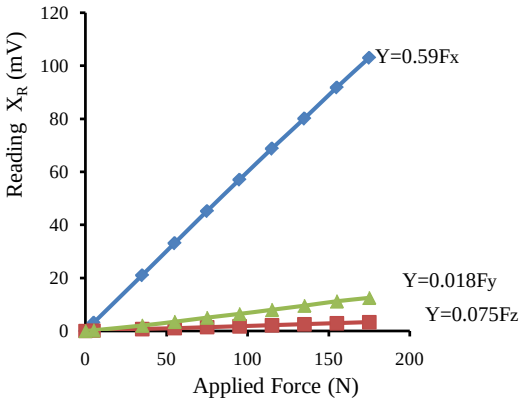

(a) plot for loading in X-direction

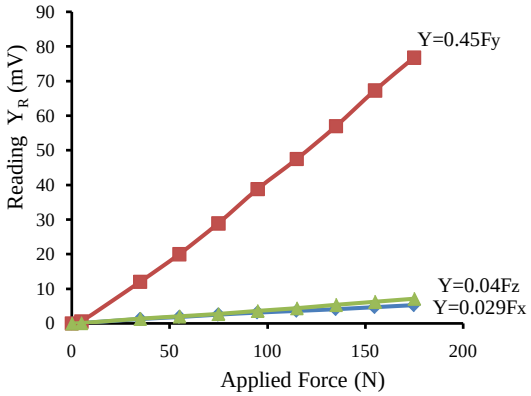

(b) plot for loading in Y-direction

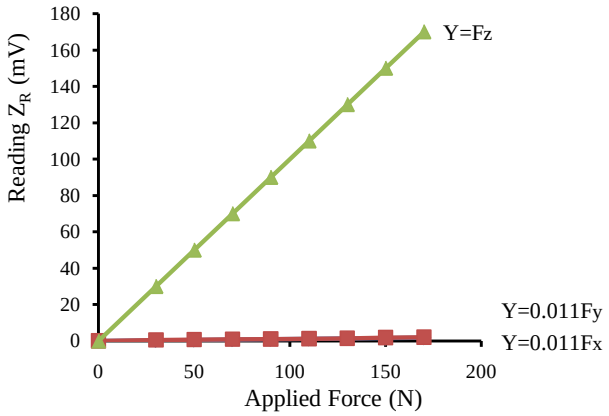

(c) plot for loading in Z-direction

Figure D.2: Dynamometer calibration curves.

Considering the gradients of the plotted lines, when the tool dynamometer was loaded

in all the three axes directions independently, the following simultaneous equations were obtained.

$$\begin{aligned} X_R &= 0.59F_x + 0.018F_y + 0.075F_z \\ Y_R &= 0.029F_x + 0.45F_y + 0.04F_z \\ Z_R &= 0.01F_x + 0.011F_y + F_z \end{aligned} \tag{D.1}$$

From equation D.1 the force components in X,Y and Z axes are obtained, taking into account the effect of sensitivity of the load applied in other component direction;

$F_x = 20.953X_R - 0.819Y_R + 1.537Z_R$, $F_y = -1.113X_R + 2.267Y_R + 0.007Z_R$,

$F_z = -0.198X_R - 0.017Y_R + 0.985Z_R$

D.2 Calibration of displacement sensor

Known displacements δ were applied to the sensor probe, and the output voltages from the sensor, V, recorded as shown in Table D.2. The output voltages were plotted against the applied displacements in the calibration curve shown in Figure D.3. From this figure it is seen that, there exists a linear relationship between the output voltage and the displacement. The equation for the curve, is

$$\delta = 0.45556V \tag{D.2}$$

Table D.2: Displacement sensor calibration data

Displacement (mm)	Output voltage (V)
0	0
0.3	1.4
0.5	2.22
0.6	2.6
0.75	3.3
0.8	3.49
0.95	4.27
1	4.5

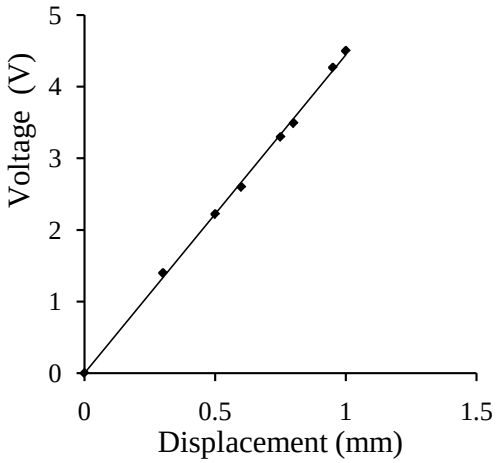

Figure D.3: Plot for displacement sensor calibration

APPENDIX E

E CODE FOR FFT AND RMS OF DISPLACEMENTS

E.1 Code for finding Fast Fourier Transforms of displacements

```
load DISPLN.dat

amp=DISPLN(:,4);

y=fft(amp,256);

Pyy=y.*conj(y)/256;

f=2000/256*(0:127);

plot(f,Pyy(1:128))

title('Power spectral density')

xlabel('Frequency (Hz)')
```

E.2 Code for finding RMS values of the displacements

```
load DISPLN.dat

a=DISPLN(:,2);

y=sqrt(sum(a.*conj(a))/size(a,1))
```